Origin of the Earth and Moon

Thesis by

Miki Nakajima

In Partial Fulfillment of the Requirements

for the Degree of

Doctor of Philosophy

California Institute of Technology

Pasadena, California

2016

(Defended Oct 30th, 2015)

I dedicate this thesis to our mysterious Moon :)

Acknowledgements

I am deeply grateful to my advisor Dave Stevenson for wonderful guidance, wisdom and humor. I have been very inspired by his attitude towards science. Dave is knowledgeable in any research field and his ideas are exceptionally creative and inspiring. He is willing to challenge conventional ideas including own previous research, and he really cares about young scientists and future directions of planetary science. I think that he is one the greatest *samurai* in academia who is loyal to science (this is the biggest compliment I can think of). I am so fortunate that I have had this opportunity to work with him through my Ph.D. career.

I would like to thank Andy Ingersoll for providing this great opportunity to work with him. He is a living legend in planetary science and it has been very fun to work with him by sharing excitement about research findings, observations and ideas. I cannot wait for having discussions with you about upcoming observations by Cassini. I also would like to thank Andy for inviting us for his house on thanksgiving and July 4th. It was wonderful to spend time with you, your family, and our colleagues on these special occasions.

I am thankful to Paul Asimow for providing perspectives of thermodynamics and science discussions. I have learned so much through his classes and discussions we had.

I would like thank John Eiler for teaching me geochemistry and having fun science discussions with me at PRG (petrology reading group) and other places. When I came to Caltech, I had no background in geochemistry, but now it has become an essential part of my research.

I am grateful to Konstantin Batygin, Bethany Ehlmann, Yuk Yung, and Oded Aharonson for providing me with scientific and career advice. I would like to thank former graduate students we had science discussions with over SecDec lunch: Aaron Wolf, Dan Bower, June Wicks, and Clair Waller-Thomas. I am so fortunate to meet with the former graduates Kaveh Pahlevan, Kevin Lewis, Alejandro Soto, Kuai Le, and Mike Line, who have provided me science and career advice. I cannot imagine my PhD life without having my wonderful officemates Zhang Su, Cheng Li, Mike Wong, and Danielle Piskorz. It has been great fun to take classes and have fun together with my classmates, including Peter Gao, Masha Kleschcheva, Hilary Martens, Adam Waszczak, and Josh Kammer. I cannot believe it has been five years since we first met. I wish you all the best luck with the wonderful journeys ahead of you. It has been fun to spend time in the offices as well as outside with my fellow graduates students and postdoctoral scholars Hao Cao, Bjoern Benneke, Kat Deck, Leslie Rogers, Abigail Fraeman, Pushkar Kopparla, Henry Ngo, Joe O'Rourke, Lu Pan, Dana Anderson, Peter Buhler, Patrick Fischer, Chris Spalding, Ian Wong, Elizabeth Bailey, and Nancy Thomas. I am very thankful to our administrative staff for helping me in many ways, including Irma Black, Margaret Carlos, Bronagh Glaser and Ulrika Terrones.

I am very thankful to Tobias Bischoff, Belinda Pang, Rebecca Schwantes, John

Chris Rollins, and Bryan Riel for working at home and having fun with me. You are my extended family in Pasadena.

Last but certainly not least, I would like to thank my family, Tsuneo Nakajima, Kazuyo Nakajima, Emi Matsubara, and Nobuko Nakajima. Without any of you, I would not have been here (literally). I am so thankful that you supported me in pursuing my passion even though my career is quite unusual as a Japanese woman. It has been a wonderful journey with you all and I am excited for our upcoming years. I would like to thank my American family Steven Yoda, who is related to me through my great great grand parents, for welcoming me as a part of your family.

Abstract

According to the giant impact hypothesis, the Moon formed from a disk created by an impact between the proto-Earth and an impactor. Three major models for this hypothesis are (a) standard model: a Mars-sized impactor hit the Earth; (b) fast-spinning Earth model: a small impactor hit a rapidly spinning Earth; and (c) sub-Earths model: two half-Earth sized planets collided. These models have been supported because they can explain several observed features of the Earth-Moon system, such as the Moon's mass, angular momentum, and potentially geochemical measurements that suggest that the Earth and Moon have nearly identical isotopic ratios.

However, it is uncertain if these models are consistent with other geochemical constraints. For example, isotopic measurements of Earth's rocks indicate that the early Earth's mantle was chemically heterogeneous and this signature was preserved for billions of years. However, it is not clear if the giant impact hypothesis is consistent with this geochemical constraint because the giant impact could have been so energetic that the Earth's mantle could have completely mixed and homogenized. Furthermore, the fraction of the Earth's mantle that became molten by the impact is not well known, even though it is known to have significantly affected the subsequent evolutions of

the Earth's interior and atmosphere. Additionally, the water and volatile content of the Moon may have an important implication for the lunar origin. Since the Moon-forming disk formed through a giant impact process, it must have been hot and partially vaporized. From this disk, a significant amount of water and volatiles may have escaped to space. However, this idea may contradict recent geochemical studies that indicate that Moon may not be as dry as previously thought.

Furthermore, moons of other planets may provide comprehensive pictures of the origin and evolution of the moons. For example, the Pluto-Charon system could have formed via a giant impact. Recent studies also suggest that Mars' satellites Phobos and Deimos could have formed in the same way. In contrast, satellites around the gas giants could have formed in situ from their proto-satellite disks and by gravitational capture. One of the Saturnian satellites, Enceladus has very unique geological and dynamical features. Cassini spacecraft observed that water plumes are emanating from cracks on the surface (so-called "tiger stripes"). These plumes may originate from a few kilometer deep subsurface liquid ocean. Along the cracks, strong thermal emissions have been observed and these are thought to be related to the plume activities, but the connection has been still unclear.

In my Ph.D. thesis, I aim to understand the origin and evolution of the Earth, Moon, and the Saturnian moon Enceladus. In order to understand the initial state of the Earth's mantle and the Moon-forming disk, I perform giant impact simulations with a method called smoothed particle hydrodynamics (SPH). I show that the Earth's mantle becomes mostly molten by the impact and that the mantle re-

mains unmixed in (a), but it may be at least partly mixed in (b) and (c). Therefore, (a) is most consistent with the preservation of the mantle heterogeneity. As for the Moon-forming disk, my calculations show that the disk of the standard model has a relatively low temperature (up to 4500 K) and low vapor mass fraction ($\sim 20-30\%$) while the disk formed by other models could be much hotter (6000-7000 K) and has a higher vapor mass fraction ($80-90\%$). Furthermore, I investigate the structure of the Moon-forming disk and estimated the extent of water escape. I show that escape is in the diffusion-limited regime and water escape from the disk to space is minor. This result could explain recent measurements on lunar water abundance. Furthermore, I develop a dynamical model that includes flow dynamics and flow-ice wall interaction that explains the Enceladus plume mass flux, heat flux, and several observed signatures. These studies will deepen comprehensive understanding of the origin of the moons in the solar system.

Contents

List of Figures

List of Tables

Chapter 1

Introduction

According to the standard giant impact hypothesis, the Moon formed from a debris disk created by a collision between an impactor and the proto-Earth (Hartmann and Davis, 1975; Cameron and Ward, 1976). This hypothesis is favorable because it can successfully explain the Moon's mass, its iron depletion, and its angular momentum. However, the standard model might fail to explain the nearly identical isotope ratios of the Earth and Moon (e.g. oxygen, silicon, tungsten, and titanium, Wiechert et al. 2001; Armytage et al. 2012; Touboul et al. 2007; Zhang et al. 2012). This is because numerical simulations have shown that most of the disk materials originate from the impactor, which is likely to have had different isotope ratios from the proto-Earth (e.g., Benz et al., 1986). Therefore, the Moon should have primarily inherited the isotope ratios of the impactor. To overcome this inconsistency, Pahlevan and Stevenson (2007) have suggested that turbulent mixing may have homogenized the isotope ratios between the disk and Earth through the Earth's atmosphere that connected the two reservoirs. However, this model may have difficulties explaining the silicon isotope ratios (Pahlevan et al., 2011; Halliday, 2012). It may be possible that the impactor happened to have similar isotopic ratios of a specific element to those of Earth, such as oxygen (Kaib and Cowan, 2015; Mastrobuono-Battisti et al., 2015), but it is still not very likely that it has all the observed isotopic ratios identical to those of Earth. Recently, new dynamical models have been suggested for the origin of the Moon. Ćuk and Stewart propose that an impactor hit a fast-spinning Earth (Ćuk and Stewart, 2012), whereas Canup suggests a giant impact between two half Earth-mass objects (Canup, 2012) ("sub-Earths", hereafter). In these cases, the

composition of the disk is nearly the same as that of the Earth's mantle, so that the isotope similarities can be explained.

However, it has not been studied whether these giant impact models are consistent with other geochemical constraints. A 2.8 billion year old rock (Kostomuksha komatiites) that may originate from the deep mantle shows an excess of ^{182}W with respect to modern terrestrial samples (Touboul et al., 2012). Since ^{182}Hf decays to ^{182}W with 8.9 Myr half-life, the anomaly must have been formed in the first $\sim$ 60 Myr after the formation of the solar system and it must have been preserved at least until 2.8 billion years ago. This event is likely to predate the Moon formation ($>$ 60 Myr, Touboul et al. 2007) which indicates that this pre-existing mantle heterogeneity may have survived the energetic giant impact. However, no quantitative research has been conducted on this issue.

In addition to this, the giant hypothesis has not successfully explained the volatile depletion of the Moon. Since the Moon-forming impact was so energetic, the Moon-forming disk must have been at least partially vaporized. Under this circumstance, the volatiles are thought to be lost from the disk by hydrodynamic flow (hydrodynamic escape) (Cameron and Ward, 1976). Some of previous work suggests that this mechanism may have removed most of hydrogen, which is dissociated from water, due to its light mass (Desch and Taylor, 2013). Some heavier elements may have escaped from the disk as well through collisions with lighter atoms. However, isotope measurements of hydrogen in lunar volcanic glasses and melt inclusions suggest that the D/H ratio of the Moon could be almost the same as that of the Earth (Saal et al.,

2013). This is puzzling because significant hydrogen escape is likely to enhance the D/H ratio of the residue. A number of studies have been conducted to measure the water content of lunar crystals and they suggest that the disk did not lose its water and hence the Moon was more "wet" than previously thought (e.g., Boyce et al., 2010; Saal et al., 2013; Hauri et al., 2011) even though determining the water abundance of the bulk Moon is a challenging problem and is an active area of research (e.g., Boyce et al., 2014).

Furthermore, moons of other planets may help deepening comprehensive understanding of the origin and evolution of the moons. For example, the Pluto-Charon system as well as Mars' satellites (Phobos and Deimos) could have formed via giant impacts (Canup, 2005; Canup and Salmon, 2014). On the other hand, satellites around gas giants could have formed in situ from the proto-satellite disks and by gravitational capture. These gas giants tend to have multiple moons and they gravitationally interact with each other. One of the Saturnian satellites Enceladus, whose eccentricity is excited by another satellite Dione, has very unique geological and dynamical features. Cassini spacecraft observed that water plumes are emanating from cracks on the surface (so-called "tiger stripes") (Porco et al., 2006). These plumes may originate from a subsurface liquid ocean (Iess et al., 2014). Along the cracks, strong thermal emissions have been observed and these are thought to be related to the plume activities, but the connection has been still unclear.

In my thesis, I aim to understand the origin and evolution of the Earth, Moon, and the Saturnian moon Enceladus. In Chapter 2, in order to understand the initial

state of the Earth's mantle after the Moon-forming impact, I performed giant impact simulations with a method called smoothed particle hydrodynamics (SPH). I show that the Earth's mantle becomes mostly molten by the impact and that the mantle remains unmixed in the standard model, but it may be at least partly mixed in the fast-spinning Earth and sub-Earths models. Therefore, the standard model is most consistent with the preservation of the mantle heterogeneity.

In Chapter 3, by performing SPH and analytical calculations, I determine the initial structure of the Moon-forming disk. My calculations show that the Moon-forming disk of the standard model has a relatively low temperature (up to 4500 K) and low vapor mass fraction ($\sim 20-30\%$) while the disk formed by other models could be much hotter (6000-7000 K) and has a higher vapor mass fraction ($80-90\%$). These differences could affect the evolution of the Moon-forming disk and predict different resulting geochemistry of the Moon.

In Chapter 4, based on the thermal structure of the Moon-forming disk I develop in Chapter 3, I investigate the extent of water and volatile loss from the Moon-forming disk. I find that the Moon-forming disk is always dominated by heavy elements and the mixing ratio of hydrogen is low at the upper part of the disk. This leads to the conclusion that hydrodynamic escape from the Moon-forming disk was in the so-called diffusion-limited regime. This indicates that hydrogen had to diffuse out from the heavy element-rich disk in order to escape from the system. This is an inefficient process, and therefore water and volatile loss from the disk was minor.

In Chapter 5, I develop a dynamical model to explain the observed heat flow

and mass flow from Enceladus assuming that the flow originate from a subsurface liquid ocean and water vapor condenses onto the surrounding ice walls as the flow approaches the surface. My study finds that water condensation onto the ice walls is most intense near the surface. This generates strong thermal emission from the ice surface that is consistent with the Cassini observations. I also find that the crack width may need to be narrow (< 0.1 m) to explain the observed mass and heat flows from the Enceladus surface.

Chapter 2

Initial state of the Earth's mantle after the Moon-forming impact

2.1 Introduction

The so-called giant impact hypothesis is a widely accepted explanation for the origin of the Moon (Hartmann and Davis, 1975; Cameron and Ward, 1976). According to the standard version of this hypothesis, a Mars-sized impactor hit the proto-Earth and created a disk around the planet from which the Moon accreted. This hypothesis has been favored because it can explain the Moon's mass, iron depletion, and the angular momentum of the Earth-Moon system. However, this model has difficulty in explaining the fact that the Earth and Moon have nearly identical isotopic ratios (e.g. oxygen, silicon, and tungsten, Wiechert et al. 2001; Herwartz et al. 2014; Armytage et al. 2012; Touboul et al. 2007). The typical outcome of a giant impact simulation is that the disk materials are derived mainly from the impactor (e.g., Benz et al., 1986), which is often assumed to have had different isotopic ratios given that the oxygen isotopic ratios between the Earth and Mars differ by 0.321‰ (Franchi et al., 1999). Reufer et al. (2012) report that an impact at a high impact velocity and steep impact angle would deliver more Earth's mantle materials to the disk, but it is still difficult to explain the identical isotopic ratios.

Pahlevan and Stevenson (2007) have suggested that turbulent mixing in the Earth's atmosphere and the disk homogenized the isotopic ratios of the two reservoirs. This model could potentially solve the isotopic problem, but it has several shortcomings. This mechanism may not work for all of the observed isotope systems, such as Si (Pahlevan et al., 2011; Armytage et al., 2012). Furthermore, this mixing would have required the Earth's whole mantle convection during the Moon formation, but such

convection may not have occurred due to the thermally stratified structure of the mantle after the impact (discussed in Sections 2.2.4 and 2.3.3). Even if the post-impact mixing caused the disk to have the same isotopic reservoir as, say, the outer 80% of the mantle but failed to equilibrate with the inner 20%, then the Earth and Moon could still be isotopically different if there had been a subsequent mixing of the Earth's mantle after the Moon formation. At present, there is no detectable oxygen isotopic difference (with respect to the three isotopes, which are referred to as $\Delta^{17}\mathrm{O} \equiv \delta^{17}\mathrm{O} - 0.52\delta^{18}\mathrm{O}$) among Earth rocks.

The possibility that the impactor had a similar oxygen isotopic ratio to the Earth has been recently revisited. Kaib and Cowan (2015) investigate feeding zones of terrestrial planets based on orbital calculations and predict that this possibility is $\sim 5\%$ or less. Mastrobuono-Battisti et al. (2015) have performed similar analyses and report that the possibility could be as high as $20-40\%$ if its standard deviation ($\pm\sigma$) is included, although the most plausible value of this possibility ($\sim 10-20\%$) may not be significantly different from the value estimated by Kaib and Cowan (2015). It is also possible that the impactor could have been compositionally similar to enstatite chondrites (e.g., Herwartz et al., 2014), whose compositions are much more similar to those of the Earth than those of Mars. Alternatively, a recent model of planet formation, the so-called Grand Tack model (Walsh et al., 2011), may suggest a different outcome. This Grand Tack model suggests that the planetesimal disk was truncated at 1 AU due to migration of gas giants and, as a result, terrestrial planets mainly formed from the inner part of the disk. This model may increase the chance of hav-

ing an impactor with a composition similar to the Earth (personal communications with Alessandro Morbidelli). This increased probability may arise possibly because the main source of the Earth's materials was confined to a limited region of distances from the Sun, or perhaps because of more efficient mixing of the source materials than the standard models predict (discussed in Section 2.4.4). In either case, this finding would imply that the Earth is different from Mars but not necessarily different from the terminal giant impacting body that led to the formation of the Moon (often called as "Theia"). It should be noted that having the same oxygen isotopic ratios for the proto-Earth and impactor does not necessarily explain the nearly identical tungsten and silicon isotopic ratios of the two (Dauphas et al., 2014; Fitoussi and Bourdon, 2012).

New giant impact models have been suggested as alternatives. Ćuk and Stewart (2012) propose that an impactor hit a rapidly rotating proto-Earth (called the "fast-spinning Earth"), whereas Canup (2012) suggests a giant impact between two half-Earth-mass objects (here we call this "sub-Earths", and the model is also called "large impactor" and "half Earth" in other literatures). In these cases, the composition of the disk would have been similar to that of the Earth's mantle; therefore, the models could explain the isotopic similarities. In these models, the angular momentum of the Earth-Moon system after the impact was 2-3 times as large as today's value. Ćuk and Stewart (2012) suggest that the evection resonance between the Moon and the Sun could have transferred the excess angular momentum of the Earth-Moon system to the Sun-Earth system. This resonance occurs when the period of precession of the

pericenter of the Moon is equal to the Earth's orbital period (Touma and Wisdom, 1998). It is also possible that there is some other resonance that yields the same result (Wisdom and Tian, 2015). Nonetheless, it is not yet clear whether any resonance could efficiently remove the excess of the angular momentum (personal communications with Jack Wisdom). The existence of a resonance does not imply the removal of a large amount of angular momentum because that would depend on a particular and possibly narrow choice of tidal parameters.

These new models are indistinguishable in terms of the oxygen isotopic ratios, but additional geochemical constraints may differentiate these models. For example, it has been suggested that the Earth's mantle may not have been completely mixed by the giant impact. This has been drawn from various isotopic studies, especially those on the Hf-W system. Hf is a lithophile ("rock-loving") element, whereas W is a moderately siderophile ("iron-loving") element. ^{182}Hf decays to ^{182}W with a 9 Myr half-life; thus, the mantle of a planet would have an enhanced ^{182}W/^{184}W if differentiation occurred while Hf was still alive (within the first $\sim$ 60 Myr after CAI formation). Most terrestrial rocks have similar values of ^{182}W/^{184}W (Lee and Halliday, 1996), but Willbold et al. (2011) and Touboul et al. (2012) find that 2.8 and 3.8 billion years old rocks have ratios in excess of these values. This finding may indicate that the early mantle was heterogeneous (while ^{182}Hf was still present) and that the signature was preserved at least until 2.8 billion years ago. Determining the cause of the heterogeneity is an active area of research. It should be noted that the chemical heterogeneity could take many forms, including a non-uniformity of noble

gas mole fraction (e.g., Mukhopadhyay, 2012) or a discrete layer of denser mantle material at the base of the mantle because of the formation of a basal magma ocean (e.g., Labrosse et al., 2007).

Regardless of the cause or form, if the mantle heterogeneity formation predated the Moon-forming impact, the Earth's mantle may not have been mixed even by the giant impact. Previous studies based on the lunar $^{182}W/^{184}W$ ratio suggest that the Moon formed as early as 30 Myr after CAI formation (e.g., Lee et al., 1997), whereas Touboul et al. (2007) propose that ∼60% crystallization of the lunar magma ocean occurred after ∼60 Myr by taking into account the excess of ^{182}W formed by neutron capture of ^{181}Ta. This is consistent with the age estimate based on other systems (e.g., Sm-Nd, Carlson and Lugmair 1988, and recent studies on orbital dynamics, Jacobson et al. 2014). Although the age of the Moon is still under debate, recent work tends to suggest a young age of the Moon (> 60 Myr). Herein, we focus on the scenario in which the mantle heterogeneity predated the formation of the Moon.

In addition to the mantle mixing, understanding the extent of the impact-induced mantle melting is important because the extent affected the evolution of the Earth's interior and atmosphere (e.g., Abe and Matsui, 1986; Tonks and Melosh, 1993; Elkins-Tanton, 2008). When the Earth grew through collisions with numerous impactors, these impactors melted part of the Earth's mantle and delivered their metallic iron to the Earth. The metallic iron of small impactors (at least up to a few hundred kilometers in size) would have been dispersed as droplets and the resulting rainfall would have led to metal-silicate equilibration during the descent to the metal pond at

the base of the magma ocean (Stevenson, 1990). The iron might have passed through the solid-rich deeper mantle without further equilibration with the ambient mantle. If the abundance of siderophile elements in the mantle recorded the metal-silicate equilibrium at the base of the magma ocean, the magma ocean depth would have been approximately around 28-40 GPa (700-1,200km deep) (e.g., Li and Agee, 1996; Righter et al., 1997). However, this model may be too simplistic because it assumes that the core formation occurred by a single stage process, but the Earth's core must have formed though multiple impacts processes (Wade and Wood, 2005; Rubie et al., 2015). Thus, the mantle geochemistry is not likely to have recorded the single impact event. The concentrations of siderophile elements in the mantle reflect very complex processes of the core formation (e.g., Stevenson, 1989; Zimmerman et al., 1999; Rubie et al., 2003; Dahl and Stevenson, 2010; Shi et al., 2013).

Analytical and numerical studies suggest that a significant fraction of the mantle would have experienced melting by the Moon-forming impact (e.g., Tonks and Melosh, 1993; Canup, 2008a; de Vries et al., 2014). A simple estimate can be described as follows; for an impacting body with velocity 10 km/s, the specific kinetic energy carried by the body is 5×10^7 J/kg. The latent heat of melting is about 1×10^6 J/kg (for a mean temperature of 2500K). Therefore, a Mars-mass projectile would deliver several times more energy than that needed to melt the entire mantle, assuming that the pre-impact state is near the solidus. Of course, this does not indicate that the entire mantle is in fact melted upon impact because the heating is heterogeneous and because part of the impact-induced energy is partitioned to the kinetic energy of the

system. This makes the important point that the extent of melting must be assessed by considering the budgeting of all delivered energy and not merely by considering the shock heating associated with the primary impact (discussed in 2.4.1). In this respect, giant impacts differ from small impacts.

It is often assumed that if there is complete melting at one time, then the preservation of geochemical reservoirs or the retention of volatiles (e.g., He) is not possible. To the extent that this assumption is correct, the geochemical evidence appears to contradict models in which there is complete melting. However, we will argue that preserving heterogeneity (i.e., lack of complete mixing) is possible even if most or all of the mantle becomes molten by an impact (Section 2.2.4).

We also consider another problem: even if the mantle heterogeneity survived the Moon-forming impact, it could have been erased in the subsequent evolution. This could have occurred in two different ways: in the period immediately after the giant impact during the period of "healing" (cool-down following a giant impact, leading to a thermal state rather similar to that before the giant impact); or during the very long evolution of the magma ocean and solidifying mantle (time scale of millions to even hundreds of millions of years). This paper is concerned only with the first of these.

We aim to make connections between dynamics and geochemical observations in terms of the Earth's early mantle. Herein, our main questions are as follows: (1) What is the extent of mantle melting after the Moon-forming impact? (2) If the pre-impact Earth's mantle was heterogeneous, did the giant impact erase the signature?

(3) Was the post-giant impact cooling (during the subsequent thousands of years) capable of erasing the pre-giant impact heterogeneity? We attempt to answer these questions using the three different models: (a) standard, (b) fast-spinning Earth, and (c) sub-Earths. Smoothed particle hydrodynamics (SPH) is used for the giant impact simulations (Section 3.2.1). Two different equations of state are used (Section 2.2.2). Furthermore, we investigate the possibility that the Moon-forming impactor and Earth were isotopically similar (Section 2.4.4).

2.2 Model

2.2.1 Smoothed particle hydrodynamics (SPH)

SPH is a Lagrangian method in which a fluid is represented by numerous particles (grids). A particle i has a characteristic size h_i, which is the so-called smoothing length. The mass of the particle m_i is distributed within a sphere of radius $2h_i$. Each particle has its own density distribution according to its weighting function (kernel). The density at a given location is calculated as the sum of the density distributions of nearby particles. In a standard SPH, each particle has the same mass, therefore a massive object (e.g. a planet) can be resolved better than a less massive object (e. g., a Moon-forming disk). The details of SPH are included in previous studies (e.g., Nakajima and Stevenson, 2014).

2.2.2 Equation of state

We use two different equations of state (EOS) for the mantle materials. One of the equations represents forsterite Mg_2SiO_4 (hereafter "forsterite EOS"). Forsterite is the magnesium end member of the olivine solid solution series and is the major mineral phase in the upper mantle (P<$\sim$14GPa). The forsterite EOS is derived from the semi-analytic equation of state known as M-ANEOS (Thompson and Lauson, 1972; Melosh, 2007). M-ANEOS has been commonly used for hydrodynamic simulations and it can treat phase changes and co-existing multiple phases. However, it does not correctly describe the high-pressure properties, especially when the starting material is already in a high-pressure phase such as perovskite $MgSiO_3$ (now more correctly designated bridgmanite). For this reason, we also use an equation of state that represents $MgSiO_3$ liquid ("$MgSiO_3$ liquid EOS"). Since the Moon-forming impact would induce global melting of the mantle as discussed in Section 2.3.3, the liquid EOS is more suitable for this calculation. For comparison, we perform a calculation using an $MgSiO_3$ bridgmanite EOS and discuss the results in Sections 2.3.2 and 2.6.3 (Supplementary materials). Since there is no ready-to-use $MgSiO_3$ liquid EOS for hydrodynamic simulations, we reconstruct an equation of state based on an analytic expression of the Helmholtz free energy and thermal coefficients derived from the first-principles calculations (e.g., de Koker and Stixrude, 2009). The details are described in Section 2.6.1.

2.2.3 Melting criterion

We consider that a region is molten if its entropy gain, which is the entropy difference before and after the impact, exceeds the entropy required for melting $\Delta S_{\rm melt}$. A wide range of $\Delta S_{\rm melt}$ has been reported, but here we take a high end-member $\Delta S_{\rm melt} \sim 623$ J/K/kg in the subsequent calculations ($MgSiO_3$, Stixrude and Karki 2005). We also assume that the mantle is close to the solidus before the impact, as discussed in detail in Section 3.2.3. It should be noted that since the entropy of melting is a direct measure of the disorder accompanying melting, it should be relatively insensitive to pressure or temperature, unlike the latent heat of melting.

2.2.4 Mixing criterion

As discussed in Section 2.3.2 in greater detail, one of the most important consequences of a giant impact is that the outermost part of the planet would undergo a greater rise in irreversible entropy than the deeper regions because it would undergo higher shock-heating on average. This leads to $dS/dr > 0$, where S is the entropy and r is the mean radial distance from the center of the Earth to an equipotential surface (the equipotential surfaces within the planet are oblate due to the fast rotation of the planet). Therefore, the mantle is stable with respect to thermal convection immediately after the giant impact. Under this circumstance, even if the mantle is molten, the mantle would not spontaneously convect or homogenize. After a giant impact, there is a variation in the entropy rise within the same r, but we ignore the azimuthal dependence (discussed in Section 2.4.2). Our calculations are carried out

using entropy values that are averaged over latitude and longitude. We discuss the possible shortcomings of this approach in Sections 2.4.2 and 2.6.7.

The key issue here is that this entropy profile ($dS/dr > 0$) does not necessarily mean that the mantle remains unmixed. The giant impact transfers a large amount of kinetic energy to the mantle, which may dynamically mix this stably stratified mantle. Our SPH calculations dampen the velocity shears on a short timescale (but without allowing turbulence), indicating an unrealistically large viscosity, and therefore they are not suitable for analyzing the mixing directly. We must instead use the velocity fields and energy state at an early stage after the giant impact to compute the extent of mixing.

We investigate the mixing state of the mantle based on an energy balance. We assume that the mantle is unstable and mixed if the impact-induced kinetic energy of the mantle ΔKE exceeds the potential energy of the stably stratified mantle ΔPE by approximately a factor of two, i.e., $\Delta\mathrm{PE}/\Delta\mathrm{KE} < 0.5$ (see Section 2.6.2). The most important source of ΔKE is differential rotation arising from the oblique impact, which is a necessary attribute of any giant impact that is capable of forming the Moon. ΔKE is calculated as the kinetic energy differences in the mantles between before and after the impact, which is directly obtained from the SPH calculation (here, "after" indicates a state where the Earth rotates as a rigid body). The key point here is that ΔKE is not the same as the kinetic energy of the post-impact Earth if the Earth has an initial spin (this is the case for b). This is because the velocity shear is induced by the impact, not by the initial rotation of the planet and it is this

differential rotation that is responsible for the instability. The angular momentum is of course conserved in this process of energy redistribution. In an overturn that leads to mixing, half of the ΔKE contributes to overcoming gravity, and half is dissipated as heat. Therefore, in this case, the ΔKE is sufficient, by more than a factor of two, to overcome the potential energy of the stably stratified mantle.

ΔPE is the potential energy difference between the stability stratified mantle ($dS/dr > 0$) and mixed mantle ($S(r) = S_{\rm ave}$ =const., where $S_{\rm ave}$ is the averaged entropy of the pre-mixing mantle). ΔPE can be expressed approximately as

$$\Delta PE = \int_{R_{\rm CMB}}^{R_{\rm s}} 4\pi r^2 V(r) \Delta\rho dr, \tag{2.1}$$

where

$$\Delta\rho = \left(\frac{\partial\rho}{\partial S}\right)_p (S(r) - S_{\rm ave}). \tag{2.2}$$

$R_{\rm CMB}$ is the distance from the center to the core-mantle boundary (CMB) and $R_{\rm s}$ is the planetary radius. $V(r)$ is the potential energy per unit mass at r. The gravitational potential of a sphere with the core density ρ_1 and mantle density ρ_2 is

$$V(r) = -\frac{4\pi G}{3}\frac{\rho_1 R_1^3 + \rho_2(r^3 - R_1^3)}{r} - 2\pi G\rho_2(R_2^2 - r^2), \tag{2.3}$$

where R_1 and R_2 are the core and planetary radii ($R_1 < r < R_2$), respectively, and G is the gravitational constant. The value of $(\partial\rho/\partial S)_p \equiv -\alpha T\rho/C_p$ depends on the choices of EOS, V and T but it is typically $-0.3 \sim -0.5$ kg^{2}K/m^{3}J over the parameter range of interest. α is the thermal expansion coefficient, and C_p is the specific heat

at constant pressure.

2.2.5 Initial conditions

Both the target and impactor consist of 70% mantle (forsterite or $MgSiO_3$ liquid) and 30% core (iron) by mass. We assume that the mantle is compositionally uniform prior to the impact (as discussed in Section 2.4.2, it is possible that the mantle was compositionally stratified prior to the giant impact, as would be the case if there were melt migration and a possible basal magma ocean prior to the impact, Labrosse et al. 2007). Initially, the mantle has a uniform entropy such that the temperature at the model surface is approximately 2000K (3165 J/K/kg for forsterite and 3350 J/K/kg for $MgSiO_3$ liquid). It should be noted that this parameter is not important in the model or in the interpretation of the results. Of course, the true physical temperature of Earth at its surface could be as low as $\sim$ 300K if any earlier steam atmosphere has collapsed. However, the high heat flow in this epoch would lead to temperatures close to the solidus even at a depth of 10km (far too small a distance to be resolved in SPH and a negligible contribution to the total heat capacity). The essential idea here is that the pre-impact Earth cannot cool efficiently at depth to below the solidus temperature (and perhaps not even to the solidus temperature on average) because solid-state convection is unable to eliminate the heat of previous large impacts by convection in the time that has elapsed since the previous giant impact. The most important parameter in assessing the melting upon impact is irreversible entropy production and not temperature. Here, three types of giant models are investigated: (a) standard, (b)

fast-spinning Earth, and (c) sub-Earths. The parameters considered are the impactor-to-total mass ratio $M_{\rm i}/M_{\rm T}$, the total mass of the target and impactor, $M_{\rm T}$, the scaled impact parameter b ($b = \sin\theta$, here θ is the impact angle), the impact velocity $v_{\rm imp}$, and the initial spin period, $\tau_{\rm spin}$. The initial conditions of the models are listed on Table 3.1.

2.3 Results

2.3.1 Comparison of equations of state

The behaviors of the two EOS are shown in Figure 2.1. One of the differences is that the entropy of the forsterite EOS is concave-up, whereas that of the $MgSiO_3$ liquid EOS is concave down (Figure 2.1A). This disparity can be explained by the signs of $(\partial^2 S/\partial^2 \rho)_T$. For the $MgSiO_3$ liquid EOS, this expression becomes $(q+1)C_V\gamma/\rho^2$, where $\gamma = \gamma_0(V/V_0)^q$ is the Grüneisen parameter (discussed in Section S1.1) and C_V is the specific heat at a constant volume. The exponent q is positive for solids and negative for liquids (Stixrude et al., 2009). Therefore, the exponent q of the $MgSiO_3$ liquid EOS is chosen to be -1.6. On the other hand, the forsterite EOS (M-ANEOS) does not differentiate liquids from solids and assumes a positive q ($\gamma = \gamma_0(V/V_0) + 2/3(1-V/V_0)^2$, Equation 4.11, Thompson and Lauson 1972). Therefore, $(\partial^2 S/\partial^2 \rho)_T$ is positive in this EOS. The behaviors of the internal energies are similar (Figure 2.1B). The pressures of the two EOS are not significantly different at low temperature ($T = 4000$K) but the difference becomes larger at higher temperatures, which stems

from the difference in q (Figure 2.1C) ($(\partial P/\partial T)_\rho = \gamma C_V/V$ is proportional to ρ^{1-q}, derived from Equation 8, Section S1.1).

2.3.2 Mantle structure

Figure 2.2 shows a cross section of the Earth's mantle after the Earth reaches its equilibrium state ($\sim 1-2$ days after the impact). The cross-section lies on the $z = 0$ plane, which includes the center of the planet, and is perpendicular to the Earth's spin axis (z is parallel to the spin axis). The color gradient scales with the entropy gain and iron is shown in grey. As discussed in Section 2.2.4, the entropy is higher near the surface ($dS/dr > 0$). Thus, the mantle is thermally stratified (no convection). In (a), the impactor hits the surface of the Earth twice and becomes disrupted by the impact itself and the tide from the planet. The surface of the Earth is more shock-heated than the inner part partly because the surface is closer to the impact point and partly because the heavily shock-heated impactor envelops the surface of the Earth. In (b), the impact velocity is so high that the impactor penetrates all the way to the CMB (Figure 2.5, b1). This energetic impact strips off outer parts of the mantle, which is a desirable feature for producing a disk that is composed of the Earth's mantle rather than projectile. This strong impact heats the deep mantle materials, which are buoyant and come up to the surface, whereas the ambient colder materials flow to the inner region. Additionally, the outer part of the Earth's mantle is ejected in the z-direction after the impact, which eventually falls back and hits the surface of the Earth. These materials are highly shock-heated

through these processes and eventually distributed on the surface of the Earth. In (c), the two objects collide each other several times and eventually merge into a single planet. The mantle becomes highly shock-heated during these processes. The surface is more severely shock-heated because it is close to the impact points. Thus, although $dS/dr > 0$ is a common feature, the reasons for this state differ between the models.

The azimuthal dependence of the entropy is not significant. In (a), the impactor hits different parts of the mantle. Additionally, the mantle of the impactor, which is highly shock-heated, eventually falls on and covers the surface of the Earth's mantle. Through these processes, the Earth's mantle becomes approximately uniformly shock-heated. In (b), the mantle shows a slightly greater dependence than the other cases. The entropy difference at the same r can reach up to a couple of hundred J/K/kg, but it has only minor effects on the outcome (discussed in Section 2.4.2). In (c), the mantle is approximately uniformly heated through the multiple collisions.

The two EOS provide similar results for each type of impact. Figure 2.3 shows the entropy, density, temperature and pressure of the mantle. We set the minimum density $\rho_{\min}$ to avoid numerical problems, as described in the Section 2.6.4. In Figure 2.3A, $dS/dr > 0$ is clearly shown. Although the $MgSiO_3$ liquid EOS provides a slightly smaller entropy gain than the forsterite EOS, the entropy distribution is very similar between the two EOS (Figure 2.3A). A clear difference is that in the forsterite EOS, the mantle is "puffier" than in the $MgSiO_3$ liquid EOS in (b) and (c) (Figure 2.2), meaning that the forsterite EOS provides a broader region with small density (Figure 2.3B). The forsterite EOS has a higher temperature at a given r (Figure 2.3C), simply

because the temperature of the forsterite EOS needs to be higher to explain the same entropy as the perovskite EOS in the density range examined (Figure 2.1A). The pressure distributions are very close until reaching the outermost part (Figure 2.3D). Nevertheless, the overall physics of the two mantles are not significantly different. In addition to this, we also perform a simulation for (a) with an $MgSiO_3$ bridgmanite EOS and show that this result is similar to that of the $MgSiO_3$ liquid EOS (Section 2.6.3).

2.3.3 Mantle melting and mixing

Figure 2.3A shows that the majority of the mantle experiences melting ($\Delta S_{\rm melt} = 623$ J/K/kg). Specifically, the fractions of the mantle that are melted are (a) 68%, (b) 99 %, and (c) 100% for the $MgSiO_3$ liquid EOS and (a) 80%, (b)100%, and (c) 100% for the forsterite EOS (if $\Delta S_{\rm melt} = 500$ J/K/kg, the fractions become (a) 80%, (b) 100%, and (c) 100% for the $MgSiO_3$ liquid EOS and (a) 92%, (b)100%, and (c) 100% for the forsterite EOS. If $\Delta S_{\rm melt} = 200$ J/K/kg, the fractions become (a) 98% for the $MgSiO_3$ liquid EOS and the other cases are 100%). Therefore, even if there is no magma ocean prior to the impact, the base of the magma ocean is close to CMB in all cases. The analysis of the mantle mixing is summarized in Table 2.2. The potential energy is normalized by a constant ($0.01 \times \frac{1}{2} M_\oplus v_{\rm esc}^2$ where $v_{\rm esc}$ is the escape velocity of the Earth). $\Delta S_{\rm ave}$ represents the average entropy gain due to the impact. In (a), the ratio ΔPE/ΔKE is much greater than 0.5 in both EOS, which indicates that the mantle may remain unmixed. In (b), the ratio is still above the critical value, but

not as significantly. Given the uncertainties in our model, it is difficult to determine the stability of the mantle in this case. This would presumably indicate that the mantle or at least part of the mantle may remain unmixed. An important factor here, however, is that once an additional kinetic energy available to mix the mantle is considered, it becomes more likely that the mantle becomes mixed in (b) (discussed in Section 2.4.2). In (c), the ratio is much less than 0.5, which may lead to dynamical mixing of the mantle. Since ΔKE has larger variations than ΔPE among the models, the determining factor is the kinetic energy. The kinetic energies of the impacts determined by the different models rank as follows: (a) $<$ (b) $<$ (c) (Table 2.2). It should be noted that although the endpoints of the kinetic energy of the mantle in (b) and (c) are similar, ΔKE in (b) is significantly lower than that in (c) because the pre-impact Earth has a large amount of kinetic energy due to the rotation. Thus, our study indicates that the standard model (a) is most consistent, the sub-Earths model (c) may be least consistent with the preservation of the mantle heterogeneity, and the fast-spinning Earth (b) may lie between.

2.4 Discussion

2.4.1 A discrepancy between SPH and the Rankine-Hugoniot equations

The Rankine-Hugoniot equations describe the relations between pre- and post-shock states of materials (e.g., Tonks and Melosh, 1993; Stewart et al., 2014). The equa-

tions can predict the entropy increase of a shocked material by a small impact, but these equations do not model a giant impact very well. This is because the entropy increases by a giant impact not only because of the primary impact-induced shock, which provides the peak shock pressure (as shown in Figures 2.5 a1-c1 and 2.8), but also because of subsequent processes. Figure 2.4 shows a discrepancy between the Rankine-Hugoniot equations and SPH calculations. It exhibits the entropy of each SPH particle (shown in a dot) after the impact as a function of the shock peak pressure. The lines represent predictions of entropy gain using the Rankine-Hugoniot equations (Sugita et al. 2012, see Section 2.6.5). It is shown that the entropy gain predicted by SPH is generally much larger than the predictions by the equations, especially in (b) and (c). This is because the mantle is heated due to a number of additional processes, such as reflected shock waves within the Earth as well as planetary deformation followed by gravitational potential energy release. The latter effect is clearly shown in Figure 2.5, which represents the pressure evolution during the giant impact. In (b) and (c), after the impact, a large fraction of the Earth's mantle experiences an extensive expansion and becomes subject to low pressure (b2 and c2). Subsequently, the part falls back towards the Earth's core and gains a high pressure (b3 and c3). Through these processes, the part of the mantle efficiently gains entropy. In (a), the extent of such deformation is not as prominent as the other cases; therefore, its entropy increase is closer to the analytical estimates. The time dependent relationship between the pressure and entropy is discussed further in Section 2.6.6. Thus, the Rankine-Hugoniot equations of state predict only a part of the entropy

gain (due to the primary impact-induced shock); therefore they do not represent the total entropy gain by a giant impact.

2.4.2 Mixing analysis

For this mixing analysis, we assume that ΔKE is the kinetic energy of the differential rotation of the mantle. However, differential rotation is not the only source of energy available for mixing. In addition to flows produced by the impact itself, there will be excitation of normal modes of the planet (we have observed these in longer runs of SPH simulations for close encounters or glancing impacts). These are analogous to waves on an ocean and have an energy that oscillates between gravitational energy and kinetic energy of the fluid motion, with equipartition of the average kinetic energy and average gravitational energy. The mean kinetic energy is therefore simply related to the gravitational energy for a distortion of an equipotential surface or the planet as a whole by a vertical distance h. These normal modes will "ring down" slowly, but in a region of static stability the distortion of equipotential surfaces creates horizontal density gradients that drive rapid baroclinic instabilities. Thus, some significant fraction of this energy (the precise amount is not easily estimated) can go into mixing. Here we make a simple estimate for the additional kinetic energy for mixing: the gravitational energy by distortion for a uniform density sphere is proportional to $\frac{GM_\oplus^2}{R_\oplus}(\frac{h}{R_\oplus})^2$. Approximately, $\frac{h}{R_\oplus}$ is ~ 0.1 in (a) and > 0.3 in (b) and (c). Thus, the gravitational energy becomes $\sim$ 1, 10 and 10 (in 0.01 $\times \frac{1}{2} M_\oplus v_{\rm esc}^2$, which is the unit of ΔKE in Table 2.2). Assuming that approximately half of this energy eventually

goes into heat and the other half is available to mix the core (this increases ΔKE), corrected ΔPE/ΔKE become 1.60, 0.35, and 0.17 in (a), (b) and (c) ($MgSiO_3$ liquid EOS). Thus, the mantle would still remain unmixed in (a), but the mantle would be mixed in (b) and (c).

We ignore the azimuthal dependence, which is likely a reasonable approximation. To demonstrate that the approximation is feasible, consider the worst case, the mantle in (b), whose entropy distribution shows the strongest azimuthal dependence. We evenly divide the mantle into four sections according to its azimuthal angle. We observe that the average ΔPE in each section differs from the globally averaged value by less than 10%, which is not sufficient to alter the mixing status. Another potential concern is that we only perform one simulation for each model and EOS, therefore it is possible that the ratio ΔPE/ΔKE varies among models, but we show that the ratio we derived is likely to capture the general trend (discussed in Section 2.6.7).

It should be noted that the mixing analysis described in Section 2.3.3 only determines the global mixing state. Therefore, it may be possible to preserve a local heterogeneity even at ΔPE/ΔKE < 0.5, especially if the ratio is close to the critical value. Unfortunately, our SPH does not provide information about local mixing. To investigate such local mixing, it would be necessary to perform a simulation with much higher resolution, but doing so would be computationally quite expensive. Additionally, we do not consider the possibility that the mantle was compositionally stratified before the impact (e.g. a denser layer at the base of the mantle), but if this was the case, it could increase the stability of the mantle. Moreover, we discuss issues

and implications of this mixing analysis in Section 2.6.7.

2.4.3 Mixing during subsequent cooling

We turn now to the question of whether the mantle will mix during the post-giant impact cooling. This is a simple problem, conceptually, and it does not require extensive numerical analysis. As the outer regions of Earth cool, the mantle will evolve into two regions, a nearly isentropic region that can convect and a deeper region where the entropy is still lower than that appropriate for the effective radiating temperature of Earth at that time. The deeper region that is of lower entropy is unable to convect since it is still part of the stably stratified zone. Thus, the convective zone propagates downwards as the planet cools and the deepest part of the mantle is only able to convect when the entire region above has cooled to the entropy that this deepest part had immediately after the giant impact. But as we have seen, this entropy is not much larger than it was before the giant impact, at least in the case of the canonical giant impact. This takes a long time relative to the time it takes to make the Moon, as we now demonstrate. Let T_e be Earth's effective temperature for the thermal state corresponding to the isentrope that is only slightly higher (and hotter) than the pre-giant impact state. At that epoch, the cooling equation takes the form

$$4\pi R^2 \sigma T_e^4 = -\frac{d}{dt}(M C_V T_{\rm m}) \tag{2.4}$$

where M is the mantle mass and $T_{\rm m}$ is the mean temperature at that epoch. Accordingly, the time τ that takes to cool an amount $\Delta T_{\rm m}$ is

$$\tau \sim 5 \times 10^3 \left(\frac{\Delta T_{\rm m}}{1000{\rm K}}\right) \left(\frac{1000{\rm K}}{T_e}\right)^4 {\rm yrs} \tag{2.5}$$

This is an underestimate because we assume a typical specific heat rather than the additional term that comes from freezing. Importantly, T_e can be low at this point, though its exact value depends on whether there is a steam atmosphere. For example, at T_e= 500K, this cooling time for 1000K is tens to hundreds of thousands of years, which is much longer than the estimated time for making the moon (hundreds to thousands of years). The reason for this is obvious: Earth's mantle has a much greater heat capacity than the Moon-forming disk and yet a smaller area from which to cool. This is the time that must elapse before any mixing of the deepest mantle material can even begin. Even at that time, mixing will not occur if there is a basal magma ocean prior to the impact. It is often assumed in the literature that mixing occurs if there is liquid but it is important to stress that the state of the material is not the crucial issue here. Counterintuitive though it may seem, it is harder to mix a stably stratified liquid than to mix a solid of the same stratification because the thermal anomalies associated with convection in a liquid are much smaller than those for solid state convection.

2.4.4 Impactor's isotopic signature

For the standard scenario (a), the impactor needs to have isotopic signatures similar to those of the Earth to explain the geochemical evidence. To gain a better idea of how likely this similarity could be in the Grand Tack model, we run similar analyses to those of Pahlevan and Stevenson (2007). Although Kaib and Cowan (2015) have conducted isotopic analyses of a model that is similar to the Grand Tack, the initial conditions are more simplified than the original model.

We take 30 planets from eight simulations from Walsh et al. (2011) (each simulation produces three to four terrestrial planets) and examine the difference in the oxygen isotope ratios between the target and impactor. We assume that the oxygen isotopic ratio in the protoplanetary disk linearly varies as a function of the heliocentric distance r', $\Delta^{17}\mathrm{O}(r') = c_1 \times r' + c_2$. Two pairs of c_1 and c_2 are used; case 1: c_1 and c_2 are chosen such that $\Delta^{17}\mathrm{O}(r') = 0$ ‰ at 1 AU and $\Delta^{17}\mathrm{O}(r') = 0.321$ ‰ at 1.5 AU(Δ^{17}O of Mars), and case 2: c_1 and c_2 are chosen such that the Earth and Mars analogues in each simulation have $\Delta^{17}\mathrm{O}(r') = 0$ ‰ and 0.321 ‰, respectively (this is the same setting as those of Pahlevan and Stevenson 2007). Simulations that do not produce Mars analogues are discarded. Figure 2.6 shows histograms of the differences in the oxygen isotopic ratios. The top and bottom planes correspond to case 1 and case 2. The left panels include all of the impacts and the right panels focus on the last giant impact for each planet. Even if we take the stricter criterion (the isotopic difference should be less than 0.005 ‰), there is one last giant impact out of 30 events and one out of 19 events that satisfy this criterion in case 1 and case

2, respectively (Figure 2.6 right panel). It should be noted that the mass involved in these particular impacts are a couple of Mars masses, so that these do not mimic the Moon forming impact. Nevertheless, this simple analysis may indicate that the Grand Tack model could produce an impactor that has a similar composition to the Earth and its possibility is around 3-5 %. Needless to say, a much larger dataset is needed to estimate the probability. Additionally, other isotopic ratios, such as tungsten and silicon, need to be explained in addition to oxygen (Section 5.1).

2.5 Conclusions

To investigate the relationship between the Moon-forming model and geochemical evidence, we have investigated the initial state of the Earth's mantle after the Moon-forming impact. Giant impact simulations using the SPH method are performed with the $MgSiO_3$ liquid and forsterite equations of state. Three impact models are considered here: (a) standard, (b) fast-spinning Earth, and (c) sub-Earths. We find that the mantle becomes mostly molten after the Moon-forming impact in all of the cases. It is also shown that the impact-induced entropy gain of the mantle cannot be predicted well by the Rankine-Hugoniot equations. Based on our analysis on the energy balance of the mantle, we find that the Earth's mantle is likely to stay unmixed in (a), while it may be mixed in (b) and (c). The extent of mixing is most extensive in (c). This is primarily because the impact-induced kinetic energy in (c) is much larger than that of (a) while (b) falls between. Thus, the standard model (a) is most consistent, the sub-Earths model (c) may be least consistent with the preservation of

	$M_{\rm i}/M_{\rm T}$	$M_{\rm T}$	b	$v_{\rm imp}$	$\tau_{\rm spin}$
(a) Standard	0.13	1.02	0.75	1.0	0
(b) Fast-spinning Earth	0.045	1.05	-0.3	20 (km/s)	2.3
(c) Sub-Earths	0.45	1.10	0.55	1.17	0

Table 2.1: The initial conditions of the impact. $M_{\rm i}/M_{\rm T}$ is the impactor-to-total mass ratio, $M_{\rm T}$ is the total mass scaled by the mass of the Earth, b is the scaled impact parameter, $v_{\rm imp}$ is the impact velocity scaled by the escape velocity (except b), and $\tau_{\rm spin}$ is the initial spin period of the target (hrs).

	ΔKE	ΔPE	ΔPE/ΔKE	$\Delta S_{\rm ave}$
(a1) Standard, liq	1.38	3.01	2.18	1181
(a2) Standard, for	1.51	2.82	1.86	1220
(b1) Fast-spinning Earth, liq	3.08	2.79	0.91	1645
(b2) Fast-spinning Earth, for	3.36	2.45	0.73	1675
(c1) Sub-Earths, liq	5.85	1.85	0.32	2210
(c2) Sub-Earths, for	5.50	1.26	0.23	2196

Table 2.2: The outcomes of the impact. ΔKE is the change in kinetic energy (normalized by $0.01 \times \frac{1}{2} M_\oplus v_{\rm esc}^2$, where $v_{\rm esc}$ is the escape velocity of the Earth) and ΔPE is the potential energy required to mix the mantle. $\Delta S_{\rm ave}$ is the average entropy gain of the mantle. liq represents the $MgSiO_3$ liquid and for represents forsterite EOS.

the mantle heterogeneity, and the fast-spinning Earth (b) may lie between. We also find that if the impact does not mix the mantle, the Earth's mantle would remain partially unmixed for more than the Moon accretion time scale ($\sim 100 - 1000$ yrs). It is therefore possible, at least in the standard giant impact case (and possibly some others), to avoid complete mixing during and immediately after a giant impact. The issue of subsequent mixing ($>\sim$ 1000 yrs) is not a simple problem but is no different from the usual assessment of mantle convection mixing (e.g., Tackley, 2012).

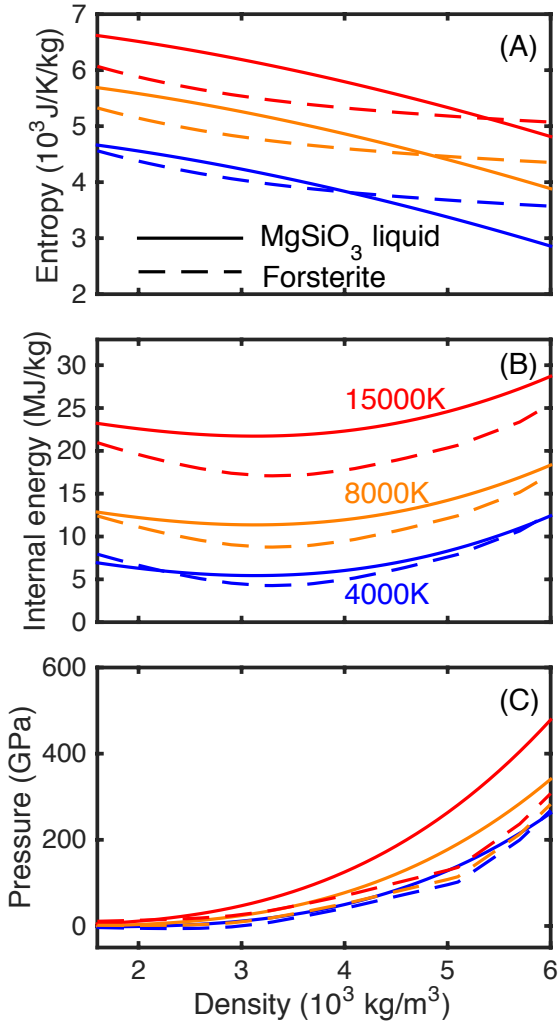

Figure 2.1: The two equations of state at various temperatures. The blue, orange and red lines correspond to 4000 K, 8000 K, and 15000 K, respectively. The solid and dashed lines represent the $MgSiO_3$ liquid and forsterite EOS.

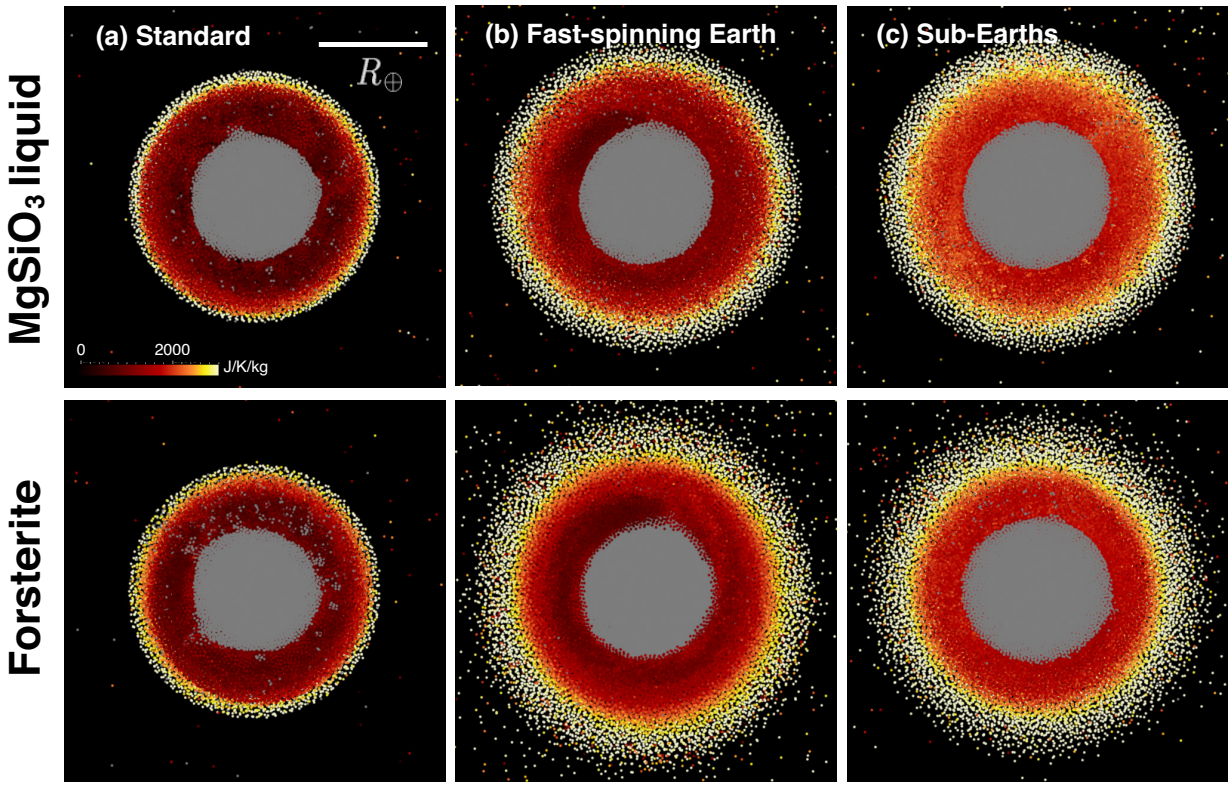

Figure 2.2: Cross-section of the mantle after the impact. The color gradient scales with the entropy gain of the mantle material. Iron is shown in grey. The top panels show the case with the $MgSiO_3$ liquid EOS and the bottom panels show the case with the forsterite EOS.

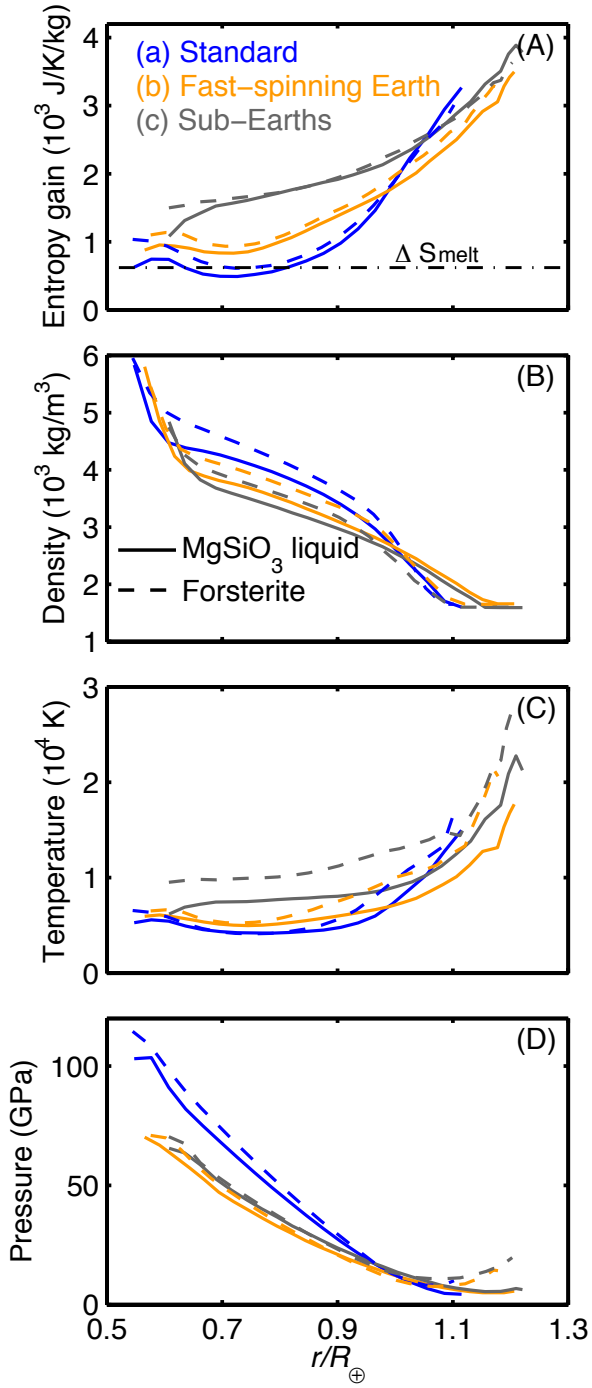

Figure 2.3: Mantle structure as a function of r. The blue, orange and grey lines represent the standard, fast-spinning and sub-Earth cases. The solid and dashed lines represent the $MgSiO_3$ and forsterite EOS. The dash-dot line represents the entropy of melting. Although the density and temperature are slightly different, the entropy is quite similar for the different EOS. The pressure is also nearly the same except for the outer boundary.

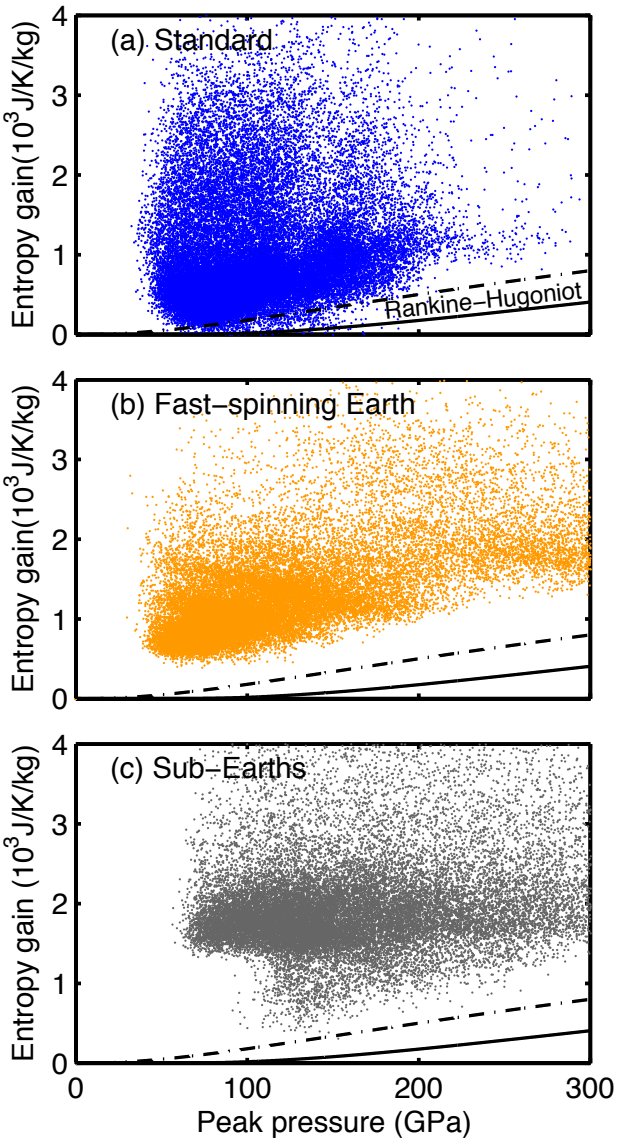

Figure 2.4: Entropy gain of each SPH particle in the mantle with the $MgSiO_3$ liquid EOS. The dashed ($p_i = 0$ GPa) and solid ($p_i = 50$ GPa) lines represent estimated entropy gain based on the Rankine-Hugoniot equations, where p_i is the pre-shock pressure. To examine the lower part of the mantle, this figure only shows SPH particles that were initially under high pressure (> 24 GPa) before the impact.

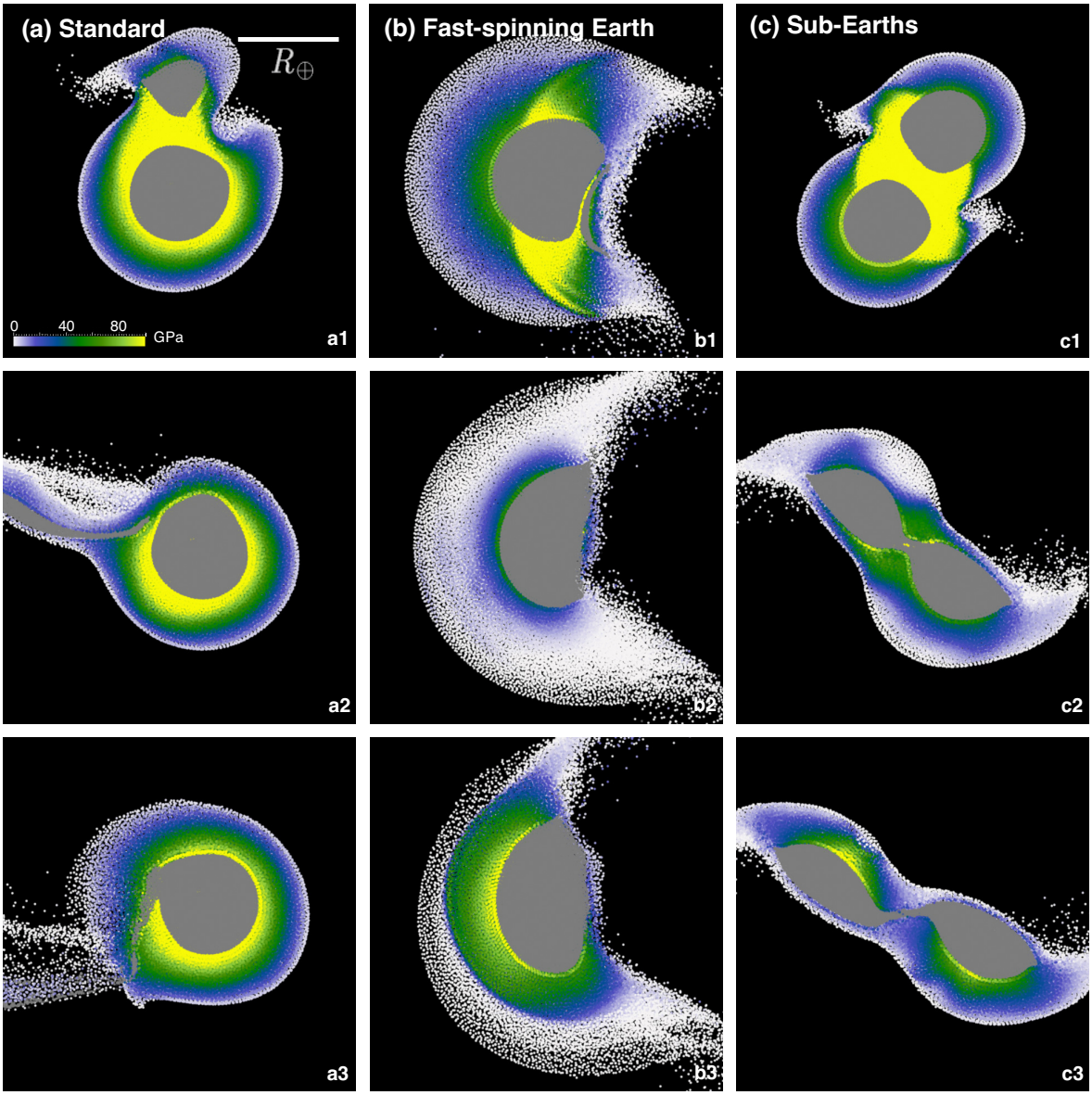

Figure 2.5: Snapshots of early stages of the impacts (a1-3: 0.62, 1.0, 1.5 hrs, b1-3: 0.37, 0.60, 0.70 hrs, and c1-3: 0.33, 0.60, 0.72 hrs after the start of the simulation). The color gradient scales with the pressure of the mantle material and iron is shown in grey. The Earth deforms significantly and experiences low pressure in (b) and (c) while the deformation is less intense in (a).

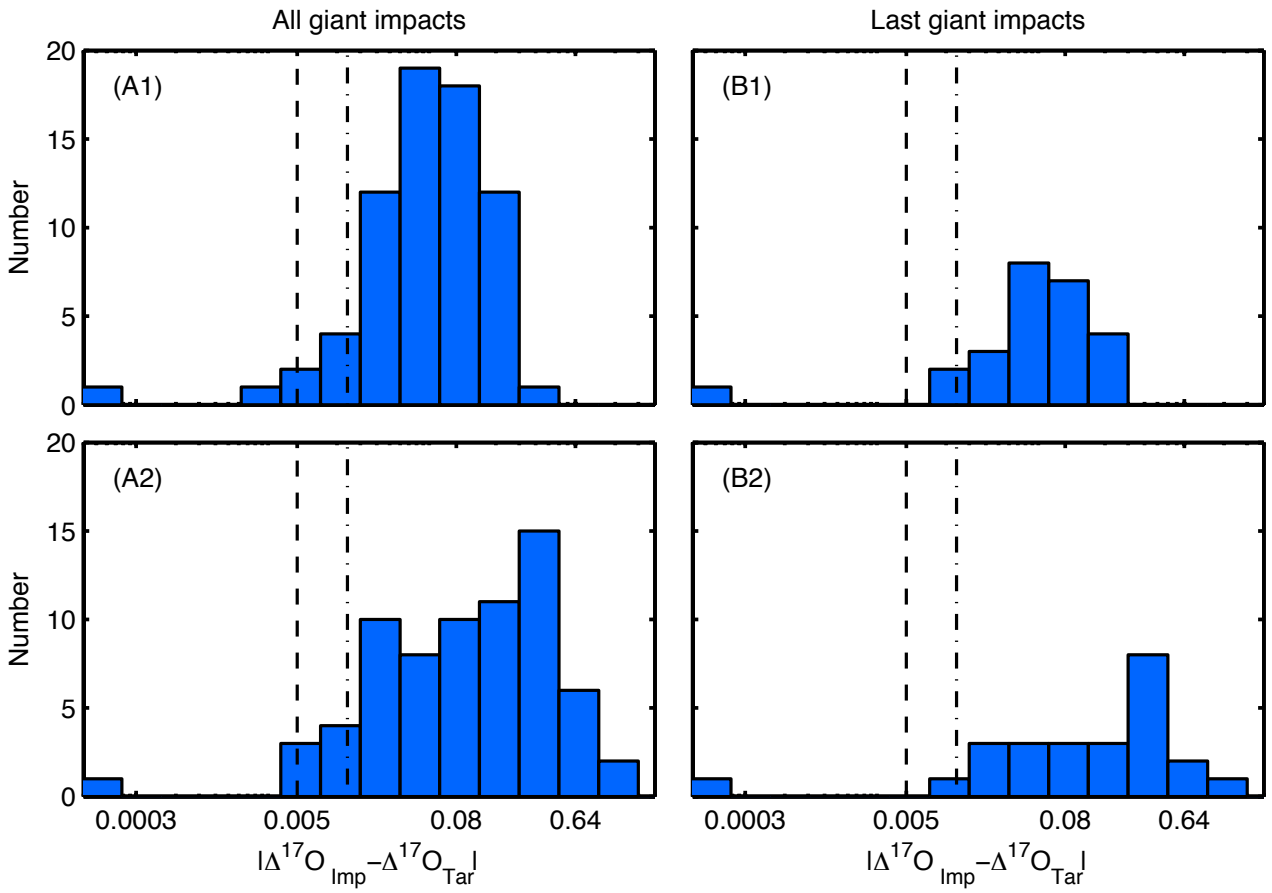

Figure 2.6: Histogram of the differences in the oxygen isotopic ratios between the target (proto-Earth) and impactor. The left panel includes all of the giant impacts and the right panel includes only the last giant impact for a planet. The top and bottom panels represent different initial conditions (case 1 and case 2, Section 2.4.4). The dashed and dash-dot lines indicate the two estimates of the oxygen isotopic differences between the Earth and Moon (0.005‰ and 0.012‰, respectively, Wiechert et al. 2001; Herwartz et al. 2014).

2.6 Supplementary Materials

2.6.1 Equation of state

Our equation of state for the $MgSiO_3$ liquid follow the formulae previously derived (e.g., de Koker and Stixrude, 2009; Stixrude et al., 2009). The Helmholtz free energy is written as

$$F(V,T) = F_0 + F_{\rm cmp}(V,T_0) + F_{\rm th}(V,T), \tag{2.6}$$

where $F_0 = F(V_0,T_0)$ is the free energy at the reference volume, V_0, and temperature, T_0. $F_{\rm cmp}(V,T_0)$ and $F_{\rm th}(V,T)$ are the compressional and thermal contributions to the free energy, respectively. $F_{\rm cmp}$ is

$$F_{\rm cmp} = 9K_{T0}V_0\left(\frac{1}{2}f^2 + \frac{1}{6}a_3 f^3\right), \tag{2.7}$$

where

$$a_3 = 3(K'_{T0} - 4), \tag{2.8}$$

$$f = \frac{1}{2}\left[(V_0/V)^{2/3} - 1\right]. \tag{2.9}$$

K_{T0} is the isothermal bulk modulus (at $T = T_0$), and $K'_{\rm T0}$ is its pressure derivative at $p = 0$ and $T = T_0$. $F_{\rm th}$ is written as

$$F_{\rm th} = -\int_{T_0}^{T} S(V,T')dT'. \tag{2.10}$$

The entropy $S(V,T)$ is described as

$$S(V,T) = S_0 + \int_{V_0}^{V} \frac{C_V \gamma(V', T_0)}{V} dV' + \int_{T_0}^{T} \frac{C_V(V,T')}{T'} dT', \tag{2.11}$$

where $S_0 = S(V_0, T_0)$, and C_V is the specific heat that is assumed to be a constant. γ is the Grüneisen parameter, which is described as

$$\gamma = \gamma_0 \left(\frac{V}{V_0} \right)^q, \tag{2.12}$$

where, γ_0 and q are constants.

The internal energy, E, and pressure, P, are described as

$$E(V,T) = E_0 + 9K_{T0}V_0 \left(\frac{1}{2}f^2 + \frac{1}{6}a_3 f^3 \right) + C_V(T - T_0) + C_V T_0 \int_{V_0}^{V} \frac{\gamma(V', T_0)}{V'} dV', \tag{2.13}$$

$$P(V,T) = 3K_{T0}(1+2f)^{5/2}(f + \frac{a_3}{2}f^2) + C_V(T - T_0)\frac{\gamma(V, T_0)}{V}. \tag{2.14}$$

Here, $E_0 = E(V_0, T_0)$. $\rho_0 = (1/V_0)$, T_0, K_{T0}, K'_{T0}, C_V, γ_0, q, E_0, and S_0 are listed in Table 2.3.

ρ_0(kg/m^3)	$T_0(K)$	K_{T0}(GPa)	K'_{T0}	C_V(J/K/kg)	γ_0	q	E_0(MJ/kg)	S_0(kJ/K/kg)
2650	2000	27.3	5.71	1480	0.6	-1.6	2.64	3.33

Table 2.3: Parameters for the $MgSiO_3$ liquid EOS.

2.6.2 Mixing criterion

In a simple shear flow, the criterion for a Kelvin-Helmohltz instability (effectively the criterion for mixing) is $Ri \equiv N^2/(du/dz)^2 < 1/4$. Ri is the Richardson number of the system, N is the Brunt-Vaisala frequency, $N^2 \equiv -g(d\rho/dz)/\rho$, u is the velocity, z is the direction perpendicular to the flow, g is the gravity, and ρ is the density. Ri is related to the ratio of potential energy to kinetic energy (e.g., Taylor, 1931; Chandrasekhar, 1961) and is normally defined in terms of fluids with well defined constant density differences or a density gradient, but our system has variable values of all the input parameters. Therefore, we must necessarily restate the problem in terms of the energy budgets rather than explicitly in terms of velocity shear. The kinetic energy difference ΔKE per unit area for a layer of thickness L between the initial state (with shear) and the final state (with no shear but the same linear momentum) is

$$\frac{1}{2}\overline{\rho}\int_{-L/2}^{L/2}(u(z)^2 - (u_0/2)^2)dz = L\overline{\rho}u_0^2/24, \tag{2.15}$$

where u_0 is the initial velocity difference between the top and bottom and $\overline{\rho}$ is the mean density. The gravitational potential energy difference (ΔPE) between initial and final (fully mixed) states is

$$\int_{-L/2}^{L/2}(\overline{\rho} - \rho(z))gzdz = \rho N^2 L^3/12, \tag{2.16}$$

where the density variation is assumed small. Therefore, the Richardson number criterion becomes ΔKE>2ΔPE and the physical interpretation is that one must provide not only the energy to overcome the potential energy difference but also the energy to mix (which shows up as heat from the dissipation of small scale turbulent motions). In the analysis provided by Chandrasekhar (1961) (p. 491), the ΔPE he defines is for complete overturn (that is, the new density profile is the exact opposite of the initial density profile), which is a different setting from ours. Therefore, his criterion differs from ours (mixed if ΔKE > ΔPE in his anaysis).

2.6.3 $MgSiO_3$ bridgmanite EOS

Figure 2.7 shows cross-sections of the mantles after the impact with the $MgSiO_3$ liquid and $MgSiO_3$ bridgmanite EOS. The thermodynamic parameters for the bridgmanite EOS is listed in Table 2.4. The entropy gains are slightly different, but the extent of shock-heating and the feature of $dS/dr > 0$ are similar among these cases. One might expect that a liquid mantle may gain higher entropy than a solid mantle based on the study done by Karato (2014). His work suggests that the surface of a molten mantle gains higher entropy by impact than a solid surface due to its smaller sound speed C_0 and negative q for the liquid (for the definition of C_0, see Section 2.6.5).

However, the difference in C_0 between the two EOS becomes smaller at a greater depth. This would diminish the difference between the entropy gained by the mantles with the two EOS. In addition, Karato (2014) use the Rankine-Hugoniot equations to describe the physics of the planetary surface, but we cannot use these equations

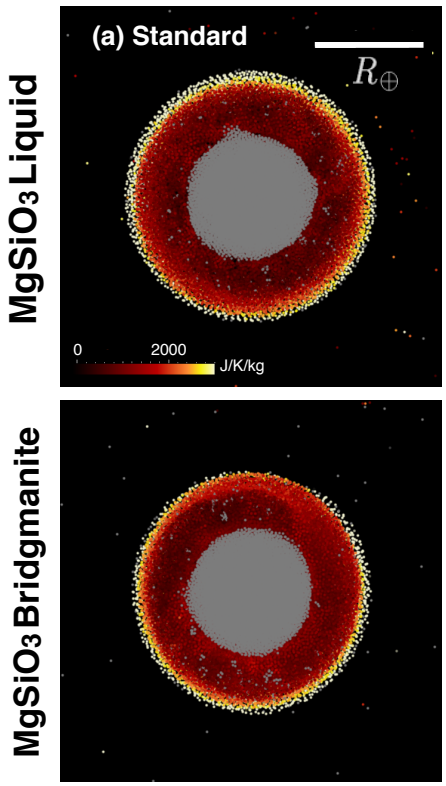

Figure 2.7: Entropy of the Earth's mantle after the impact. The top panel shows the case with the $MgSiO_3$ liquid EOS (this is the same as the top panel of Figure 2a) in the main text, and the bottom panel shows the case with the $MgSiO_3$ bridgmanite EOS.

ρ_0(kg/m^3)	$T_0(K)$	K_{T0}(GPa)	K'_{T0}	C_V(J/K/kg)	γ_0	q	E_0(MJ/kg)	S_0(kJ/K/kg)
3680	2000	200	4.14	1200	1.0	1.0	1.995	2.63

Table 2.4: Parameters for the equation of state of $MgSiO_3$ bridgmanite.

to predict the entropy gain of the entire mantle as discussed in Section 4.1.

2.6.4 Correction of the outer boundary

The density of the outer edge of the mantle is corrected because the simulation itself does not provide an accurate value. One of the reasons is that the standard SPH

cannot describe a large density difference (e.g., CMB or planet-space boundary). The density of a particle at the outer boundary becomes too small because the particle does not have many nearby particles; thus, the smoothing length becomes large. This leads to a problem that dP/dr at the outermost part of the mantle becomes nearly 0 or it even becomes positive in (b) and (c) (Figure 3D). This state is not physically sensible because the hydrostatic equation is not correctly solved in the region.

To avoid this numerical problem, we define the minimum density $\rho_{\rm min} = \rho(r_{\rm max})$. Here, $r_{\rm max}$ is the maximum r whose region satisfies $dP/dr < 0$. If the density at $r > r_{\rm max}$ is lower, the r is recalculated by setting $\rho = \rho_{\rm min}$ and conserving the mass. Typically, $\rho_{\rm min} \sim 1500 - 1600$ kg/m^3 (Figure 3B). This is uncertain but may be reasonable because this is close to a rough estimate of the density at such a high temperature. The density at the outer edge can be approximated as $\rho \sim \rho_0(1-\alpha T) \sim 1577$ kg/m^3 at $\alpha = 2.7\times10^{-5}$ (Fiquet et al., 2000), $\rho_0 = 2650$ kg/m^3, and $T = 1.5\times10^4$ K. After this procedure, ΔPE in the two EOS become similar. Thus, although this approximation is simple, it provides a reasonable answer.

2.6.5 The Rankine-Hugoniot equations

Sugita et al. (2012) derive the following differential equations to describe after-shock temperature T and entropy S based on the Rankine-Hugoniot equations;

$$\frac{dT}{dU_p} = C_0\gamma_0 T\frac{(U_s - U_p)^{q-1}}{U_s^{q+1}} + \frac{sU_p^2}{C_V U_s}, \tag{2.17}$$

$$\frac{dS}{dU_p} = \frac{sU_p^2}{TU_s}. \tag{2.18}$$

Here, $p = p_i + \rho_i U_s U_p$ and $\rho = \rho_i U_s/(U_s - U_p)$, where p_i, ρ_i, U_s, and U_p are the pre-shock pressure, pre-shock density, shock velocity and particle velocity. U_s and U_p has a relation $U_s = C_0 + sU_p$, where C_0 and s are the sound speed and constant. For our calculations, we choose $s = 1.56$ (for $MgSiO_3$ bridgmanite, Deng et al. 2008) and $T_i = 2000$ K (pre-shock temperature). At $p_i = 0$ GPa, $\rho_i = 4100$ kg/m^3, $C_0 = 6.47$ km/s and at $p_i = 50$ GPa, $\rho_i = 4500$ kg/m^3, $C_0 = 9.0$ km/s.

2.6.6 Pressure vs. entropy increase

Figure 2.8 shows the relationship between the pressure (shown in grey) and entropy gain (shown in green). We choose a specific SPH particle from each simulation and track its properties. In (a), the primary impact, whose shock peak pressure is ~ 90 GPa, is the major source for the entropy increase. The entropy changes overtime, but the extent is limited. In (b), the SPH particle is heated by multiple shocks, including the primary impact-induced shock and shocks due to the planetary expansions and contractions (discussed in Section 4.1). After ~ 5 hrs, the entropy slowly increases due to continuous small-scale planetary deformation (the planet continues to wobble) until the system reaches its equilibrium state. In (c), the SPH particle experiences a number of shocks because the target and impact collide several times. The entropy gain is larger than the other two cases.

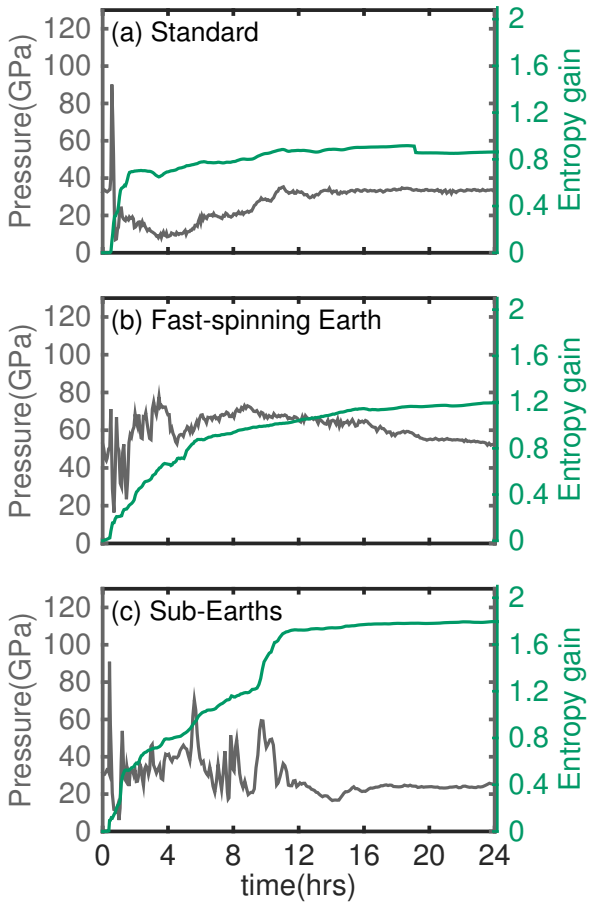

Figure 2.8: Time dependence of the pressure and entropy (in 10^3 J/K/kg) of an SPH particle in each model during the initial 24 hours.

2.6.7 Further discussions on the mixing analysis

We assume that the Earth's mantle was chemically heterogeneous before the impact, but here we further discuss its plausibility. Unlike (a) or (c), the model (b) requires that the Earth spins very quickly before the giant impact. This may indicate that the Earth experienced another (older) giant impact before the Moon-forming impact. This is because the angular momentum of a planet delivered by a number of small impacts from random directions tend to cancel out. This older giant impact could have been similar to the "sub-Earths" model, meaning that two similar mass objects collided, because this type of an impact is one of the easiest ways to deliver a large angular momentum to the planet (Canup, 2014). If this is the case, Earth's mantle could have been homogenized before the Moon-forming impact. If the heterogeneity formation predated this older impact, this could be a potential problem for (b). Alternatively, it is also possible that the heterogeneity formed between this older and the Moon-forming giant impacts, possibly in the form of a basal magma ocean by fractional melting and crystallization processes. The re-establishment of a compositionally distinct basal magma ocean could have been accomplished in less than 10^6 yr compared to the likely time between giant impacts plausibly $\sim 10^7$ years (without an atmosphere, the majority of the mantle could have crystallized as short as 10^3 years, Solomatov 2000). It should be noted that there is no reason to suppose that this older impact was immediately prior, but the time interval might have been preferably short if the older impact formed a satellite. This is because the interaction between the Earth and satellite may have slowed the Earth's spin rate within $10^6 - 10^7$ years

(Canup, 2014). This older satellite might have merged with a newer satellite formed by the last giant impact (Citron et al., 2014).

Another potential problem is that the critical value 0.5 has been derived to analyze the stability of horizontally stratified layers, but the value can differ for spherically stratified layers, as in our model. However, there is no literature concerning this geometry; thus, we simply apply the critical value for our analyses. The choice of the minimum density could also affect the estimate of ΔPE.

Furthermore, we only perform one simulation for each model and EOS. It is possible that ΔKE and ΔPE can change even for the same type of impact depending on the choice of the initial conditions (e.g., $v_{\rm imp}$ and b). To perform a simple and crude analysis, here we assume that the planetary kinetic energy is expressed as $\frac{1}{2}I\omega^2$, where I is the moment of inertia and ω is the angular velocity of the planet, and that I and ΔPE do not vary in the same model. We compute the ratio of ΔPE/ΔKE based on ω from published successful simulations (Ćuk and Stewart, 2012; Canup, 2012) and find that most of these simulations do not change the ratio large enough to cross the critical value 0.5, except Run 14 ($M_{\rm i}/M_{\rm T} = 0.45$, $b = 0.40$, and $v_{\rm imp}/v_{\rm esc} = 1.4$) in the sub-Earths model, depending on the EOS (0.52 for $MgSiO_3$ liquid and 0.38 for forsterite). Thus, our results likely provide the general trend, but some outlier may exist. Nevertheless, the choice of initial conditions is not likely to alter the signatures of $dS/dr > 0$ or the melting of the nearly entire mantle because these are states less sensitive to the conditions.

Chapter 3

Initial state of the Moon-forming disk

3.1 Introduction

The widely accepted explanation for the origin of the Moon is the giant impact hypothesis, which involves a collision between the proto-Earth and an impactor during the late stage of terrestrial planet formation (Hartmann and Davis, 1975; Cameron and Ward, 1976). A number of numerical simulations of giant impacts have been performed to test this hypothesis (Benz et al., 1986, 1987, 1989; Cameron and Benz, 1991; Canup and Asphaug, 2001; Canup, 2004, 2008b). Typically, a Mars-sized impactor hits the proto-Earth with a small impact velocity and large impact angle. The ranges of the impact velocity and angle are relatively limited because the angular momentum of the system is thought to be conserved over time (e.g., Canup et al., 2001). The typical outcome of these simulations is that the impactor is tidally disrupted, partly by tides and partly by the shock-induced flows, and creates a massive iron-depleted circumplanetary disk, from which the Moon is subsequently accreted. In this paper, we call this model the "standard" scenario. This model can potentially explain several observed features, such as the Moon's mass and iron depletion, as well as the angular momentum of the Earth-Moon system.

The standard model might fail to explain the observed isotopic similarities of the Earth and Moon. According to these simulations, most of the disk materials originate from the impactor, which is likely to have different isotope ratios from the proto-Earth. Then, the Moon should primarily inherit the isotopic signature of the projectile. This seemingly contradicts the nearly identical isotopic ratios of oxygen, silicon, tungsten, and titanium observed for the Earth and Moon (Wiechert et al.,

2001; Armytage et al., 2012; Touboul et al., 2007; Zhang et al., 2012). A recent study shows that a giant impact with a smaller impact angle and larger impact velocity could lead to a disk that mainly originates from proto-Earth (Reufer et al., 2012), but this model still has difficulty with explaining such strong isotopic similarities.

Pahlevan and Stevenson (2007) suggest mixing have occurred between the disk and Earth's mantle through the connected atmosphere. This process could have homogenized the isotopic ratios, such as oxygen. However, this model may have difficulty explaining the silicon isotopic ratios (Pahlevan et al., 2011; Halliday, 2012). It is also unclear whether the mixing is sufficiently efficient to accomplish the isotopic similarity even for oxygen, especially because this requires efficient homogenization all the way from the deep mantle of the Earth to the outermost half of the disk mass.

Recently, new dynamical models have been suggested for the origin of the Moon. Ćuk and Stewart (2012) propose a model in which an impactor hit a rapidly rotating, and hence oblate, proto-Earth (called the "fast-spinning Earth"), whereas Canup (2012) suggests a giant impact between two objects with half Earth's mass (hereafter "sub-Earths"). In these models, the composition of the disk is similar to that of the Earth, so that the isotopic similarities can be potentially explained. In these studies, the angular momentum of the Earth-Moon system is approximately three times larger than its present-day value. Ćuk and Stewart (2012) suggest that the evection resonance between the Moon and the Sun can transfer excess angular momentum from the Earth-Moon system to the Sun-Earth. This is the resonance that occurs when the precession period of the Moon's pericenter is equal to the Earth's orbital period

(Touma and Wisdom, 1998). The efficiency of this angular momentum transfer may depend on a fortuitous choice of tidal parameters and their constancy with time, but we set aside this concern in this paper.

To bridge such dynamical models and the resulting properties of the Moon, the thermodynamics of the Moon-forming disk needs to be understood. The thermal structure of the disk affects the Moon-forming process and, hence, the chemical and isotopic compositions of the Moon. As an example, the initial entropy of the disk may control the volatile content of the disk. In a disk without radial mass transport or loss to infinity, the initial entropy will not matter since a high-entropy disk will simply cool to reach the same thermodynamic state as an initially low-entropy disk. However, the interplay of cooling and transport can be expected to affect the fate of the volatile components. This is important for explaining the volatile depletion of the Moon (Ringwood and Kesson, 1977). Additionally, the isotope mixing occurs more efficiently in the high-entropy, and hence, vapor-rich disk (Pahlevan and Stevenson, 2007).

The disk structure and its evolution have been studied analytically and numerically (e.g., Thompson and Stevenson, 1988; Ida et al., 1997; Kokubo et al., 2000; Pritchard and Stevenson, 2000; Genda and Abe, 2003; Machida and Abe, 2004; Ward, 2012; Salmon and Canup, 2012), but such previous studies are not directly connected with the giant impact modeling. Rather, these studies assume a circumplanetary disk as the initial condition. This discrepancy hinders deriving a realistic disk structure consistently.

The aim of this paper is to derive, for the first time, the initial thermal structures of Moon-forming disks directly from giant impact simulations. First, we perform various giant impact simulations and then derive the hydrostatic disk structures based on the numerical results. Here we focus on four cases: (a) standard, (b) fast-spinning Earth, (c) sub-Earths, and (d) intermediate. Case (d) is a collision of two bodies whose mass ratio is 7:3, which is similar to one of the calculations performed by Cameron (2000). Lastly, we explain a simple semi-analytic model that describes the thermal structure of the disk.

3.2 Model

The disk structure is derived in two steps. First, giant impact simulations are performed using Smoothed Particle Hydrodynamics (SPH) (e.g., Lucy, 1977; Gingold and Monaghan, 1977; Monaghan, 1992). The details of SPH are summarized in Section 3.2.1. The endpoint of each simulation provides mass, angular momentum, and entropy distributions that form the starting point to determine the disk structure.

3.2.1 SPH integrated with GRAPE

SPH is a Lagrangian method in which the fluid is modeled by numerous moving particles (grids). A particle i has a mass m_i and the so-called smoothing length, h_i. The mass m_i is distributed in a sphere of radius $2h_i$. h_i is defined such that approximately 50 neighboring particles are included in the sphere. Increasing the number of particles near particle i decreases h_i. The momentum and energy equations are solved at each

time step. The momentum equation describes the forces due to gravity, pressure gradients, and shock compressions. The energy equation describes the change in internal energy due to shocks and adiabatic pressure work. The details have been described in previous studies (Monaghan and Lattanzio, 1985; Monaghan, 1992; Canup, 2004). We have tested our SPH code by reproducing the analytical solution for a shock tube and the adiabatic collapse of an initially isothermal gas sphere (Evrard, 1988; Hernquist and Katz, 1989). We use $N = 100,000$ SPH particles, which is similar to modern SPH calculations (e.g., Ćuk and Stewart, 2012; Canup, 2012). We have developed our own SPH code integrated with GRAvity PipE (GRAPE). The GRAPE hardware calculates gravitational interactions 100-1000 times faster than conventional computers at comparable cost (Makino et al., 1995, 1997).

3.2.2 Entropy of the disk

In this work, entropy is used to characterize the thermodynamics of the system. Entropy is relatively well-conserved after the passage of shocks and is insensitive to the resolution. This is because it slowly changes spatially, even when density and temperature change rapidly. A particle with few nearby particles increases its smoothing length and experiences artificial adiabatic expansion and cooling (without its neighboring particles, the density of a particle i is $\rho_i \propto m_i/h_i^3$). This effect can lead to unrealistically a small density and temperature of the particle. Because a particle in the disk does not have sufficient neighboring particles with the present-day resolution ($N \sim 10^5$), it experiences significant adiabatic expansion. This leads to

the unrealistically small density and temperature, while the entropy does not change in the process.

The majority of the entropy gain is due to the impact-induced shocks, which can be modeled by SPH simulations. Additionally, we allow for the small increments in entropy arising from SPH particles that are initially in eccentric or inclined orbits but are incorporated into the disk as material in circular orbit. Entropy gain due to mass redistribution within the disk is also possible, even on a short timescale. This effect is considered for high entropy (high vapor fraction) cases. The detailed ideas and procedures are described in Section 3.2.4 and the Appendix.

3.2.3 Initial conditions

Both the target and impactor consist of 70% mantle (forsterite) and 30% core (iron) by mass. The M-ANEOS equation of state is used (Thompson and Lauson, 1972; Melosh, 2007). This equation can treat phase changes and co-existing multiple phases. Initially, the mantle has a uniform entropy of 3165 J/K/kg, such that temperature at the surface is approximately 2000K. The surface temperature corresponds to that of the "warm starts" of the previous studies (Canup, 2004, 2008b). The constant entropy at depth implies a solid that is close to the melting curve. This is appropriate since the early Earth was formed so quickly that it could not have efficiently cooled in the period since the previous giant impact. The parameters are the impactor-to-total mass ratio γ, the total mass of the target and impactor, $M_{\rm T}$, the scaled impact parameter b ($b = \sin\theta$, here θ is the impact angle), the impact velocity $v_{\rm imp}$, and the

initial spin period, $T_{\rm spin}$.

3.2.4 Derivation of the disk structure

The mass and entropy of the disk is obtained from an SPH simulation. After approximately one day of simulated time, the system has usually evolved to the point where its final state can be estimated from the current distribution of orbital parameters and thermodynamic state. The semi-major axis, eccentricity, and inclination of each particle orbiting around the planet are identified based on the SPH output. A particle whose orbit is not hyperbolic or does not cross the planet is considered to be a part of the disk. The details are described in a previous study (Canup et al., 2001). Additionally, we also detect aggregates of SPH particles and assign a single orbit to them. Assuming the inclination and eccentricity are quickly damped (Thompson and Stevenson, 1988) while the angular momentum is conserved, the corrected semi-major axis of a particle i, $a_{i,\rm final}$, is obtained. The details are described in the Appendix. The entropy of the particle, S_i, is directly obtained from the SPH calculation. Based on m_i and S_i as a function of $a_{i,\rm final}$, the cylindrically averaged surface density of the disk, $\Sigma(r) = dM/2\pi r dr$, and entropy, $S_{\rm SPH}(r)$, are derived. Here, r is the distance from the Earth's spin axis and dM is the mass between the two cylindrical shells.

A problem occurs with this approach when the vapor mass fraction is high. Clearly, SPH particles that will expand mostly to vapor will not follow approximately Keplerian trajectories due to the large pressure gradient forces and possibly instabilities as explained below. The vapor-rich disk is partially supported by the

pressure gradient (dp/dr). When the self gravity of the disk is negligible, the specific angular momentum of the vapor in the z-direction (parallel to the Earth's spin axis), L_z, is written as

$$L_z(r) = \sqrt{GM_{\rm p}r + \frac{r^3}{\rho}\frac{dp}{dr}}, \tag{3.1}$$

where $M_{\rm p}$ is the mass of the planet. In the outer part of the disk, dL_z/dr becomes negative since the term that includes $r^3 dp/\rho dr$ (< 0) starts dominating the $GM_{\rm p}r$ term. These regions do not satisfy the Rayleigh stability criterion ($dL_z/dr > 0$, Chandrasekhar, 1961) and will mix radially on a dynamical timescale (i.e., of order hours). In addition, if $d\Sigma/dr > 0$ at the inner edge of the vapor-rich disk, there will be an radial mass redistribution, and some vapor will migrate inward and merge with the planet due to the pressure gradient forces.

Therefore, it is not possible to determine the surface density in these cases using only the SPH output and the procedure for treating the SPH particles as Keplerian. In principle, a sufficiently high-resolution SPH simulation carried out to longer times could determine the structure. We have chosen instead to estimate the outcome by use of a simple functional form that satisfies the global constraints. We assume that the surface density can be written as $\Sigma(r) = (C_1 + C_2 r)\exp(-C_3 r)$ (C_1, C_2, and C_3 are constants). These constants are obtained by conserving $M_{\rm D}$ and L_D and meeting a stable condition that $d\Sigma/dr = 0$ at the inner edge (This choice of boundary condition is not physically required and other choices could be possible). The resulting disk is more stable and meets the Rayleigh criterion in the broader regions. However, the disk may be still unstable near the outer edge because $L_z(r)$ rapidly decreases at large

r, but this does not cause a major problem because the mass present in the outer region is relatively small.

Next, the two-dimensional structure of the disk is calculated based on the following assumptions: (1) The disk is hydrostatic in the z-direction. (2) A vapor phase exists above a thin liquid layer (if it exists) and no mixed-phase layer exists. (3) The gravity forces of the planet and liquid of the disk are considered. (4) If a liquid layer exists at $z = 0$ at a given r, the pressure is equal to the saturation vapor pressure at any $z > 0$. Otherwise, the pressure gradient follows a dry adiabatic lapse rate until the pressure reaches the saturation vapor pressure. The vapor phase above is also saturated. Whether a liquid layer exists at a given r depends on $\Sigma(r)$ and $S_{\mathrm{SPH}}(r)$. The details are described in Section 3.3.4. The hydrostatic relation can be described as

$$\frac{1}{\rho}\frac{dp}{dz} = -\frac{GM_{\mathrm{p}}z}{(r^2+z^2)^{\frac{3}{2}}} - 2\pi G\Sigma_{\mathrm{l}}(r), \tag{3.2}$$

where p is the pressure, ρ is the density, G is the gravitational constant, M_{p} is the mass of the planet, and $\Sigma_{\mathrm{l}}(r)$ is the surface density of the liquid at a given r.

The thermodynamic properties, such as p, ρ, and the temperature, T, are iteratively calculated in the z-direction by solving Equation (3.2), while satisfying $\Sigma(r)$ and $S_{\mathrm{SPH}}(r)$. Based on an initial guess of $T(r, z = 0)$ at a given r, the entropy averaged in the z-direction $S(r)$ is calculated using the relationship

$$\Sigma(r)S(r) = \int_{-\infty}^{\infty} \rho_{\mathrm{v}}(r,z)S_{\mathrm{v}}(r,z)dz + \Sigma_{\mathrm{l}}(r)S_{\mathrm{l}}(r). \tag{3.3}$$

	γ	$M_{\rm T}$	b	$v_{\rm imp}$	$T_{\rm spin}$	$M_{\rm D}$	$L_{\rm D}$	$S_{\rm ave}$	VMF
(a) Standard	0.13	1.02	0.75	1.0	0	1.35	0.26	4672	19%
(b) Fast-spinning Earth	0.045	1.05	-0.3	20 (km/s)	2.3	2.36	0.44	7132*	96%
(c) Sub-Earths	0.45	1.04	0.55	1.17	0	3.07	0.64	7040*	88%
(d) Intermediate	0.3	1.00	0.6	1.0	0	2.80	0.57	5136	31%

Table 3.1: The initial conditions and outcomes. γ is the impactor-to-total mass ratio, $M_{\rm T}$ is the total mass scaled by the Earth mass, b is the scaled impact parameter, $v_{\rm imp}$ is the impact velocity scaled by the escape velocity (except b), and $T_{\rm spin}$ is the initial spin period of the target (hrs). $M_{\rm D}$ is the disk mass scaled by the Moon mass, and $L_{\rm D}$ is the angular momentum of the disk scaled by the current angular momentum of the Earth and Moon. $S_{\rm ave}$ is the averaged entropy of the disk (J/K/kg). The asterisk indicates that the entropy increase due to mass-redistribution of the disk is considered (discussed in Section 3.2.4 and the Appendix.) VMF is the vapor mass fraction.

Here, $\rho_{\rm v}(r,z)$ and $S_{\rm v}(r,z)$ are the density and entropy of the vapor, $\Sigma_{\rm l}(r)(=\Sigma(r)-\Sigma_{\rm v}(r))$ and $S_{\rm l}(r)$ are the surface density and entropy of the liquid. By comparing $S_{\rm SPH}(r)$ with $S(r)$, the temperature at the interface ($z=0$) is corrected until the relative change of these two values becomes less than 0.1%.

3.3 Results

The initial conditions and outcomes are summarized in Table 3.1. $M_{\rm D}$ is the disk mass normalized by the lunar mass and $L_{\rm D}$ is the disk angular momentum normalized by that of the Earth-Moon system. $S_{\rm ave}$ is the average disk entropy (discussed in Section 3.3.1) and determined by the impact energy and material properties. VMF is the overall vapor mass fraction of the disk. The $S_{\rm ave}$ of the fast-spinning Earth (b) and sub-Earths (c) is much larger than that of standard (a) due to the larger kinetic energy involved in the impact. This high-entropy disk is mainly vapor (discussed in

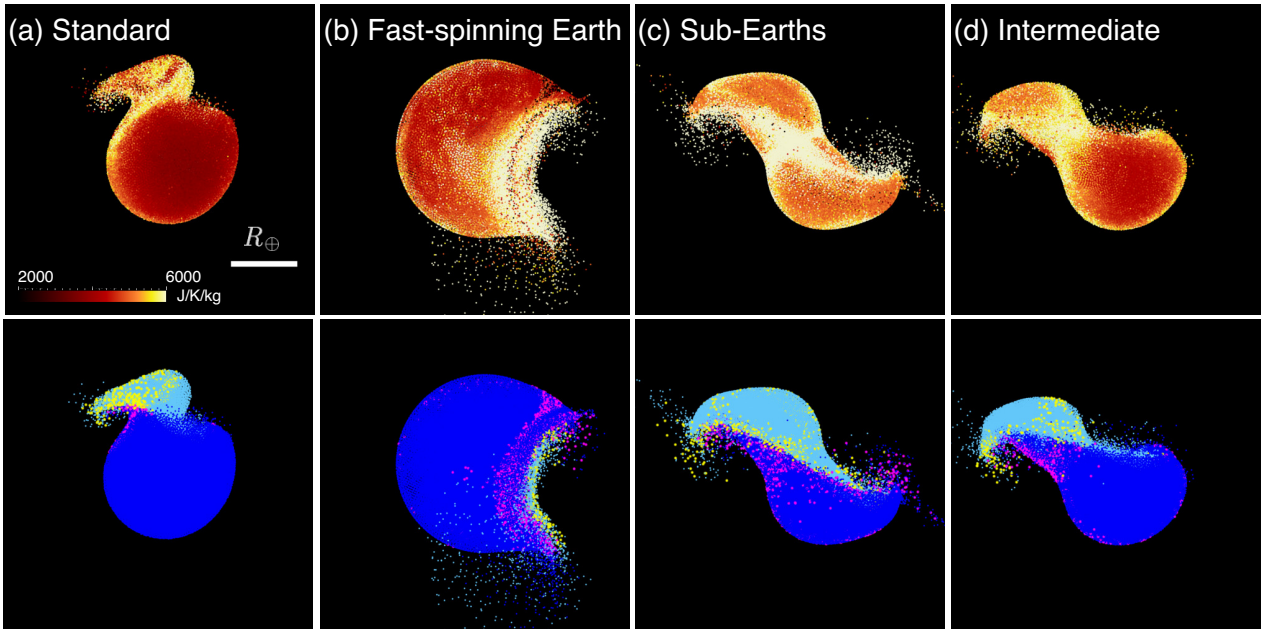

Figure 3.1: Each panel shows a projection of a 3D calculation onto the equatorial plane. In the top panel, color scales with the entropy of forsterite in J/K/kg. In the bottom panel, particles originating from the target are shown in blue and magenta. Particles originally from the impactor are shown in sky blue and yellow. The magenta and yellow particles (their sizes are magnified) become part of the disk.

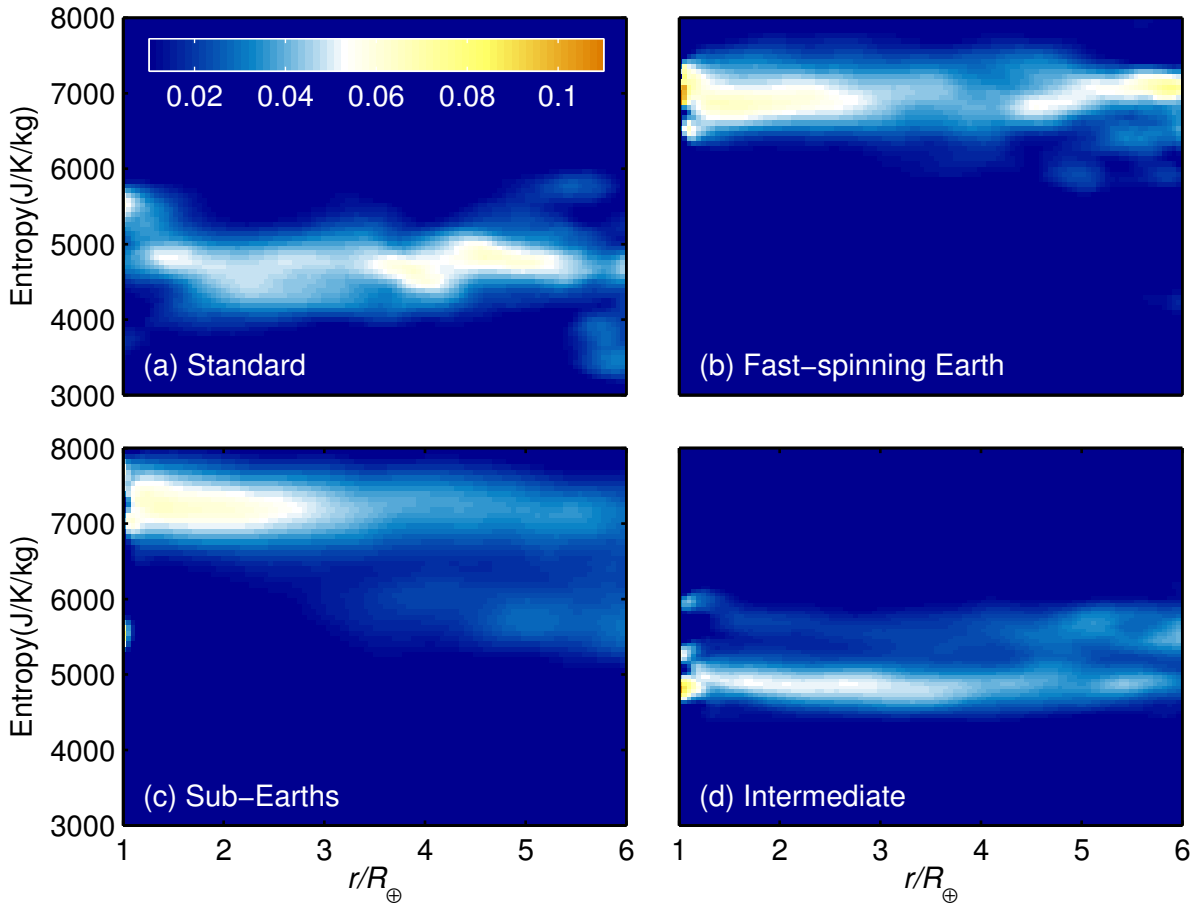

Figure 3.2: A probability distribution of a particle, $\mathrm{P}(r, S)$, where r is a distance from the Earth's spin axis and S is entropy. The probability is normalized at a given r ($\Sigma_k \mathrm{P}(r, S_k) = 1$) and color-coded according to its intensity. $\mathrm{P}(r, S)$ is a weak function of r and the disk is nearly isentropic in all cases.

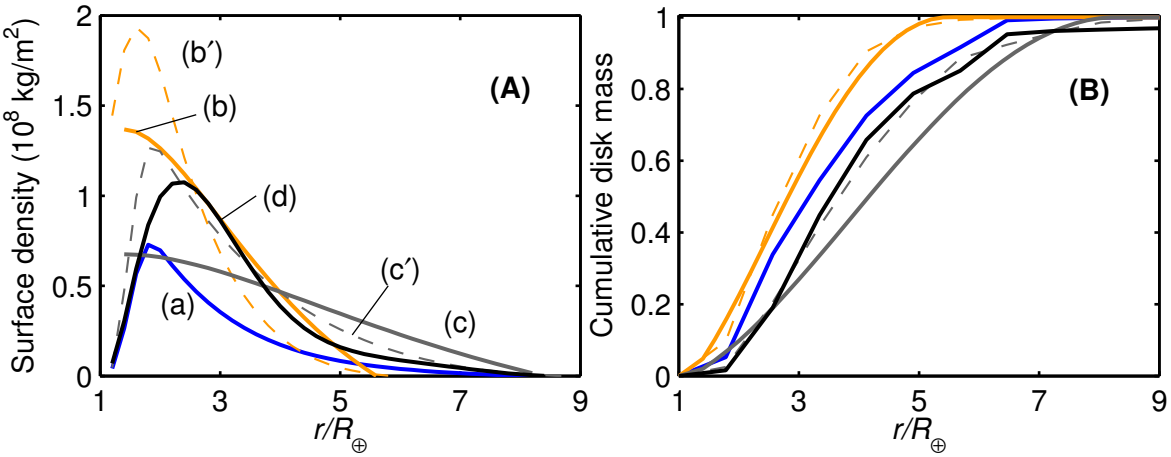

Figure 3.3: The surface density and cumulative mass distribution of the disk. (a) standard: blue, (b) fast-spinning Earth: yellow, (c) sub-Earths: gray, (d) intermediate: black. (A) The SPH calculations produce the surface densities of (a), (b'), (c'), and (d). However, (b') and (c'), indicated by the dashed lines, are unstable because these disks do not satisfy the Rayleigh criterion. The surface densities of more stable disks are shown in (b) and (c). (B) The mass distribution is obtained by integrating the surface density.

Section 3.3.4). The disk in the intermediate (d) is moderately shock-heated. The entropy increase due to the circularization of the particles in the disk is typically less than 10%. The mass redistribution is considered in (b) and (c), which also increases $S_{\rm ave}$ (indicated by the asterisk). The value of this increment depends on the model of the surface density, but it is not significant (less than 5%). The details are discussed in Section 3.2.4 and the Appendix. The disk of the non-standard models is more massive than that of the standard model. After the circulation of the disk, the mass outside of the Roche radius ($\sim 2.9R_\oplus$) is (a) 0.77, (b) 1.12, (c) 2.33, and (d) 1.96 in lunar mass.

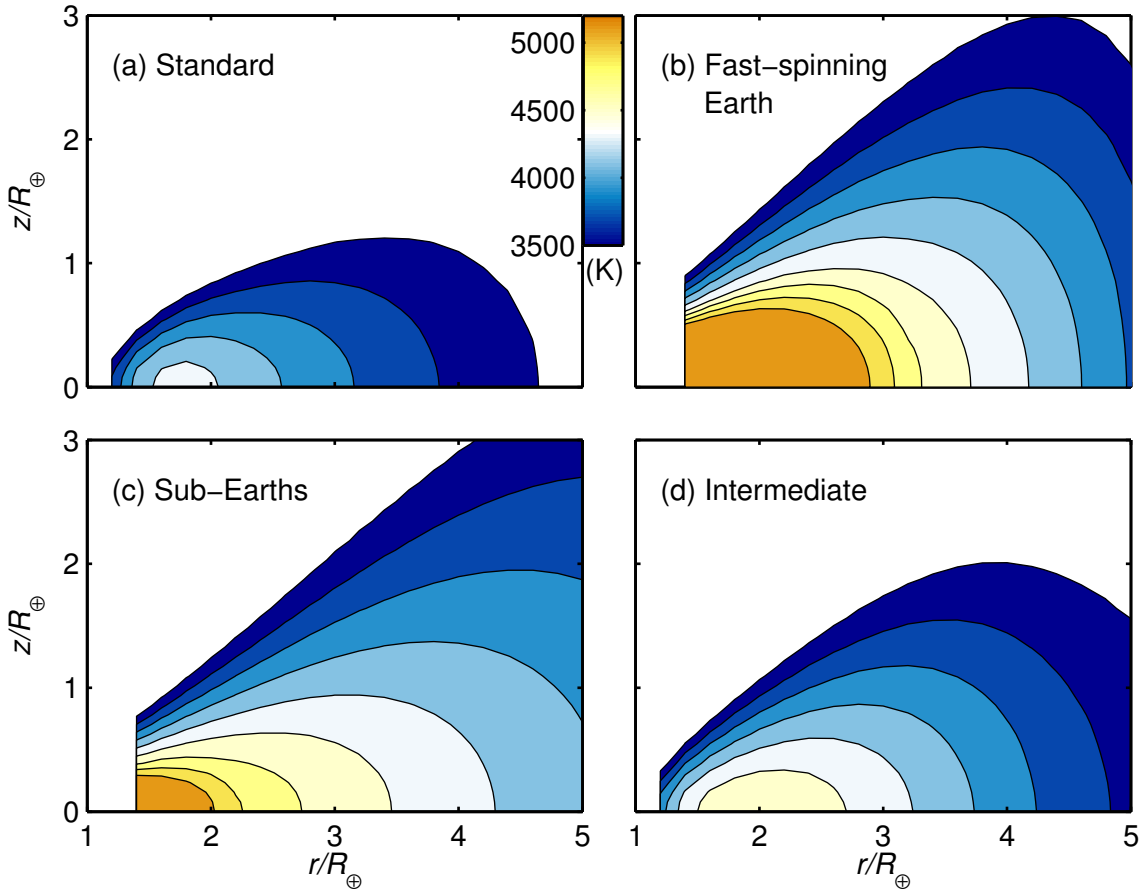

Figure 3.4: Temperature contours of the disk. More energetic impacts lead to higher disk temperatures. In (b) and (c), the inner edge of the disk is located slightly outside of the disk in (a) and (d) because its planetary equatorial radius is larger due to its short spin period.

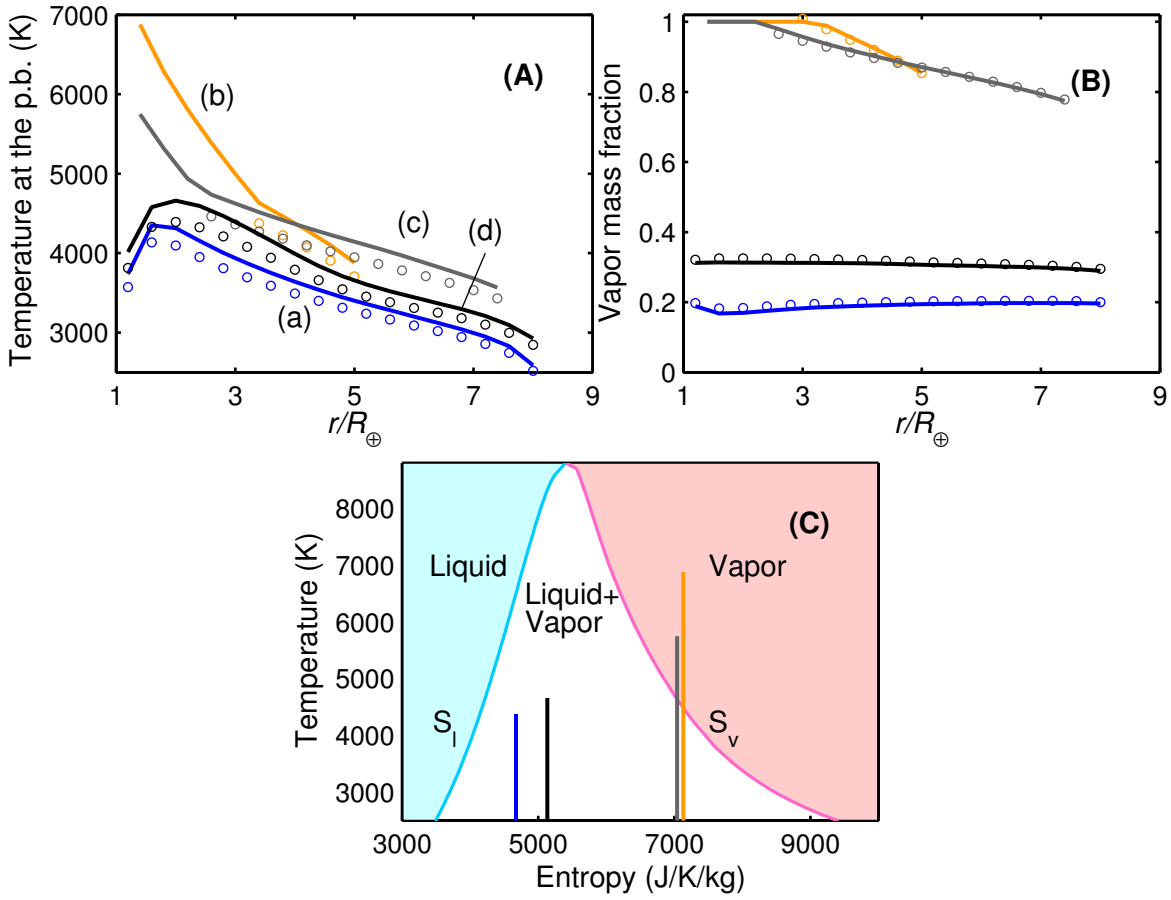

Figure 3.5: (A) and (B) show the comparisons between the numerical result (line) and the simple model (circle) described in Section 3.3.4. The color-coding of the lines is the same as that of Figure 3.3. (A) shows the temperature at the phase boundary (at $z = 0$). The difference of $\sim$200 K between the simulation and model arises because the self-gravity of the disk and vertical variation of the temperature are ignored in the model. The peaks of the surface density and temperature coincide. (B) shows the radial vapor mass fraction. The model matches the numerical result well. (C) is the phase diagram of forsterite (M-ANEOS, Thompson and Lauson, 1972; Melosh, 2007). The sky-blue solid line represents the entropy of liquid and the magenta solid line represents that of the vapor at the phase boundary. The range of $T_{\rm pb}$ for each $S_{\rm ave}$ is indicated by the solid lines.

3.3.1 Isentropic disk

Figure 3.1 shows snapshots of the impact simulations of the four different scenarios. The upper panels show the entropy at the impact and the bottom panels show the origin and fate of the particle. The magenta particles (target-origin) and yellow particles (impactor-origin) become part of the disk. We refer to the particles that eventually form the disk as "disk particles" hereafter. In (a), the impactor is destroyed by the impact and the tides from the planet and then form a disk. Most of the disk particles come from specific parts of the impactor. Since the disk particles have similar distances from the impact point, they gain similar extent of shock-heating and entropy. This leads to a relatively isentropic disk. This feature is clearly shown in Figure 3.2a. This figure shows the probability distribution of a disk particle, $\mathrm{P}(r, S)$, color-coded according to its intensity. The number of the SPH particles is counted at a given $r \pm \Delta r$ and $S \pm \Delta S$ ($\Delta r = 0.02 R_\oplus$ and $\Delta S = 20$ J/K/kg). $\mathrm{P}(r, S)$ is obtained by normalizing the number by the total number of SPH particles at that radius. Note that $\mathrm{P}(r, S)$ is statistically irrelevant in a sparse region (near the outer edge of the disk). Although the entropy of the disk in (a) has a dispersion, it is relatively uniform and a weak function of r.

In (b), a small impactor smashes into the rapidly-rotating oblate planet. The impact is so energetic that a part of the planetary mantle is stripped off. Most of the disk particles are initially located near the surface (shown in magenta in Figure 3.1b). These particles are ejected in the z-direction after the first shock. When they fall back to the $z = 0$ plane, they collide with the particles coming from the other

side. This secondary shock significantly increases the entropy of the disk particles, because the pre-shock density of the second impact is small and the disk materials are compressed easily. Since most of the disk particles follow this evolutionary path, the disk particles are shock-heated to a similar extent (Figure 3.2b). In (c), the two similar-size objects collide with each other several times until they merge into a single planet. The angular momentum of the planet becomes so large that the planet becomes unstable. A portion of the outer mantle is stripped away and forms a disk. The entropy of the disk particles continue to increase through the multiple impacts. This leads to a larger dispersion of disk entropy than the other cases (Figure 3.2c), but the entropy still does not depend on r. (d) is similar to (a), but disk materials are coming from broader regions, including the target. Nevertheless, the disk particles are originally located nearby and experience similar increase of the entropy (Figure 3.2d).

Thus, the entropy is a weak function of r and approximately uniform in all cases. In the following arguments we assume the disk is adiabatic and has a uniform entropy ($S_{\rm SPH}(r) = S_{\rm ave} = \text{const.}$). Note that $S_{\rm SPH}$ includes additional heating due to the circularization of the disk particles (Section 3.2.4 and the Appendix), although the increments are relatively small (typically, less than 10% of $S_{\rm ave}$). For (b) and (c), additional heating is considered due to the mass redistribution in the disk (Section 3.2.4 and the Appendix).

3.3.2 Radial mass distribution

Figure 3.3A shows the surface density of the disk. The blue solid line (a), the yellow dashed line (b'), the gray dashed line (c'), and the gray solid line correspond to the surface densities of the cases (a), (b), (c), and (d) based on the SPH calculations. The disk in (b') and (c') is unstable because the Rayleigh criterion is not satisfied at $r > 3.4R_{\oplus}$ and $r > 4.8R_{\oplus}$ for (b') and (c'), respectively. Even in the stable regions, the slope of $L_{\rm z}$ is shallow, especially for (b'), so that the regions may become easily unstable. Additionally, since $d\Sigma/dr > 0$ at the inner edge of the disk, the mass is redistributed radially.

The surface density of a more stable disk ($\Sigma(r) = (C_1 + C_2 r)\exp(-C_3 r)$) is shown as (b) and (c). This modeled disk is stable in a broader region, but still unstable at $r > 3.8R_{\oplus}$ and $r > 5.4R_{\oplus}$ in (b) and (c). However, the slope of L_z of (b) and (c) is steeper than that of (b') and (c'), so that the disk is more stable. The disk in (a) and (d) does not satisfy the criteria either and hence its structure may be reshaped. But we ignore this change because the disk in (a) and (d) is liquid-dominant and the effect of pressure gradient is less significant.

Figure 3.3B shows the cumulative disk mass. This is obtained by integrating the surface density (Figure 3.3A). The disk in (b) is more compact than in the other cases, because the disk materials originate from the mantle of the target and they gain relatively little angular momentum from the impact. In the other cases, the angular momentum comes from the orbital angular momentum of the massive impactor.

3.3.3 2D structure of the disk

The temperature is derived at a given r and z from the entropy and phase diagram. It is important to stress that entropy is a better parameter to characterize the thermodynamics of the disk, but temperature is of course is important to decide chemical questions such as partitioning and possible isotopic fractionation. The temperature is also relevant to the evaluation of possible hydrodynamic outflow. Figure 3.4 shows the temperature contour of the disks as a function of r and z, normalized by $R_{\oplus}$. The figure is color-coded according to the temperature (3500-5200K). A more energetic impact (with higher values of $S_{\rm ave}$) leads to higher temperatures in the disk.

3.3.4 Simple semi-analytic disk model

The structure of the disk can be described by a simple model. Equation (3.3) can be approximately written as

$$\Sigma(r)S_{\rm ave} \simeq \Sigma_{\rm v}(r)S_{\rm v}(r,0) + \Sigma_{\rm l}(r)S_{\rm l}(r), \tag{3.4}$$

where, $S_{\rm SPH}(r) = S(r) = S_{\rm ave}$ is assumed. $S_{\rm v}(r,0)$ is the entropy at the phase boundary ($z = 0$) at a given r. This approximation is reasonable because the entropy variation in the z-direction is relatively small. Additionally, because the density is largest at $z = 0$, $S_{\rm v}(r,0)$ has the largest contribution to $S(r)$ among $S_{\rm v}(r,z)$. Neglecting the self gravity of the disk and assuming that the temperature variation

in the z-direction is small, $\Sigma_{\rm v}$ is written as

$$\Sigma_{\rm v}(r) = \int_{-\infty}^{\infty} \rho_{\rm v}(r,z)dz \sim \int_{-\infty}^{\infty} \rho_{\rm v}(r,0)e^{-(z/H)^2}dz, \tag{3.5}$$

which becomes

$$\Sigma_{\rm v}(r) \sim \sqrt{\pi}\rho_{\rm v}(r,0)H, \tag{3.6}$$

as previously derived (Thompson and Stevenson, 1988; Ward, 2012). Here, $H = \sqrt{2}c/\Omega$, $c = \sqrt{RT(r,0)/\mu}$, and $\Omega = \sqrt{GM_{\oplus}/r^3}$. μ is the average molecular weight (~ 30 g/mol, Thompson and Stevenson, 1988). Likewise, the pressure distribution is also derived as $p(r,z) \sim p(r,0)\exp\left[-(z/H)^2\right]$.

Equation (3.4) can be written as

$$S_{\rm ave} \sim fS_{\rm v}(r,0) + (1-f)S_{\rm l}(r), \tag{3.7}$$

$$f(r) \equiv \frac{\Sigma_{\rm v}(r)}{\Sigma(r)}, \tag{3.8}$$

where $f(r)$ is the vapor mass fraction at a given radius r.

Note that all parameters on the right hand side of Equation (3.7) depend only on the temperature at the phase boundary, $T_{\rm pb}(r)(= T(r,0))$. Since the liquid and vapor are assumed to be in equilibrium, $\rho_{\rm v}(r,0)$ and hence $\Sigma_v(r)$ are uniquely determined, once $T_{\rm pb}(r)$ is specified. $T_{\rm pb}$ is approximately obtained from Equation (3.7), given

$\Sigma(r)$, $S_{\rm ave}$, and an equation of state. Replacing r by $T_{\rm pb}$ ($r = r(T_{\rm pb})$), f is written as

$$f(T_{\rm pb}(r)) \sim \frac{S_{\rm ave} - S_{\rm l}(T_{\rm pb})}{S_{\rm v}(T_{\rm pb}) - S_{\rm l}(T_{\rm pb})}. \tag{3.9}$$

Figure 3.5 shows the validity of this model. In Figure 3.5A, the $T_{\rm pb}$ calculated numerically by solving Equation (3.2) are indicated by the lines and the model (the approximate $T_{\rm pb}$ by solving Equation (3.7)) is indicated by the circles. A systematic difference ($\sim$ 200K) occurs because the temperature variation in the z-direction and the self-gravity of the disk are ignored here, but the model still captures the behavior. Figure 3.5B shows radial vapor mass fraction. The model matches the calculation very well. While the vapor fraction does not change radially in (a) and (d), it does change in (b) and (c). Additionally, the inner part of the disk in (b) and (c) is completely in the vapor phase. This vapor-only region cannot be modeled since the pressure is not equal to the saturation vapor pressure. Figure 3.5C provides visual interpretations of Equation (3.9). The shaded regions in sky-blue and magenta show the liquid and vapor phases of forsterite. $S_{\rm ave}$ of each disk is represented by the solid line. $f = (S_{\rm ave} - S_{\rm l})/(S_{\rm v} - S_{\rm l})$ does not vary greatly in (a) and (d) as in the other cases. Our model also provides an intuition for the reason that a higher $\Sigma(r)$ tends to give a higher $T_{\rm pb}$ (Figure 3.3A and 3.5A). $\Sigma_{\rm v}(r)$ is basically determined by $T_{\rm pb}$. For a given r and $T_{\rm pb}$, a higher $\Sigma(r)$ results in a smaller $S(r)$, since the contribution of $\Sigma_{\rm l} S_{\rm l}$ becomes larger in Equation (3.4) ($S_{\rm v} \geq S_{\rm l}$). Therefore, given a higher $\Sigma(r)$, $T_{\rm pb}$ increases to obtain the same $S(r)$. Additionally, given $\Sigma(r)$, a smaller r leads to a smaller $\Sigma_{\rm v} (\propto H \propto r^{3/2})$. Thus, to obtain the same $S_{\rm ave}$, $T_{\rm pb}$ needs to be greater at

a smaller r.

The vapor mass fraction in (b) and (c) reaches 100% at the inside of the disk. In this region, both $\Sigma(r)$ and $S_{\rm ave}$ are large. To reach such high $S(r)(= S_{\rm ave})$, $T_{\rm pb}(r)$ needs to be large. However, an upper limit of $T_{\rm pb}(r)$, and hence $S(r)$, exists to satisfy $\Sigma_{\rm v}(r) \leq \Sigma(r)$. Let these limits called be $T_{\rm pb(max)}(r)$ and $S_{\rm max}(r)$. $dT_{\rm pb(max)}(r)/d\Sigma(r) > 0$ because a larger $\Sigma(r)$ allows a larger $T_{\rm pb}$. Near this limit, f is close to unity and $S(r)$ should be close to $S_{\rm v}(r)$. Since $dS_{\rm v}(T)/dT < 0$ according to the phase curves of forsterite (Figure 3.5C), $dS_{\rm v}(r)/d\Sigma(r) \sim dS_{\rm max}(r)/d\Sigma(r) < 0$. Therefore, a given $S_{\rm ave}$ may not be satisfied if $\Sigma(r)$ is too large in the region. In such a region, the assumption that the system is in vapor-liquid equilibrium is no longer valid. The part of the disk is completely in the vapor phase. This is the case for the inner region of (b) and (c). Once $T_{\rm pb}(r)$ is determined, $\rho(r,z)$ and $p(r,z)$ are approximately obtained, as discussed ($\rho(r,z) \sim \rho(r,0)\exp\left[-(z/H)^2\right]$, $p(r,z) \sim p(r,0)\exp\left[-(z/H)^2\right]$). Although this model is very simple, it is useful in that the thermal structure of the disk can be semi-analytically approximated based on just two parameters $S_{\rm ave}$ and $\Sigma(r)$.

3.4 Discussion

3.4.1 Structure of the disk

In (b) and (c), the modeled surface density is not uniquely determined by the SPH output (Section 3.2.4), but this is only a problem in the high vapor fraction cases.

A different model of the surface density will provide different $S_{\rm ave}$ according to the potential energy differences, ΔU, of the disks (Appendix). The increment of $S_{\rm ave}$ due to ΔU is typically a few percent. Therefore, although the disk model is not unique, our model still describes the general disk structure.

Here, we only consider one giant impact simulation for each model. However, the surface density and entropy of the disk can vary even in the same type of the giant impact model. Previous statistical studies show that disk mass and angular momentum vary, depending on the choices of initial conditions. This is the case especially for grazing impacts (e.g., Canup, 2004). Therefore, the initial conditions affect the structure of the disk (personal communications with Kaveh Pahlevan).

Note that the atmosphere of the planet has not been considered. Because the SPH method does not adequately describe the physics at the interfaces of large density differences, it cannot very well describe the planet-atmosphere or core-mantle (iron-forsterite) boundaries. This limitation arises because the density of an SPH particle i is determined by its neighboring particles. If the neighboring particles have much larger or smaller densities than that of the expected density of the particle i, it leads to an artificially large or small density of the particle. At the end of an SPH simulation, the outer part of the planet is inflated and has an atmosphere-like structure. But the mass and size of the atmosphere may include large errors. For simplicity we exclude the effect of this "atmosphere" and merely consider it part of the planet.

3.4.2 Stability of a vapor-rich disk

It has been suggested that a vapor-rich disk is not suitable for the Moon formation. Wada et al. (2006) perform two grid-based hydrodynamic simulations of a standard-type giant impact. They use two different polytrope-type equations of state (EOS) and compare the outcomes. One of the EOSs mimics a "gas-like" material and the other represents a liquid (or solid) material. They find out a giant impact with the gas-like EOS leads to a dynamically unstable disk. The density contrasts within the disk are so large that several shocks propagate through the disk. The disk loses its angular momentum by the process and a significant disk mass falls onto the planet. On the other hand, if the disk is mostly liquid (i.e., with the liquid-like EOS), the density contrast within the disk is small, so that such strong shocks are not created. They conclude that a vapor-rich disk loses its significant mass so quickly that it is not suitable for the Moon formation. This is an interesting outcome, but it is unclear in their result exactly how the angular momentum budget is satisfied (since material falling back onto Earth is necessarily balanced by material that gains angular momentum). Additionally, it is uncertain whether this is applicable to the stability of the vaporous disk in (b) and (c). The polytrope-type EOSs cannot describe the behavior of the realistic mantle materials very well, such as the phase changes. Therefore, the density structure of the disk may not be very physical. In addition, the proposed EOS may not provide realistic estimates of the Mach numbers of the shocks either. This may provide a large uncertainty in estimating the loss of the angular momentum and mass of the disk due to the shock passage. In order to understand the stability of

the disk, a more realistic EOS needs to be implemented with such a grid-based code.

3.4.3 Evolution of the disk

The Moon-forming disks of the fast-spinning Earth (b) and sub-Earths (c) have much higher entropy and vapor mass fractions than those of the standard model (a). The evolution of such a highly shock-heated disk would likely follow a different path from the canonical scenario. The extent of vaporization may affect the chemical and isotopic signature of the disk and the resulting Moon (Pahlevan, 2013). Additionally, the mass of the Moon might become an important constraint. It takes a longer time to radiatively cool this high-entropy disk. If the disk experiences viscous spreading during the cooling process, it may lose its mass to the planet even before condensation to allow Moon formation. In addition, because the gas is orbiting more slowly than the liquid, the gas removes the angular momentum of the liquid. Thus, the liquid droplets fall to the planet while the gas moves outward, leading to the additional mass loss of the disk. However, the effect may not prevent a Moon formation, because the disk of (b) and (c) is more massive than (a). In any event, further study is required for a more quantitative argument.

Our study also shows that the vapor fraction of the disk can radially vary in (b) and (c), which may cause some chemical and isotopic heterogeneity in the disk. If the Moon (or at least its surface) preferentially formed from a particular location of the disk (Salmon and Canup, 2012), the Moon's chemical and isotopic signatures might not represent the entire disk, but rather a specific region of the disk. However, this

conclusion depends on the efficiency of the radial mixing.

3.4.4 Effects of the equation of state

The forsterite M-ANEOS has several non-negligible caveats. Recent experimental studies indicate that M-ANEOS underestimates the shock-induced entropy gain of silicates (Kurosawa et al., 2012; Kraus et al., 2012). Kurosawa et al. (2012) suggest that this effect becomes prominent when the peak pressure, $P_{\rm peak}$, is higher than 330 GPa. Although this may lead to the higher entropy and vapor-mass fraction of the disk, the increments may be relatively limited. This is because majority of the disk particles have smaller peak pressures than this. The fraction of disk particles with $P_{\rm peak} > 330$ GPa is (a) 0 %, (b) 30 %, (c) 6.5 %, and (d) 0 %. However, the entropy gain by an impact cannot be determined simply from this criterion, because these experiments have significantly different initial conditions from those of the giant impact. An impact simulation needs to be performed with a new EOS that includes these experimental results.

In addition, the real mantle material is not pure forsterite. Rather, perovskite is the dominant phase in the lower mantle (P >24 GPa). Since perovskite is less compressible than forsterite (e.g., Jackson and Ahrens 1979; Deng et al. 2008, Sarah Stewart, personal communications), material initially in the perovskite phase may be less shock-heated by an impact than our pure forsterite mantle. However, we conclude that this has a minor effect on the outcome, at least for the thermodynamics of the particles that end up in the disk. First, the larger part of the disk particles was

originally in the upper mantle. The fractions of the disk particles that are from the upper-mantle are (a) standard 79%, (b) fast-spinning Earth 60%, (c) sub-Earths 68%, (d) intermediate 42%. Additionally, most of the disk particles suffer additional shocks in which the pre-shock pressure is much lower than 24 GPa. These multiple shocks efficiently increase the entropy of the disk particles and erase the memory of the initial condition. Therefore, the choice of the phase in the mantle is not likely to affect the entropy estimate significantly. We are separately considering the difficult question of the outcome of these events for the deep Earth.

3.5 Conclusions

This is the first work that bridges a hydrodynamic giant impact simulation and the resulting hydrostatic disk. We perform various SPH simulations in order to identify the properties of the disk, including its mass, angular momentum and entropy distribution. Using these values as constraints, the two dimensional structure of the disk is derived. Four distinctive scenarios are investigated: (a) standard, (b) fast-spinning Earth, (c) sub-Earths, and (d) intermediate. In all cases, the disk is approximately isentropic. In (a) and (d), the temperature of the disk is up to 4500-5000K and the overall vapor mass fraction of the disk is 20-30%. These results are consistent with previous studies on the disk. On the other hand, the recently suggested models, such as (b) and (c), create a high-entropy and more vaporized disk. The temperature is as high as 6000-7000K and the vapor mass fraction is higher than 80%. Such a high-entropy disk might lead to a chemically and isotopically different Moon from

that of the canonical model. We also develop semi-analytic solutions for the thermal structure of the disk, including the radial temperature distribution on the mid-plane and the radial vapor mass fraction. This model only requires the radial surface density and the average entropy of the disk as inputs. This may be used as an initial condition for further study on the Moon-forming disk.

Appendix

Two additional processes that heat up the disk, besides the impact-induced shock heating, are considered here. As described in Section 3.2.4, we assume that an initially eccentric and inclined disk particle is circularized. Since this lowers the orbital energy of the particle, the excess of the energy is emitted as heat and heats up the disk. Assuming the component of angular momentum which is parallel to the Earth's spin axis is conserved, the resulting semi-major axis is $a_{i,\mathrm{final}} = a_i(1 - e_i^2)\cos^2 I_i$. a_i is the initial semi-major axis before the damping, e_i is the eccentricity, and I_i is the inclination. Additional heating ΔE_i due to the circularization can be expressed as

$$\Delta E_i = \frac{GM_\oplus m_i}{2a_i}\left(1 - \frac{1}{(1 - e_i^2)\cos^2 I_i}\right). \tag{3.10}$$

The entropy increase by this process $\Delta S_{i,\mathrm{circular}}$ is $\sim \Delta E_i/T_i$, where T_i is the temperature of the particle. In addition to this, in the vapor-rich cases, the disk is heated due to a mass redistribution within the disk, as described in Section 3.2.4. Similarly, let ΔU equal the difference of the potential energies of the disks before and after the

redistribution. The additional entropy is approximately written as $\Delta S \sim \Delta U/T_{\rm ave}$, where $T_{\rm ave}$ is the average temperature of the disk. The increments of $S_{\rm ave}$ by these post-impact processes depend on the initial conditions of the impact. In our calculations, each process increases the entropy by less than 10 percent.

Chapter 4

Volatile loss from the Moon-forming disk

4.1 Introduction

It is widely accepted that the Earth's Moon formed by a collision between the proto-Earth and an impactor around 4.5 billion years ago (Hartmann and Davis, 1975; Cameron and Ward, 1976). This impact created a partially vaporized disk around the planet, from which the Moon accreted. In the standard version of this hypothesis, the impactor was approximately Mars-size and the impact velocity was close to the escape velocity (Canup and Asphaug, 2001). This model has been favored because it can explain several observed aspects of the Earth-Moon system, but it cannot easily explain the fact that the Earth and Moon have identical isotopic ratios (e.g., oxygen, silicon, tungsten, chromium, and titanium, Wiechert et al. 2001; Herwartz et al. 2014; Armytage et al. 2012; Touboul et al. 2007; Zhang et al. 2012; Lugmair and Shukolykov 1988). This is because numerical simulations of the giant impact show that most of the disk materials mainly originate from the impactor, which presumably had different isotopic ratios from the Earth. For example, the oxygen isotopic ratios between the Earth and Mars differ by 0.32‰ (Franchi et al., 1999). It may be possible that the impactor happened to have similar isotopic ratios of a specific element to those of Earth, such as oxygen (Kaib and Cowan, 2015; Mastrobuono-Battisti et al., 2015), but it is still not very likely that the impactor has all the observed isotopic ratios identical to those of Earth.

To overcome this problem, several new impact models have been suggested. Ćuk and Stewart (2012) suggest that a small impactor hit a rapidly rotating Earth while Canup (2012) suggests that two half Earth-size object collided. In these models,

the composition of the disk is similar to that of the Earth, and therefore the isotopic similarities could be naturally explained. Since the giant impacts in the recent models are more energetic than that of the standard model, the recent models predict hotter and more vaporized Moon-forming disks (up to 6000-7000K) and its vapor mass fraction ($80 - 90$ %) with respect to the standard model (up to 4000-5000K, 20-30 %) (Nakajima and Stevenson, 2014). These new models are promising in terms of explaining the isotopic similarities, but they may contradict Earth's mantle chemistry that suggests that the Earth's mantle was not mixed by the impact (Nakajima and Stevenson, 2015).

In addition to the similar isotopic ratios, the giant impact may have also left its signature on the lunar geochemistry. The giant impact has been thought to be at least partly responsible for the fact that the Moon is depleted in volatiles because the giant impact was so energetic that some volatiles may have escaped from the Moon-forming disk. A number of geochemical studies show that the Moon is depleted in volatiles (e.g. K, Rb, Na and other volatile elements, Krähenbühl et al. 1973a,b; Tera and Wasserburg 1976; Ringwood and Kesson 1977; Taylor 1979; Wolf and Anders 1980). In addition, gamma ray spectroscopy data from Lunar Prospector confirmed that the lunar K/Th ratio ($\sim$360) is much smaller than that of the Earth ($\sim$5500) (K is much more volatile than Th) (Prettyman et al., 2006). Likewise, the Moon's K/U ratio, which is smaller than that of the Earth, also indicates volatile loss (Tera et al., 1974).

In a similar manner, the Moon may have lost its water during its accretion. Indeed,

initial analyses of lunar rock samples from Apollo missions appeared to suggest that the Moon is devoid of indigenous water (Epstein and Taylor, 1974). However, more recent studies with improved analytical techniques indicate that the Moon is more water-rich than previously thought. A number of studies have been conducted to measure water abundance in lunar apatites (Boyce et al., 2010; McCubbin et al., 2010; Greenwood et al., 2011; Barnes et al., 2013; Tartése et al., 2013), lunar volcanic glasses (Saal et al., 2008, 2013), olivine-hosted melt inclusions (Hauri et al., 2011), and in plagioclase grains in lunar anorthosites (Hui et al., 2013). The water abundances of the source regions of these crystals would reach a couple of hundreds ppm. Based on these studies as well as models of the evolution of the lunar interior, the bulk water content of the Moon has been estimated ranging from < 10 ppm (Elkins-Tanton and Grove, 2011) to ~ 300 ppm (Hui et al., 2013; Hauri et al., 2011, 2015).

Additionally, the lunar D/H contains important information. If a significant amount of water escaped from the disk, the lunar D/H ratio should be more enhanced than that of the Earth because hydrogen H is lighter and would have escaped more easily than the deuterium D. However, analyses of pristine lunar water suggests that the lunar D/H ratio could be comparable to the Earth's ratio, which indicates water loss was insignificant (Saal et al., 2013; Füri et al., 2014). It should be noted that measuring the bulk content of indigenous water and D/H ratio as well as estimating the water content of the bulk Moon are very challenging problems. First of all, later processes, such as degassing from melt, solar wind irradiation, and cosmic-ray spallation, would likely alter the water content and D/H ratio of the melt and

lunar crystals, therefore such processes need to be corrected or find pristine crystals that did not experience such post processes. Furthermore, the evolution of melt must be considered. For example, a water-rich apatite crystal could have been produced after $\sim$ 95 % crystallization of anhydrous minerals (Boyce et al., 2010). This gives another complication to model the indigenous lunar water content. It would be beneficial to combine other elements to untangle these problems. Recent measurements of carbon content of the lunar volcanic glasses support a volatile-rich Moon (Wetzel et al., 2015) while other work using Cl and F in addition to H in apatite suggest that actually the water content of the Moon can be much lower (Boyce et al., 2014, 2015). The distribution of water in the Moon could be heterogeneous (Robinson and Taylor, 2014).

To summarize the geochemical studies, the Moon lost its volatiles with respect to the Earth, but at least the Moon did not lose all the original water by the impact process itself. However, it is not clear whether and how the Moon lost its volatiles during its accretion. One of the suggested processes is that volatiles were lost from the Moon-forming disk by hydrodynamic escape (Abe et al., 2000; Genda and Abe, 2003; Desch and Taylor, 2013). Hydrodynamic escape is a thermal atmospheric escape process that can lead to the escape of heavy atoms or molecules in the atmosphere through collisions with lighter elements. This theory was originally developed for explaining the solar wind dynamics (e.g., Parker, 1963).

This is thought to have occurred in the early terrestrial atmospheres, which were rich in hydrogen (Hunten, 1973; Hunten et al., 1987; Zahnle et al., 1990). Desch and

Taylor (2013) suggest that hydrodynamic escape could have occurred and blowed off the disk atmosphere when the condition $\lambda \equiv GM_{\oplus}\bar{m}/2kT$ is smaller than ~ 2 based on the hydrodynamic escape model developed for solar wind (Parker, 1963). Here, G is the gravitational constant, $M_{\oplus}$ is the Earth mass, $\bar{m}$ is the mean molecular weight, k is the Boltzmann constant, and T is the temperature. They suggest that when $T = 2000$ K, this condition could have been met given that the disk is dominated by dissociated water, which gives $\bar{m} = 6$ g/mol. This is an interesting idea, but an important issue here is that the condition has been developed for the solar wind, which is primarily hydrogen. Thus, if the disk was dominated by heavier elements, this model may not be applicable. If the disk was dominated by heavier elements that were gravitationally bound (i.e., its escape flux was negligible) as discussed in Section 4.3.3, for the hydrogen to escape, it had to first diffuse from this heavy-element rich atmosphere. In this case, the escape rate was limited by the hydrogen diffusion process from the ambient atmosphere. This was likely the case for hydrogen escape from early planetary atmosphere (Hunten, 1973; Hunten et al., 1987; Zahnle et al., 1990) and this type of escape is called "diffusion-limited" hydrodynamic escape. This is a much slower process than the "atmospheric blow off" hydrodynamic escape. Therefore, if this model is applicable to the escape process from the Moon-forming disk, it is not at all clear if volatiles or water could have escaped from the disk.

In this paper, we examine the amounts of water and volatiles (potassium, sodium, and carbon) escape from the Moon-forming disk. We argue that the escape would have been the diffusion-limited hydrodynamic escape and that the amount of the volatile

lost to space was negligible. We first determine the thermal structure of the disk and the existing elements assuming that the disk is in thermal equilibrium. Therefore, in order to explain the volatile loss, hydrodynamic escape is not the most efficient mechanism to remove volatiles from the disk. Therefore, to explain the volatile loss from the disk, another process may be required. For example, volatiles may have lost to the Earth (Canup et al., 2015). It is also possible that some elements escaped from the system by degassing from the lunar magma ocean (Elkins-Tanton and Grove, 2011).

4.2 Model

Here we assume that the disk has a liquid layer on the mid-plane that is sandwiched by a vapor layer (this picture is the same as Figure 3 in Pahlevan and Stevenson 2007). The vertical direction z is defined to be parallel to the Earth's spin axis and the horizontal direction r is perpendicular to the spin axis. No dynamical motion of the disk is considered. First, we calculate the vertical structure of a Moon-forming disk. Subsequently, based on the properties of an upper part (low pressure) of the disk, the escape fluxes of hydrogen and other volatiles are estimated. We assume that the composition of the disk is silicate liquid (SiO_2) and water (Section 5.3). Another disk compositions (Mg_2SiO_4 and water) are considered in Section 5.4. The Moon-forming disk is horizontally extended to a couple of Earth radii ($r = 5 - 7R_\oplus$, Canup et al. 2013; Nakajima and Stevenson 2014). Nevertheless, instead modeling the whole horizontal structure, we identify the vertical structure of the disk at a certain

radial location ($r = 4R_{\oplus}$). This is primarily because the escape is not sensitive to the specific radial location of the disk. The surface density of the part of the disk is assumed to be 7×10^5 kg/m^2, which is based on previous work (Nakajima and Stevenson, 2014). The parameters are the temperature at the liquid-vapor interface and the bulk water content of the disk.

4.2.1 Boundary condition at the liquid-vapor interface

At the liquid-vapor interface (the mid-plane) of the disk, the partial pressure of water is given as (Abe and Matsui, 1986)

$$p_{\mathrm{H_2O}} = \left(\frac{y_{\mathrm{H_2O}}(\%)}{2.08 \times 10^{-4}} \right)^{\frac{1}{0.54}}, \tag{4.1}$$

where y_{H2O} is the mass fraction of water in the liquid. The saturation vapor pressure of pure SiO_2 liquid (2000-6000K) is written as (the units are modified from Visscher and Fegley 2013)

$$p^*_{\mathrm{SiO_2}} = p_0 \exp(-L/RT), \tag{4.2}$$

where $p_0 = 1.596 \times 10^{13}$ Pa, $L = 4.95 \times 10^5$ J/mol, and R is the gas constant. The total pressure at the interface becomes $p = (1 - x_{\mathrm{H_2O}}) p^*_{\mathrm{SiO_2}} + p_{\mathrm{H_2O}}$, where $x_{\mathrm{H_2O}}$ is the mole fraction of water in the liquid ($x_{\mathrm{H_2O}} = \frac{y_{\mathrm{H_2O}}}{18} (\frac{y_{\mathrm{H_2O}}}{18} + \frac{1 - y_{\mathrm{H_2O}}}{60})^{-1}$).

4.2.2 Vertical structure of the disk

We assume that the disk is in the thermal equilibrium as well as in the radiative-convective equilibrium, which indicates that the lower part of the disk (under higher pressure) is convective and the upper part (under smaller pressure) is radiative. It is a new aspect of study in the sense that such a convective region has not been explicitly considered Thompson and Stevenson 1988; Genda and Abe 2003; Ward 2012). The disk is in the hydrostatic equilibrium, i.e., $dp/dz = -\rho g$ where p is the pressure, ρ is the density, and g is the gravity, $g = GM_{\oplus}z/(r^2+z^2)^{\frac{3}{2}}$, where G is the gravitational constant.

In the convective region, the part of the disk is adiabatic. Here, two types of adiabatic structures, moist pseudoadiabat and dry-adiabat, are considered. In the moist pseudoadiabat, the partial pressure of silicate vapor is equal to the saturation vapor pressure (silicate liquid would rain out in the convective region). Water condensation is negligible because of the high temperature of the disk. The lapse rate of the moist pseudoadiabatic is described as (Nakajima et al., 1992),

$$\left(\frac{\partial T}{\partial p}\right)_{\rm mps} = \frac{\frac{RT}{pC_{p,w}} + \frac{x_s^*}{x_w}\frac{L}{pC_{p,w}}}{x_w + x_s^*\frac{C_{p,s}}{C_{p,w}} + \frac{x_s^*}{x_n^*}\frac{L^2}{RT^2C_{p,w}}}, \tag{4.3}$$

where x_s^* is the mole fraction of saturated silicate ($= p^*(T)/p$), x_w is the mole fraction of water, $C_{p,w}$ is the specific heat of water, $C_{p,s}$ is the specific heat of silicate, and L is the latent heat of silicate. Here, $C_{p,w} = 55.7$ J/K/mol, $C_{p,s} = 62$ J/K/mol (values at 1 bar at 3000K, Chase et al. 1985).

Now we consider radiative transport in the disk. The optical depth throughout the disk is described as (Nakajima et al., 1992)

$$d\tau = (\kappa_s x_s m_s + \kappa_w x_w m_w)\frac{dp}{\overline{m}g}, \tag{4.4}$$

where τ is the optical depth, κ is the absorption coefficient, m is the molecular weight, and $\overline{m}$ is the averaged molecular weight. Here, $\kappa_s = 0.1$ m^{2}kg^{-1} (Thompson and Stevenson, 1988) and $\kappa_w = 0.01$ m^{2}kg^{-1} are used (Nakajima et al., 1992). The upward radiation flux at given τ is written as

$$\begin{aligned} F_{\uparrow}(\tau) = \frac{3}{2}\int_{\tau}^{\tau_s} \pi B(\tau') \exp\left[-\frac{3}{2}(\tau' - \tau)\right] d\tau' \\ + \pi B(\tau_s) \exp\left[\frac{3}{2}(\tau - \tau_s)\right], \end{aligned} \tag{4.5}$$

where τ_s is the optical depth at the liquid-vapor boundary. Likewise, the downward radiation flux is written as

$$F_{\downarrow}(\tau) = \frac{3}{2}\int_{0}^{\tau} \pi B(\tau') \exp\left[-\frac{3}{2}(\tau' - \tau)\right] d\tau'. \tag{4.6}$$

The net upward flux is written as $F(\tau) = F_{\uparrow}(\tau) - F_{\downarrow}(\tau)$. Here $\pi B = \sigma T^4$ where σ is the Stefan-Boltzmann coefficient. In the radiative part of the disk, the temperature profile follows

$$\pi B = \sigma T^4(\tau) = \frac{1}{2} F_{\uparrow \mathrm{top}}(\frac{3}{2}\tau + 1), \tag{4.7}$$

where $F_{\uparrow \mathrm{top}}$ is the radiation flux from the top of the atmosphere (where $\tau = 0$). The

transition between the convective lower disk and radiative upper disk is determined iteratively. First, we compute the vertical structure of the convective region and guess the location of the troposphere. This provides τ and T at the troposphere, which gives the value of $F_{\uparrow \mathrm{top}}$ (Equation 4.7). Then, using Equations 4.5 and 4.6, $F_{\uparrow \mathrm{top}} = F_{\uparrow}(\tau = 0)$ is calculated. We repeat this process until the initial guess and the compute value of $F_{\uparrow \mathrm{top}}$ converge.

4.2.3 Dissociation of molecules

At the upper part of the atmosphere, the molecules in the disk are under high temperature and low pressure and therefore they break down to smaller molecules and atoms. Given that the system is in thermal equilibrium, as an example, dissociation of $\mathrm{SiO_2} = \mathrm{SiO} + \frac{1}{2}\mathrm{O_2}$ (v) is described as

$$K_{\mathrm{th}} = \frac{p_{\mathrm{SiO}} p_{\mathrm{O_2}}^{\frac{1}{2}}}{p_{\mathrm{SiO_2}}} = \exp(-\Delta G^0/RT), \tag{4.8}$$

where K_{th} is the equilibrium constant and G^o is the Gibbs free energy at the standard condition ($\Delta G^0 = \Delta H^0 - T\Delta S^0$). Here, ΔH^0 is the change in the Helmholtz energy and ΔS^0 is the change in the entropy. We assume that ΔH^0 and ΔS^0 are not sensitive to temperature and pressure. The rest of reactions and the thermal constants are listed in Table 4.1.

Reaction	ΔS^o (J/mol K)	ΔH^o (kJ/mol)
$SiO_2 = SiO + \frac{1}{2}O_2$	85.2	205
$SiO = Si + \frac{1}{2}O_2$	85.1	550
$MgO = Mg + \frac{1}{2}O_2$	38.0	88
$O_2 = 2O$	117	498
$H_2O = H_2 + \frac{1}{2}O_2$	44.4	242
$H_2 = 2H$	98.8	436

Table 4.1: Reactions and thermodynamic constants (Chase et al., 1985). All the elements are in the vapor phase.

4.2.4 Diffusion-limited flux

The escape flux of hydrogen is determined by the thermal profile of the disk. At lower parts of the disk (small z), eddy diffusion is more efficient than molecular diffusion, and therefore the disk is homogenized. In other words, $K > D$ in this region where K is the eddy diffusivity and D is the molecular diffusivity. On the other hand, at upper parts of the disk, molecular diffusion becomes more dominant ($K < D$), and therefore each molecule or atom has its own scale height (i.e., light elements are more abundance in the region). The transition point ($K = D$) is called homopause.

Once an hydrogen atom (or any light element) goes above the homopause, the atom can easily escapes from the disk. However, this escape rate cannot exceed the hydrogen supply below the homopause. In other words, this supply rate is determined by how fast a hydrogen atom can diffuse from heavy-element rich disk. Therefore, this type of hydrodynamic escape is called diffusion-limited.

Values of K for planetary atmospheres are typically $10^6 - 10^{10}$ cm^2 s^{-1} (or 10^2 - 10^6 m^2 s^{-1}) (Atreya, 1986; Moses et al., 2000; de Pater and Lissauer, 2010). The molecular diffusion coefficient is described as $D = b/N$, where b is the binary collision parameter and N is the number density. b is often expressed as the form AT^s, where

A and s are constants, which are obtained experimentally. If there is no experimental data, with the hard-sphere approximation b is described as follows (Chamberlain and Hunten, 1987),

$$b = \frac{3}{64Q}[2\pi kT(m_1 + m_2)/m_1 m_2]^{1/2}, \tag{4.9}$$

where

$$Q = (\pi/16)(\sigma_1 + \sigma_2)^2, \tag{4.10}$$

where σ_1 and σ_2 are the collision diameters of the two atoms or molecules and m_1 and m_2 are their masses. The upper limit of the escape flux of a light element 1 (this subscript corresponds to hydrogen), ϕ_1 is approximately described as (Hunten, 1973)

$$\phi_1 \leq \phi_l \sim b_i f_1 / H, \tag{4.11}$$

where H is the scale height of the disk and f_1 is the mixing ratio of hydrogen and ϕ_l is the escape flux in the diffusion-limited regime.

4.3 Results

The parameters are the bulk water content (1000 ppm and 100 ppm) and the temperature at the mid-plane $T_{\rm mid}$ (2500, 3000, and 4500 K). Dissociation of SiO_2 and H_2O are shown in this section.

4.3.1 Thermal structure of the disk

The vertical structure of the disk is shown in Figure 4.1 and Figure 4.2. The location of homopause is shown by the shade (discussed in Section 4.3.2). Lower parts of the disk (under higher pressures) are in the convection regime and higher parts of the disk (under lower pressures) are in the radiative regime. The location of the transition is shown by the kink in the the temperature profile (at $p \sim 10$ Pa at $T_{\rm mid} = 2500$ K with 1000ppm water and at $p \sim 10^{-3}$ Pa in the other cases).

When the mid-plane temperature is large (> 3000 K) and when the water fraction of the disk is small (100 ppm and $T_{\rm mid}$=2500K), the disk is dominated by silicate vapor. This is because the partial pressure of the silicate vapor is much larger than that of water. In these cases, the pressure becomes very close to the saturation vapor pressure of SiO_2 and the water mixing ratio is small (~ 0.1 or smaller). In contrast, at $T_{\rm mid} = 2500$ K with 1000 ppm of water, the disk becomes dominated by water (nearly 100% water) since the partial pressure of water becomes larger than that of SiO_2 (Figure 4.1). The pressure becomes lower than the silicate saturation vapor pressure at a given temperature.

4.3.2 Location of homopause

The homopause location is defined as $K = D$ where K would be 10^2 - 10^6 m^2 s^{-1} as discussed in Section 4.2.3. If the disk is dominated by oxygen atoms and has a small fraction of hydrogen atoms at 2000K, $D \sim K$ at $p \sim 10^{-3} - 10^{1}$ ($m_1 = 1$ g/mol, $m_2 = 16$ g/mol, $\sigma_1 = 2 \times 53$pm, $\sigma_2 = 2 \times 60$pm, $\bar{m} = m_2$, and the ideal gas

law are used in Equations 4.9 and 4.10). If the disk is dominated by SiO at 2000K, this condition is met at at $p \sim 10^{-3.5} - 10^{0.5}$ ($m_1 = 1$ g/mol, $m_2 = 30$ g/mol, $\sigma_1 = 2 \times 53$pm, $\sigma_2 = 2 \times 161$ pm, and $\bar{m} = m_2$). Thus, the pressure range of the homopause is estimated as $10^{-4} - 10^{1}$ (Pa).

4.3.3 Species present in the disk

Molecules and atoms present in the disk are shown in Figure 4.3. The left panels show the species that are present in the disk. As discussed in Section 4.3.1, the disk is dominated by silicate vapor at high temperatures or with small bulk water fraction. In Figure 4.3, cases with two different bulk water mixing ratio of water (0.1 and 0.01) are shown in the middle and left panels. At low temperature (1000K), the disk is dominated by SiO_2 and water is in the form of H_2O. The abundance of hydrogen is significantly low ($< 10^{-5}$). At higher temperatures (2000-3000 K), SiO_2 breaks into smaller species such as SiO, O, and O. In a similar manner, H_2O becomes H and O especially at lower pressures. Therefore, at the homopause (1500-2000K), the major elements can be SiO_2, O, and SiO. Lower parts of the disk ($p > 10^{-1}$ Pa) can be dominated by H_2O, but upper parts are dominated by H.

Figure 4.4 shows the case when the disk is dominated by water. The water can be dissociated to H and O at higher parts of the disk at 2000 K, but water stays as H_2O at 1500K. Since the homopause temperature of a water dominated disk ($T_{\rm mid} = 2500$ K with 1000ppm of water) is below 1500 K, H_2O is likely to be the dominant species at the level.

4.3.4 Hydrogen loss from the disk

Hydrogen loss from the disk is estimated from Equation (4.11). First, we consider the case when the disk temperature is high and the disk is dominated by silicate vapor, which would be the case when early stages of the disk. In this case, the hydrogen mixing ratio f is small (f can be smaller than 10^{-5} and not much larger than 0.1). The mean molecular weight $\bar{m}$ could be 60 g/mol (SiO_2), 30 g/mol (SiO), and the temperature would be 1500-2000K. Given that the location of homopause is around $z \sim 3R_\oplus$, the gravity $g(= 0.23\ \mathrm{ms}^{-2})$ and the scale height $H = RT/\bar{m}g$ can be computed. At 2000K, assuming that the disk is dominated by SiO, $f_1 = 0.1$, $\bar{m}$=30 g/mol, $H = 2.36 \times 10^6$ m, $m_2 = 30$ g/mol, $\sigma_2 = 2 \times 161$pm, and $b = 1.36 \times 10^{22} \mathrm{m}^{-1}\mathrm{s}^{-1}$ and the hydrogen escape flux is computed as $\phi = 5.7 \times 10^{14}$ atoms $\mathrm{m}^{-2}\mathrm{s}^{-1}$. Assuming the disk's surface area is $2\pi((5R_\oplus)^2 - R_\oplus^2)$ and the disk life time is 1000 years, this leads to the loss of 1.6×10^{15} kg of water. If the total mass of the disk is 1.5 lunar mass and the disk contains 100ppm of water, then the mass fraction of the lost water with respect to the total water 1.44×10^{-4}.

Next, we consider the case when the upper part of the disk is dominated by water. In this case, f could reach as high as 0.66 (H_2O = 2H + O) if the homopause temperature reaches 2000K. However, as Figure 4.1 shows, the homopause temperature is closer to 1500K and this dissociation is not likely to happen. In this case, hydrogen and water loss would be negligible. Nevertheless, it is still worthwhile to consider an extreme case; given that $f = 0.66$, $T = 2000$ K, $m_2 = 16$ g/mol, $\sigma_2 = 2 \times 60$pm, and $\bar{m} = 6.1$ g/mol with bulk 100 ppm of water, ϕ becomes 2.8 $\times 10^{15}$ atoms/m^2/s,

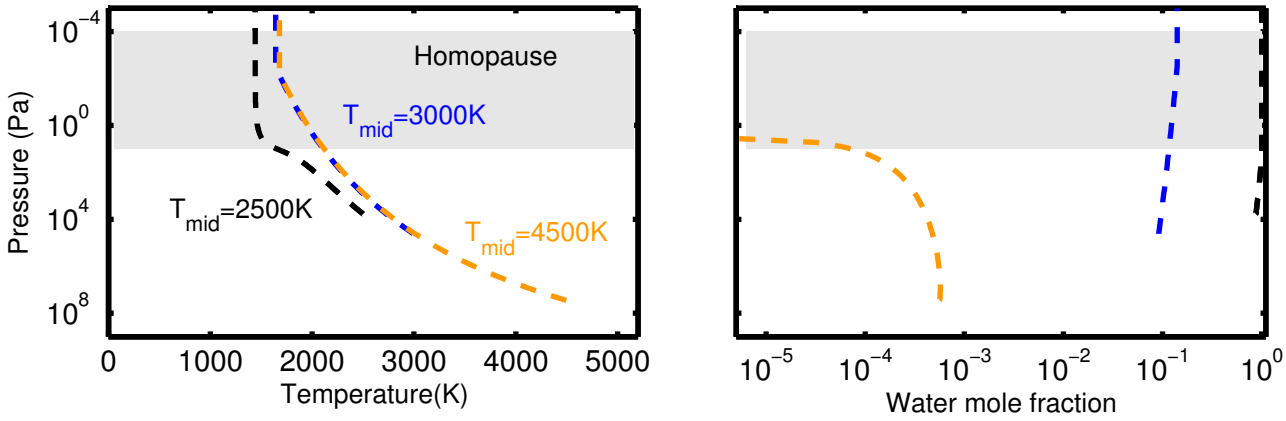

Figure 4.1: Vertical structure of the Moon-forming disk with 1000 ppm of water. The black, blue, and orange lines represent three different temperatures at the liquid-vapor interface at the mid-plane (2500K, 3000K, and 4500K, respectively). The left panel shows the temperature structure and the right panel shows the water mole fraction in the vapor phase. As the mid-plane temperature decreases, the disk becomes more water-rich. The homopause location is indicated by the shade.

which gives 7.03×10^{-5}. Thus, even this extreme case, the amount of lost water by hydrodynamic escape is too small to be detected by measurements of water content and D/H ratio of lunar rocks.

4.4 Discussion

4.4.1 Silicate disk with Mg_2SiO_4

In Section 5.3, we only consider a disk that contains SiO_2 and H_2O, but the composition of a realistic disk would be better modeled by Mg_2SiO_4. The temperature-pressure profile of the disk would not be significantly different given that the saturation vapor pressure of the bulk silicate Earth composition is similar to that of SiO_2 (Figure 3, Visscher and Fegley 2013), but species in the disk would be differ-

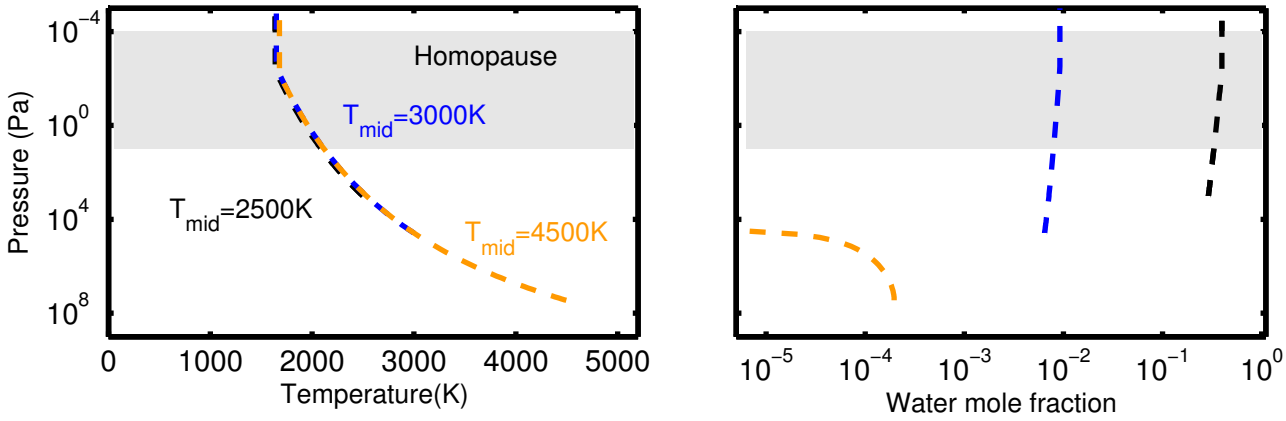

Figure 4.2: Vertical structure of the disk with 100ppm of water. The color scheme and general behaviors are the same as Figure 4.1. The abundance of water is less throughout the disk with respect to the case with 1000ppm.

ent. Figure 4.5 shows the abundance of each element given that the disk consists of Mg_2SiO_4 and H_2O. At a low temperature (1000K), the disk is dominated by Mg, but O becomes more dominant at higher temperatures. The general behavior of water is the same as that of the SiO_2 disk. The only difference is that the mixing ratio of water is smaller than that of a SiO_2 disk. This is because Mg_2SiO_4 break into a larger number of species (such as MgO and Mg). The values of $\bar{m}$, m_2, and σ_2 in the Mg_2SiO_4 disk would be different from the SiO_2 disk, but this does not change the outcome that water loss from the disk is minor.

4.4.2 Other volatile escape

In the previous sections, we only consider the escape of hydrogen, but other volatile elements, such as potassium K, sodium Na, and carbon C, can be considered in a similar framework. Zahnle et al. (1990) consider escape of a minor element with the

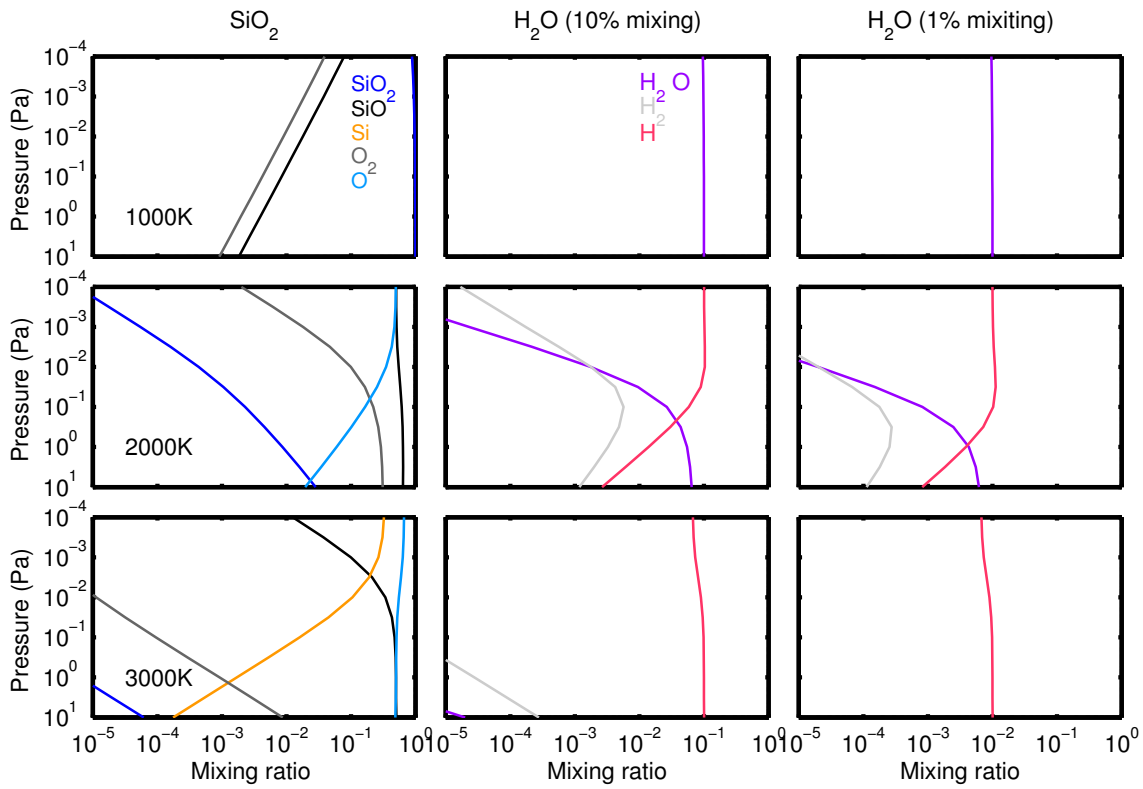

Figure 4.3: Species that are present in the disk at 1000K, 2000K and 3000K. SiO_2, SiO, Si, O_2, O, H_2O, H_2, and H are shown in blue, black, orange, dark grey, sky blue, purple, light grey, and red. The left column shows dissociation of SiO_2. The middle and right panels show dissociation of water with different mixing ratios; 0.9 mole of SiO_2 and 0.1 mole of H_2O are mixed in the middle column and 0.99 mole of SiO_2 and 0.01 mole of H_2O are mixed in the right column.

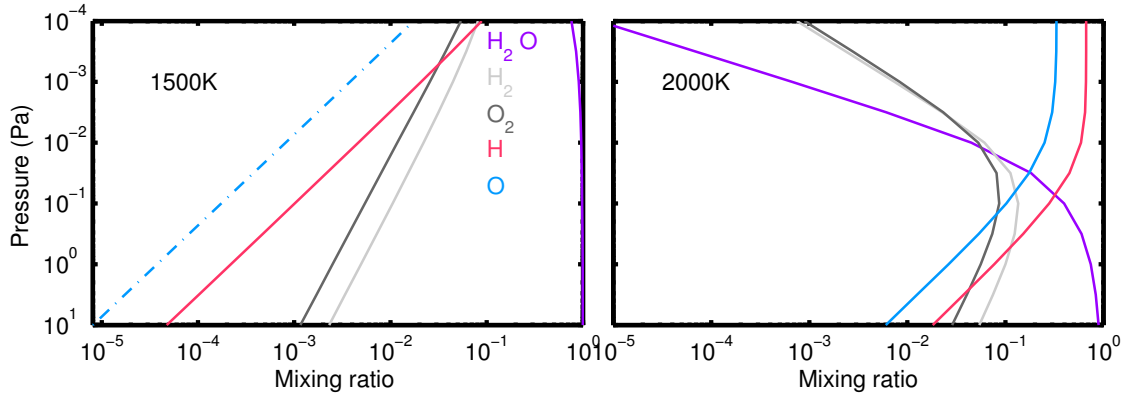

Figure 4.4: Dissociation of H_2O. At 1500K, H_2O is the dominant species while at 2000K H becomes dominant at lower pressures.

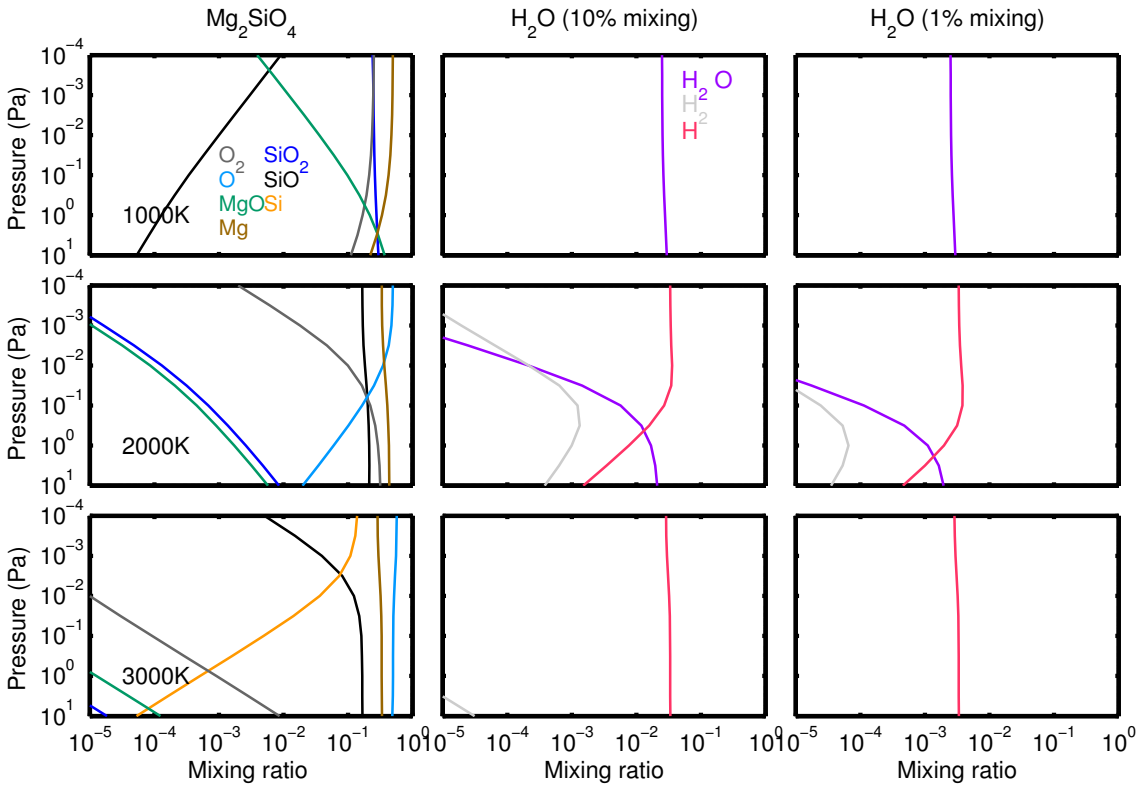

Figure 4.5: Dissociation of Mg_2SiO_4 and water. The color scheme is the same as Figure 4.3 with additional elements (MgO and Mg are shown in green and brown). The relative abundance of water is smaller than the case with SiO_2 because Mg_2SiO_4 breaks into a larger number of species.

presence of two major constituents (the mixing ratio of the minor element is much smaller than those of the major element and hydrogen). The escape flux of the minor constituent i, ϕ_i, is described as

$$\phi_i = \frac{F_i(r_0)\phi_1\alpha_i \exp(\alpha_i/r_0)}{\alpha_i + \gamma_i - \gamma_i \exp \alpha_i/r_0)} \tag{4.12}$$

where r_0 is the radial distance at a reference level (spherical coordinate), ϕ_1 is the escape flux of hydrogen, and $F_i = n_i/n_1$ where n_i and n_1 are the number densities of the element i and hydrogen. α_i and γ_i are described as

$$\alpha_i = \frac{r_0^2}{b_{1i}} F_2 \phi_{\mathrm{H}}(1 - x_2) + \frac{r_0^2}{b_{1i}}\phi_1 + \frac{r_0^2}{b_{2i}} x_2 F_2 \phi_1 - \frac{GM(m_i - m_1)}{kT} \tag{4.13}$$

$$\gamma_i = -r_0^2 \phi_1 \left(\frac{1}{b_{1i}} + \frac{F_2}{b_{2i}} \right) \tag{4.14}$$

where $x_i = \frac{\phi_i}{F_i \phi_1}$. Here, the subscript 2 indicates the dominant element (e.g. SiO and O). In the limit of $x_2 = 0$ (i.e. escape of the dominant species is negligible), the equation generally shows that the escape flux of heavier elements do not exceed the hydrogen flux. Given the abundance of potassium (240 ppm), sodium (2670 ppm), and carbon (120 ppm) in the Earth's mantle (McDonough and Sun, 1995), such weak escapes of these elements would not be significant enough to leave any detectable signatures.

4.4.3 Comparison among difference impact models

Our calculations show that at any temperature of the mid-plane, water escape is minor. This also indicates that volatiles would not escape from a high temperature ($T_{\rm mid} = 6000 - 7000$ K) disk predicted by the recent giant impact models. When the disk temperature is high, the mixing ratio of water in the upper part of the disk becomes small, therefore it becomes difficult for hydrogen to escape from the disk. Also, even if the initial temperature of the disk is high, the disk becomes colder as times progresses, the escape rate of the disk may become similar to that of one another.

4.4.4 Model validation

Our model includes several assumptions and approximations. First, we assume that heavy elements (such as O and SiO) do not escape and only hydrogen escapes (diffusion-limited regime). This assumption is valid in our case because the disk is dominated by elements that are dissociated from silicate vapor at high temperatures. At lower temperatures ($T_{\rm mid} < 2500$ K and the homopause temperature is ~ 1500 K), water exists as H_2O and the abundance of H is negligible.

Additionally, in previous and our studies on hydrodynamic escape, the velocity of escaping elements continue to increase as the distance from the planet increases. The flow reaches its sound speed and eventually escapes from the system as a wind. This approximation is likely to be valid if the exobase is above the critical point (Walker, 1982). Exobase is the location where the mean free path becomes equal to the scale

height and the critical point is where the velocity reaches the sound velocity. This indicates that the criterion is $l_c < H_{1c}$, where l_c is the mean free path and H_{1c} is the scale height of a light element and the subscript c describes the critical point. This is rewritten as (Zahnle et al., 1990)

$$\phi_l \geq \frac{m_{1g}}{RT}\frac{4b_{11}}{\sqrt{\pi}} \tag{4.15}$$

This becomes 2.44×10^{15} atoms/m^2/s, which is comparable to the hydrogen escape flux we estimate. It is possible the escape flux becomes smaller than this value. In this case, the hydrogen flux is very weak and heavy elements would not be dragged to space (Zahnle et al., 1990). In other words, the hydrogen flux in the diffusion-limited is considered as the upper limit of hydrogen flux. This makes our argument even stronger that hydrogen and volatile loss from the disk are minor.

In our analyses, we use the formulae of the diffusion-limited escape, which has been developed for spherical geometry, but this geometry is not exactly applicable for the Moon-forming disk. However, the disk is extended in the vertical direction ($z \sim 3R_\oplus$) and the geometry becomes similar to spherical. Furthermore, since the escape rate is limited by the diffusion rate, the geometry would not matter significantly.

We also assume that the disk does not evolve and stays as a disk for 100-1000 years. This is of course a inaccurate assumption because the disk would fragment and lead to the Moon accretion. Nevertheless, our model provides the upper limit of hydrogen escape given that the disk persists for such a long time.

4.5 Conclusions

We estimate the upper limit of hydrogen and volatile loss by hydrodynamic escape from the Moon-forming disk with various disk temperatures and water contents (100-1000 ppm). A liquid disk is present in the mid plane and it is sandwiched by a vapor disk, which has convective and radiative layers. When the temperature of the disk at the mid-plane is large (3000-4500 K), the disk is dominated by silicate vapor. Although water is dissociated to hydrogen and oxygen, their mixing ratio is very small. In contrast, if the mid-plane temperature is small (< 2500 K), an upper part of the disk can be dominated by water, but the ambient temperature (~ 1500 K) is so low that water stays in its molecular form (H_2O). Therefore, in either case hydrogen is not the major element and other heavy elements (such as O, SiO, SiO_2, and H_2O) are the dominant species in the disk. For hydrogen to escape, it has to diffuse out from this heavy element-rich disk. This escape regime is called diffusion-limited escape, which is an inefficient escape. We estimate the total mass of lost water and volatiles (Na, K, and C) given that the flow is in the diffusion-limited escape regime and find that the escape is inefficient that it would not remove water and the volatiles form the disk to the extent that the loss is observable. Therefore, we conclude that the diffusion-limited hydrodynamic escape is inefficient. To remove volatiles from the Moon-forming disk or from the Moon, another mechanism, such as losing volatiles from the disk to the Earth or degassing from the lunar surface, would be required.

Chapter 5

Controlled boiling on Enceladus

5.1 Introduction

Water plumes were first detected by Cassini near the south polar terrain (SPT) of Saturn's satellite Enceladus (Porco et al., 2006). These plumes consist of vapor and ice particles that emanate from the four prominent fractures, the so-called "tiger stripes", which are approximately 500 km long in total (Spitale and Porco, 2007; Porco et al., 2014). The vapor is mostly water but contains small fractions of volatiles (e.g., 5 % CO_2, 1 % CH_4, and 1 % NH_3, Hansen et al. 2011; Waite et al. 2009, 2011). The vapor production rate is reported as ~ 200 kgs^{-1} based on the measurements of the Ultraviolet Imaging Spectrometer (UVIS) (Hansen et al., 2011; Tian et al., 2007). The ice particles in the plumes are also dominated by water along with $\sim 0.5-2\%$ of salt (Postberg et al., 2011). The high salinity of the plumes suggests that the plume source is liquid water because ice particles condensed from vapor could not reach this high salinity (Postberg et al., 2011). Additionally, the reported ice to vapor mass ratios (I/V ratios) range from $< 0.1 - 0.2$ (Kieffer et al., 2009; Gao et al., 2016) to 0.3-0.7 (Porco et al., 2006; Hansen et al., 2006; Hedman et al., 2009; Ingersoll and Ewald, 2011). This variation stems from the difference in modeling the scattering of light by the ice particles. The I/V ratio is an important indicator of the plume source, given that a flow evaporating from ice cannot have a high I/V ratio (< 0.05, Schmidt et al. 2008; Ingersoll and Pankine 2010).

The tiger stripes are the source not only for the plumes, but also for strong infrared radiation. Based on the Cassini's Composite Infrared Spectrometer (CIRS), the total heat flux from the SPT was estimated to be as low as 5.4-5.8 GW (Spencer et al., 2006;

Abramov and Spencer, 2009) and as high as 15.8 GW (Howett et al., 2011). This high heat flow may include the contribution from surrounding areas, which is difficult to distinguish from re-radiated sunlight. Recently, Spencer et al. (2013) have reported that the heat flow could be ∼4.2 GW after eliminating these contributions. The thermal emission is especially strong near the tiger stripes (Spencer et al., 2006; Porco et al., 2006). Analyzing data from the Visual and Infrared Mapping Spectrometer (VIMS) shows that the thermal emission is most intense near the stripes, in the form of small-scale hot spots (∼ 10 m) (Blackburn et al., 2012; Spencer et al., 2012; Goguen et al., 2013). Thus it appears that the thermal emission along the tiger stripes is associated with the plume activity (e.g., Ingersoll and Pankine, 2010; Blackburn et al., 2012; Spencer et al., 2012; Goguen et al., 2013; Porco et al., 2014).

Another key observation is that the plume activity depends on the orbit of Enceladus. The plume brightness, caused by the scattering of light by ice particles, reaches its maximum near the apocenter (Hedman et al., 2013; Nimmo et al., 2014). This is probably because the cracks are most widely open at the apocenter, as predicted by the tidal-opening model (Hurford et al., 2007), and they lead to higher plume mass fluxes. This model is further supported by the correlation between the locations of the most active plumes and high normal tidal stresses (Nimmo et al., 2014; Porco et al., 2014). There is some time lag between the apocenter and the maximum plume brightness. Several mechanisms have been suggested regarding this issue (Nimmo et al., 2014; Běhounková et al., 2015; Kite and Rubin, 2015).

In summary, these observations performed by Cassini seem to indicate that water

vapor and ice particles are evaporating from a subsurface liquid ocean and that the hot spots are associated with the plumes. However, we still do not have a clear understanding of the connection between the plume dynamics and these observations. In this paper, we attempt to build a dynamical model that can explain the observed plume mass flow rate, heat flow from the tiger stripes, and I/V ratio of the plumes. We assume that the plumes originate from a liquid-vapor interface a few km deep. The water evaporation rate from the liquid ocean is controlled mainly by the back pressure arising from the friction of the walls (discussed in Section 5.2.2). We call this a controlled boiling mechanism in this paper. We use similar assumptions to those of Ingersoll and Pankine (2010) (IP10 hereafter), but one of the major difference is that we assume a subsurface liquid ocean and that the evaporation is controlled by the back pressure, whereas IP10 assumes that the plumes originate from vapor sublimation from the ice walls. Using this model, we attempt to clarify the following connections: Can a subsurface ocean explain the observed (1) heat flow, (2) the plume production rate, (3) size of the hot spots, and (4) the ice to vapor ratio? We propose that the evaporation of water does not freeze the liquid ocean, as discussed in Section 5.4.3. This is further discussed in our paired paper (Ingersoll and Nakajima 2016, herein Part 2). It should be noted here that the ratio of the heat flow and the vapor production rate determines the ratio of radiated heat to latent heat carried with the vapor (approximately 10:1), which has been discussed in previous literature (e.g., Ingersoll and Pankine, 2010).

5.2 Model

We solve steady-state equations of the flow and flow-wall interaction. Water vapor and ice particles evaporate from the liquid ocean and ascend towards the ice surface. Along the way, part of the vapor condenses onto the surrounding ice walls and releases its latent heat to the walls. The heat is transported by conduction in the ice and eventually reaches the ice surface. Subsequently, the heat is released into space by radiation. The parameters used here are the crack width δ, crack depth D, and solid mass fraction at the bottom of the flow (liquid-vapor interface) s_0. Here, the crack width is the distance between the ice walls, and the crack depth is the distance from the liquid surface (vapor-liquid boundary) to the surface of the ice (Figure 5.1). We consider vertically uniform and nonuniform crack widths.

5.2.1 Governing equations

The conservation equations of mass, momentum, and energy of the flow are solved simultaneously. The mass conservation is written as

$$\frac{d}{dz}(\rho v \delta) = E, \tag{5.1}$$

where z is the upward coordinate, ρ is the density, v is the velocity, and E is the vapor mass flux from the ice walls to the flow (i.e., $E < 0$ when vapor condenses onto

the ice walls). Equation (5.1) can be written as

$$v\delta\frac{d\rho}{dz} + \rho\delta\frac{dv}{dz} + \rho v\frac{d\delta}{dz} = E. \tag{5.2}$$

The momentum equation is

$$\frac{d}{dz}(\rho v^2\delta) = -\delta\frac{dp}{dz} - \tau - \rho g\delta + v(E - E^*), \tag{5.3}$$

where p is the pressure, g is the gravitational acceleration, and $E^* = E$ when $E > 0$ and $E^* = 0$ when $E < 0$. τ is the stress from the wall ($= 12\eta v/\delta + 2C_{\rm d}\rho v^2$, where η is the dynamic viscosity and $C_{\rm d}$ is the drag coefficient). The four terms on the right hand side represent the contribution from the pressure gradient, stress from the walls, gravitational force, and the momentum loss due to vapor condensation onto the walls, respectively. Using the relation that $\frac{d(\rho v^2\delta)}{dz} = Ev + \rho v\delta\frac{dv}{dz}$, Equation (5.3) can be written as

$$\rho v\delta\frac{dv}{dz} = -\delta\frac{dp}{dz} - \tau - \rho g\delta - vE^*. \tag{5.4}$$

The energy equation is

$$\begin{aligned}\frac{d}{dz}\left[\rho v\delta\left(u + \frac{p}{\rho} + \frac{1}{2}v^2 + gz + L(1-s)\right)\right] = \\ E\left(u + \frac{p}{\rho} + gz + L\right) + \frac{1}{2}v^2(E - E^*) - \frac{\tau}{v}C_p\Delta T,\end{aligned} \tag{5.5}$$

where u is the internal energy, L is the latent heat, s is the solid mass fraction, and C_p is the specific heat at a constant pressure. $\Delta T = T - T_{\rm w}$, where T and $T_{\rm w}$ are the

temperatures of the flow and ice walls. The equation on the left hand side includes the fluxes of the enthalpy, kinetic energy, gravitational potential and latent heat. The first and second terms on the right hand side represent the energy fluxes removed from the flow. The third term represents cooling due to turbulent heat transport between the flow and ice walls (IP10). Using Equations (5.2), (5.4), and (5.5), the energy equation becomes

$$\rho v\delta\left(C_v\frac{dT}{dz}-L\frac{ds}{dz}\right)+p\delta\frac{dv}{dz}=-pv\frac{d\delta}{dz}$$
$$+\frac{p}{\rho}E+v\tau+\frac{1}{2}v^2E^*+LsE-\frac{\tau}{v}C_p\Delta T. \tag{5.6}$$

Here, $du = C_v dT$ is assumed, where C_v is the specific heat at a constant volume.

Equations (5.2), (5.4), and (5.6) are the same as those of IP10 except for small modifications. First, we define z in the opposite direction. Furthermore, our energy equation does not include the term $-E^*C_v\Delta T$; this term is zero because E is always negative and thus $E^* = 0$ (Section 5.3.1).

The mass flux to the walls E is calculated as

$$E=-2\left(\frac{p}{\sqrt{2\pi RT/M}}-\frac{p_{\mathrm{w}}}{\sqrt{2\pi RT_{\mathrm{w}}/M}}\right), \tag{5.7}$$

where R is the gas constant, M is the molecular weight (18 g/mol), and p_{w} is the saturation vapor pressure at the temperature of the wall ($p_{\mathrm{w}} = A\exp[-B/T_{\mathrm{w}}]$, where $A = 3.63\times10^{12}$ Pa and $B = 6147$ K). The factor of two in Equation (5.7) stems from the fact that vapor condenses on the two walls.

In a steady state, water vapor condenses onto the ice walls and releases the latent heat to the walls (heat flux due to latent heat release, $F_{\rm s}$). The heat is conducted through ice (heat flux due to conduction, $F_{\rm c}$) and is eventually emitted to space by radiation (heat flux due to radiation $F_{\rm r}$). Here, we assume that this relationship holds at each depth, i.e., $F_{\rm s}(d) = F_{\rm c}(d) = F_{\rm r}(d)$, where d is the depth ($d \equiv D - z$, Figure 5.1).

Now we consider the wall-vapor interaction as follows. The heat due to the condensation of water vapor onto the ice walls is given as

$$F_{\rm s}(d) = -2E(d)L. \tag{5.8}$$

Let $T_{\rm s}$ and $T_{\rm e}$ be the surface temperature and effective temperature of the ice ($T_{\rm e} = 68$ K, which corresponds to the re-radiated sunlight), respectively. The radiative heat flux $F_{\rm r}$ is

$$F_{\rm r}(d) = 2\sigma \left(T_{\rm s}^4(d) - T_{\rm e}^4 \right), \tag{5.9}$$

where σ is the Stefan-Boltzmann constant. The heat flux due to conduction within the ice is (same as IP10)

$$F_{\rm c}(d) = 4k \frac{T_{\rm s}(d) - T_{\rm w}(z)}{\pi d}, \tag{5.10}$$

where k is the thermal conductivity ($= 3$ Wm$^{-1}K^{-1}$). Although this is an approximate expression of heat conduction within the ice, the temperature profile of the ice is similar to the one derived by solving the two dimensional diffusion equation using an analytical solution of E (discussed in 5.3.1). The difference is $< 15\%$ at $d < 500$m

and $< 5\%$ at greater depths. $\frac{d\rho}{dz}$, $\frac{dv}{dz}$, $\frac{dp}{dz}$, $\frac{du}{dz}$, $\frac{dT}{dz}$, and $\frac{ds}{dz}$ are solved simultaneously using the mass, momentum, and energy conservation equations, as well as the relations in which $du = C_v dT$ and $p = (1-s)\rho RT/M = A\exp(-B/T)$. E, $T_{\rm s}$, and $T_{\rm w}$ are derived based on Equations (5.7) - (5.10).

The constants used here are $g = 0.11$ m/s^2, $C_v = C_p = 2000$ J/kg/K, $C_{\rm d} = 0.002$ (IP10, and similar values have been listed in other studies, such as Hartmann 1994), $L = 2.8 \times 10^6$J/kg, and $\eta = 0.925 \times 10^{-5}(T/300)^{1.1}$ Pa s (Crifo, 1989).

5.2.2 Boundary conditions

We assume that water evaporates from a liquid ocean that exists at the bottom of the crack. This is an important difference between our model and IP10, which does not consider a subsurface ocean. Another difference is that we consider that evaporation from the ocean is suppressed and hence controlled by the back pressure p_0. The evaporation rate at the bottom of the flow is expressed as

$$\rho_0 v_0 \delta = \frac{(p_l(T_l) - p_0)}{\sqrt{2\pi RT_l/M}}\delta, \tag{5.11}$$

where the subscripts 0 and l represent parameters of the flow and liquid, respectively. The temperature of the liquid surface T_l is the same as the triple point (273K). The triple point is reduced if the ocean is salty, but the effect is minor and is ignored here. The pressure of the liquid is p_l(273K)=611 (Pa) (saturation vapor pressure). The difference between p_l and p_0 causes evaporation from the liquid (no evaporation where $p = p_0$). It should be noted that the liquid is boiling because p_l is larger than

p_0. As discussed in Part 2, some bubbles may form below the liquid surface.

The top boundary of the flow is defined where the velocity reaches its local sound speed. To satisfy this condition, the pressure at the bottom of the flow p_0 is iteratively determined. The velocity should not reach the sound speed inside the crack for the entropy to increase in the direction of the flow (Chapter 98, Landau and Lifshitz 1987). We use $v = c$ as the surface boundary condition, ignoring conditions above the surface where the gas expands into vacuum. We ignore cases where the flow does not reach the surface due to complete condensation onto the walls. These cases arise for cracks with small width and large depth, and are discussed further in Section 5.4.2.

Other conditions include the crack width δ, crack depth D, and solid mass fraction at $z = 0$, s_0, are listed in Table 5.1 given that the crack width is constant ($d\delta/dz = 0$). It should be noted that the crack width is not well constrained by the observations because the resolutions of the Cassini images are no better than a few tens of meters per pixel. For a straight crack, $\delta = 0.05 - 0.1$ m are used. A wider δ is possible, but it would lead to a much larger mass flow rate than the observed value (Section 5.3.4). In this study D is $1.5 - 4.5$ km, which is probably a reasonable range. The ice shell thickness has been estimated as a few tens of kilometers ($21 - 40$ km, Iess et al. 2014; McKinnon 2015; Thomas et al. 2016) and water would fill the crack up to 92% of the ice shell due to isostasy because the density of ice is ~ 0.92 g/cm^3 (the corresponding crack depth d becomes $1.7 - 3.2$ km). s_0 varies between 0 and 0.1. Additionally, we choose the total length of the crack as another parameter. The total length of the

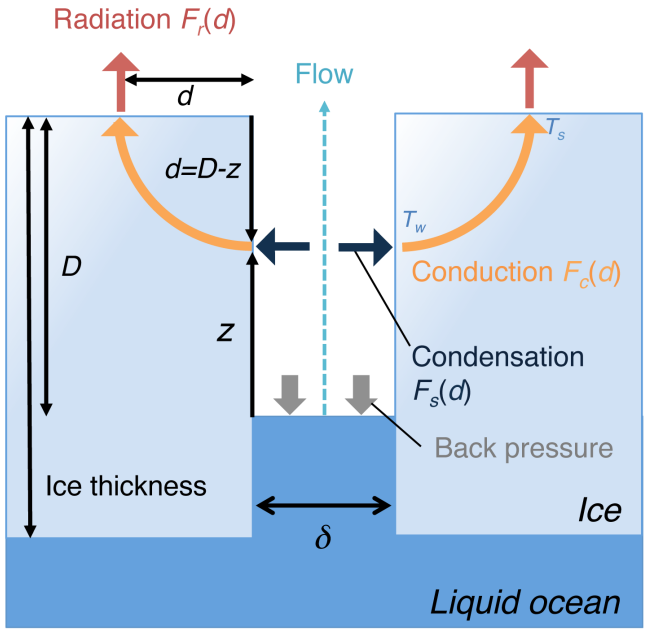

Figure 5.1: Schematic view of our model with a uniform crack width ($d\delta/dz = 0$). The evaporation is controlled by the back pressure of the flow. At each depth d, some of the vapor condenses onto the ice walls and emits its latent heat to the ice walls ($F_{\rm s}(d)$). The heat is conducted in the ice ($F_{\rm c}(d)$) and eventually emitted to space ($F_{\rm r}(d)$).

tiger stripes is approximately 500 km, but the total length of the cracks can be larger if each tiger stripe consists of several unresolved smaller cracks (discussed in Section 5.4.1). In addition, we investigate cases with non-uniform crack widths ($d\delta/dz \neq 0$). These results are listed in Tables 5.2 and 5.3.

Case	δ	D	s_0	$\Delta p/p$ (%)	Mass flow rate from liquid (kg/s)	Mass flow rate at surface (kg/s)	Heat flow (GW)	$s(z=D)$
1	0.050	1.5	0.00	4.12	696	141	1.56	0.00
2	0.050	1.5	0.05	4.28	725	156	1.56	0.13
3	0.050	1.5	0.10	4.49	760	194	1.59	0.29
4	0.050	1.8	0.00	3.59	606	44	1.60	0.00
5	0.075	1.5	0.00	7.16	1814	1245	1.58	0.00
6	0.075	2.0	0.00	5.77	1464	852	1.62	0.00
7	0.075	2.0	0.10	6.25	1587	912	1.70	0.14
8	0.075	2.5	0.00	4.87	1234	621	1.73	0.00
9	0.075	3.0	0.00	4.23	1071	454	1.73	0.00
10	0.075	3.5	0.00	3.75	950	315	1.79	0.00
11	0.075	4.0	0.00	3.38	856	204	1.84	0.00
12	0.075	4.0	0.01	3.39	860	226	1.78	0.00
13	0.075	4.0	0.05	3.51	891	239	1.82	0.10
14	0.075	4.0	0.10	3.68	934	253	1.82	0.24
15	0.075	4.5	0.00	3.08	781	133	1.82	0.00
16	0.100	1.5	0.00	10.21	3452	2887	1.55	0.00
17	0.100	2.0	0.00	8.40	2840	2159	1.70	0.00
18	0.100	2.5	0.00	7.17	2425	1697	1.70	0.00
19	0.100	3.0	0.00	6.28	2122	1303	1.76	0.00
20	0.100	3.5	0.00	5.59	1891	1221	1.85	0.00
21	0.100	4.0	0.00	5.05	1708	1055	1.83	0.00

Table 5.1: Summary of the initial conditions and results. The second to fourth columns from the left represent crack width δ, crack depth D, and the solid mass fraction at the liquid-vapor interface s_0. The fifth to ninth columns represent the fraction of pressure difference at the bottom of the flow, the mass flow rate per 500 km at the bottom and surface, the heat flow per 500 km, and the solid mass fraction at the ice surface (at $d = 0$). It should be noted that the ice to vapor ratio is described as $s/(1-s)$.

Case	δ_0	D	s_0	X	n	$\Delta p/p$ (%)	Mass flow rate from liquid (kg/s)	Mass flow rate at surface (kg/s)	Heat flow (GW)	$s(z=D)$
22	0.100	4.0	0.00	0.5	10	2.64	888	256	1.79	0.00
23	0.100	4.0	0.00	0.5	30	2.63	873	251	1.79	0.00
24	0.100	4.0	0.05	0.5	10	2.75	925	268	1.79	0.09
25	0.100	4.0	0.00	0.25	10	4.37	1475	817	1.84	0.00

Table 5.2: Summary of the initial conditions and results with $d\delta/dz \neq 0$. δ is described as $\delta = \delta_0(1 + X\sin(2n\pi z/D))$. While the heat flow does not depend on $d\delta/dz$, the mass flow rate is sensitive to the value. A tortuous crack increases the back pressure; therefore, it decreases the mass flow rate.

Case	δ_b	δ_t	D	s_0	Y	$\Delta p/p$ (%)	Mass flow rate from liquid (kg/s)	Mass flow rate at surface (kg/s)	Heat flow (GW)	$s(z=D)$
26	1	0.050	2.0	0.00	40	0.19	646	59	1.67	0.00
27	1	0.050	2.0	0.00	100	0.21	646	163	1.65	0.00
28	1	0.075	4.0	0.00	20	0.27	917	230	1.85	0.00

Table 5.3: Summary of the initial conditions and results with $d\delta/dz < 0$. δ is expressed as $\delta_\mathrm{t} + (\delta_\mathrm{b} - \delta_\mathrm{t})\exp(-z/Y)$. Here, Y is expressed in meters. In these two cases, the surface area of the liquid ocean is large, which help avoiding freezing the ocean surface (discussed in Section 5.4.3).

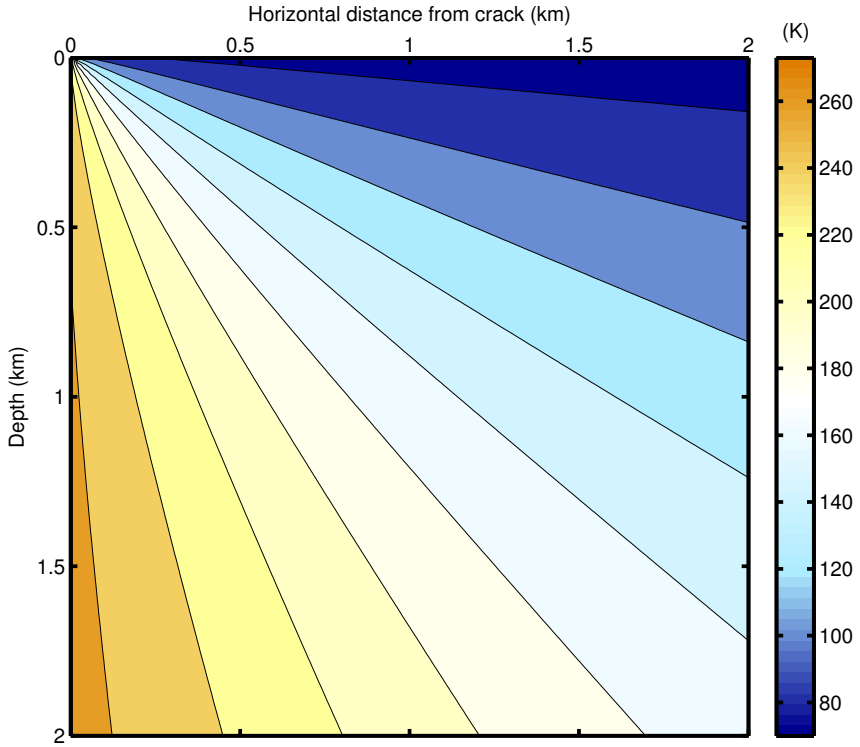

Figure 5.2: Temperature of the ice. This temperature profile corresponds to Case 11 ($\delta = 0.075$ m and $D = 4$ km), but the profile is very similar to those in the other cases. The vertical axis is the depth d and the horizontal axis is the distance from the crack in km.

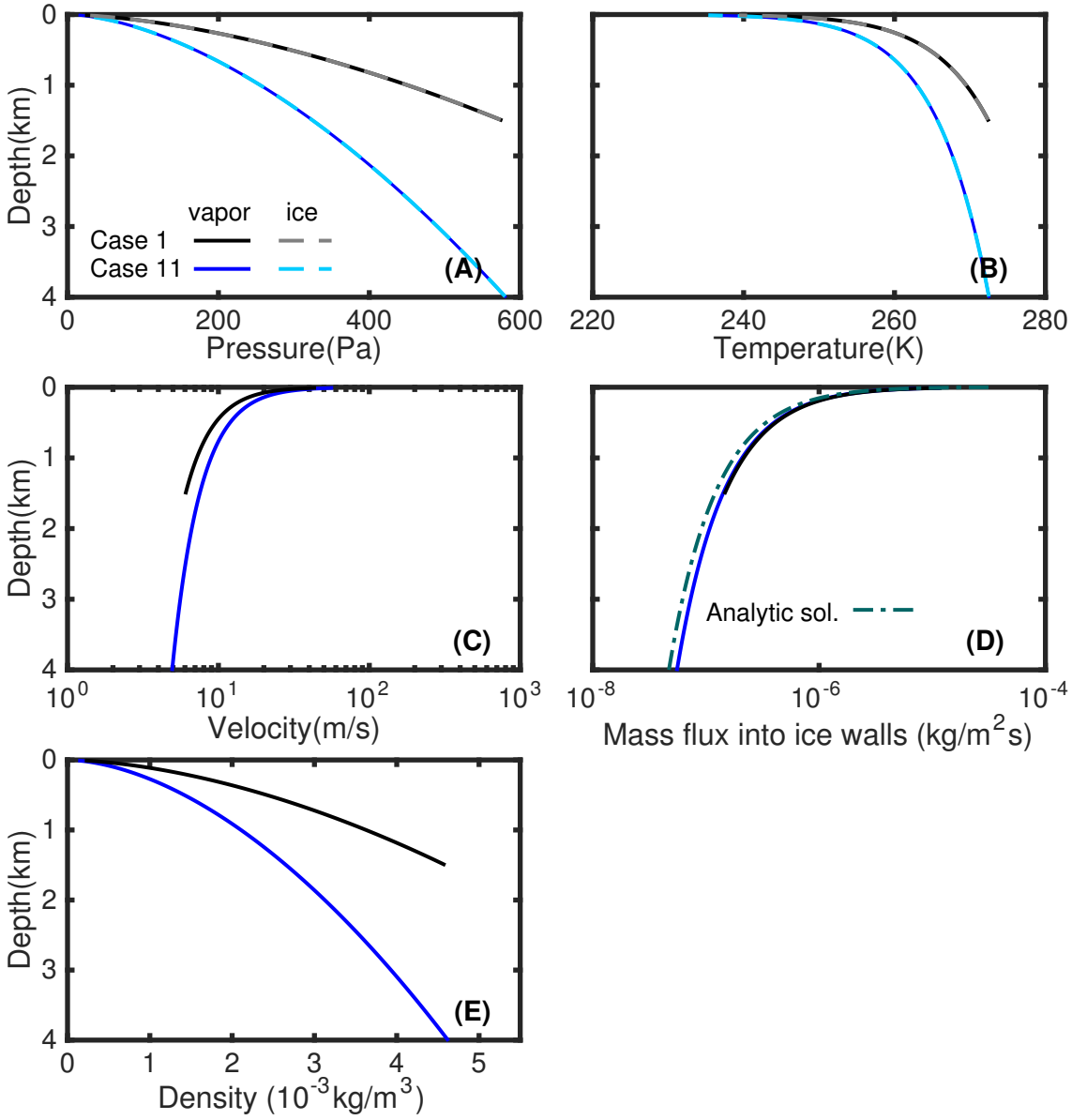

Figure 5.3: Vertical profiles of the flow and ice walls. The black and gray lines correspond to Case 1 ($\delta = 0.05$ m and $D = 1.5$ km) and the blue and sky-blue lines correspond to Case 11 ($\delta = 0.075$ m and $D = 4$ km). The black and blue lines represent the physical parameters of the flow and the gray and sky-blue lines represent those of the ice walls. The green chain line in D represents an analytic solution for the mass flux into the ice walls ($-E$).

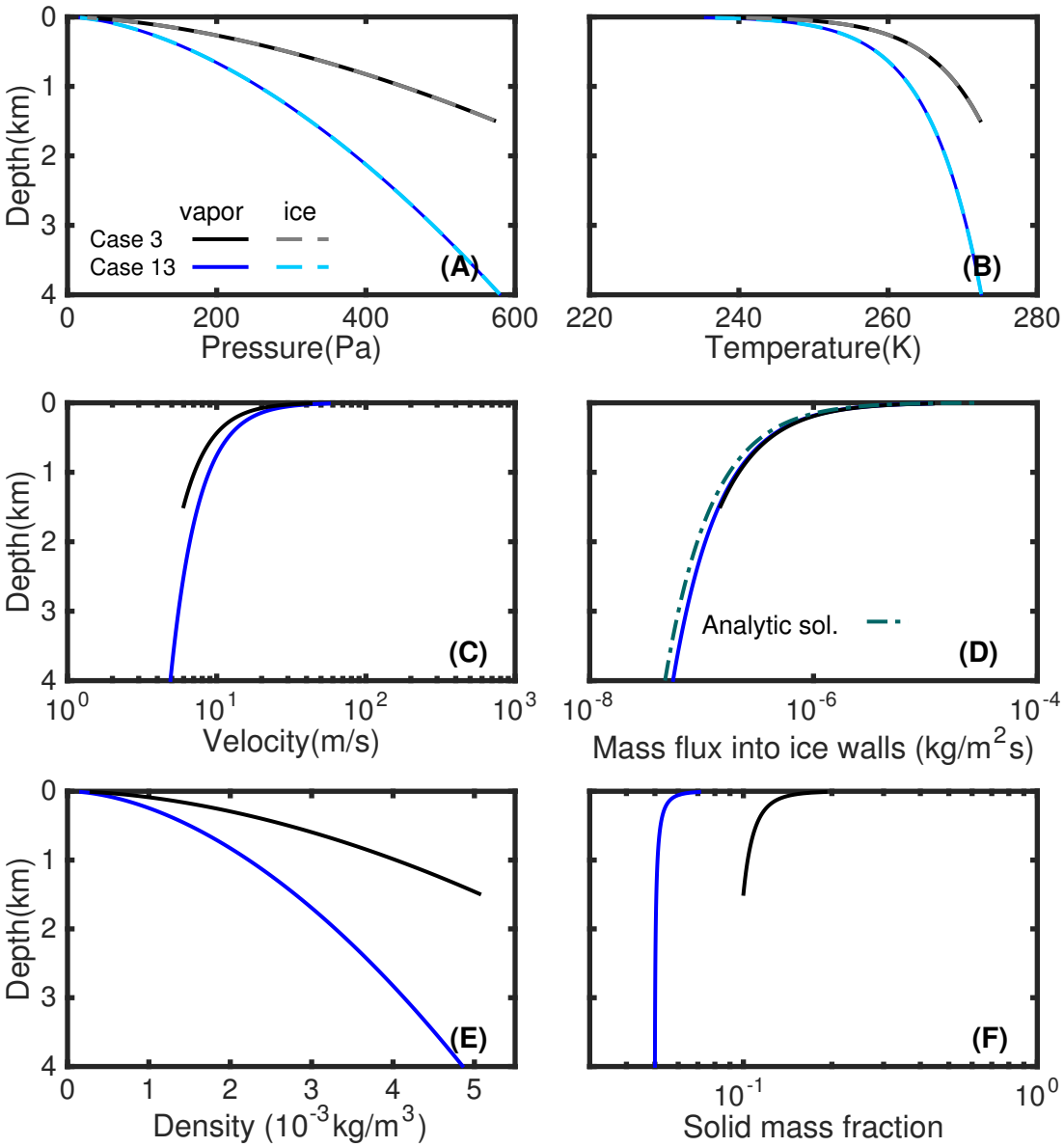

Figure 5.4: Vertical profiles of the flow and ice walls at $s_0 > 0$ (Case 3: $\delta = 0.05$m and $D = 1.5$ km and Case 13: $\delta = 0.075$m and $D = 4$ km). The color scheme is the same as that of Figure 5.3. Unlike the $s_0 = 0$ cases, the solid mass fraction increases as the flow approaches the surface.

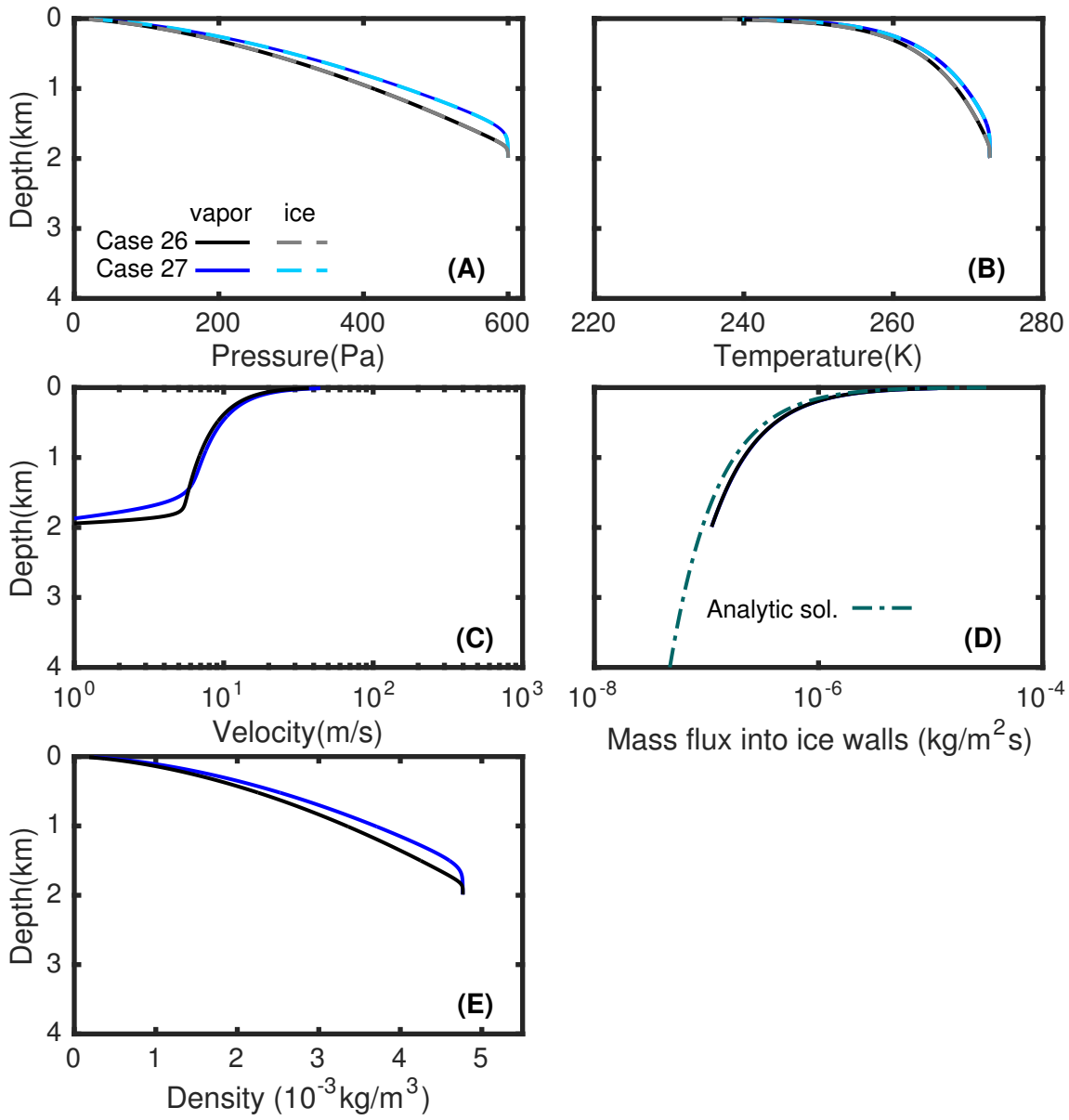

Figure 5.5: Vertical profiles of the flow and ice walls at $d\delta/dz \neq 0$ (Case 26 and Case 27). The crack is wide at the bottom of the flow ($\delta = 1$m) and becomes sharply narrower at shallower depths. In Case 26, the crack depth is $(0.05 + 0.95\exp(-z/40))$ m and in Case 27 it is $(0.05 + 0.95\exp(-z/100))$ m.

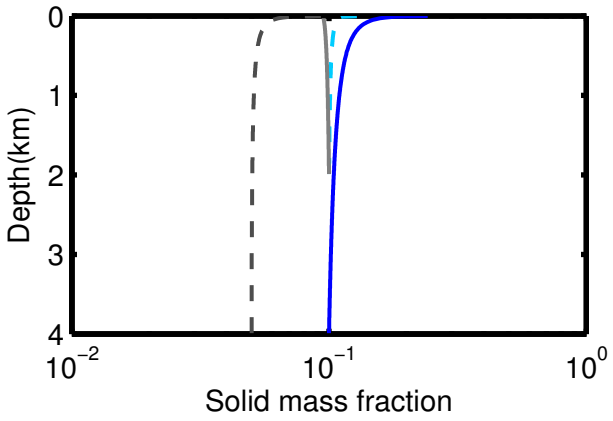

Figure 5.6: The solid mass fraction s as a function of depth d with various s_0. The sky-blue dashed ($\delta = 0.075$ m, $D = 2$ km, and $s_0 = 0.1$), gray dashed ($\delta = 0.075$ m, $D = 4$ km, and $s_0 = 0.05$), blue solid ($\delta = 0.075$ m, $D = 4$ km, and $s_0 = 0.1$), and gray solid ($\delta = 0.1$ m, $D = 2$ km, and $s_0 = 0.1$) lines correspond to Case 7, 13, 14, and 17, respectively

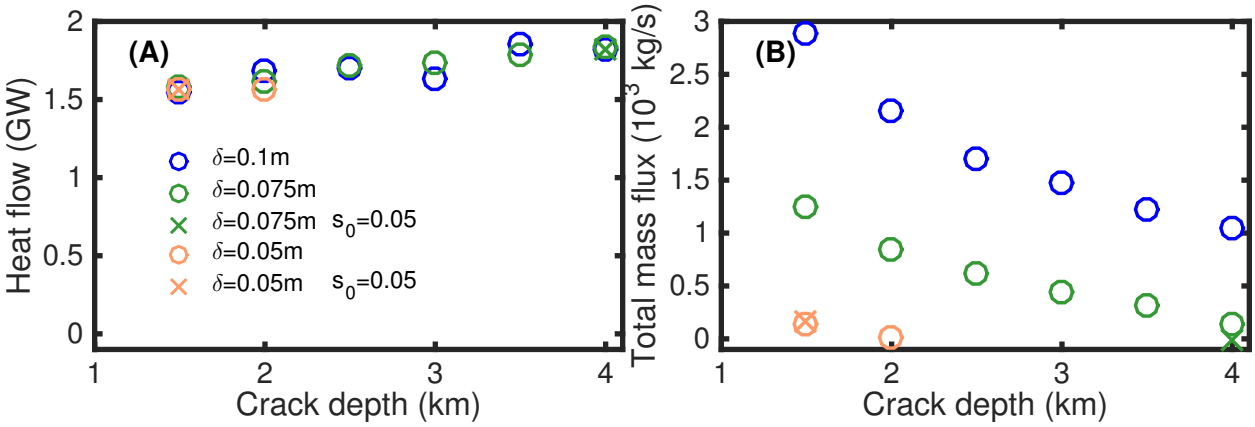

Figure 5.7: Summary of the resulting heat flow and total mass flow rate that are emitted to space per 500 km (part of seventh and eighth columns in Table 5.1). Blue, green and orange represent cases when $\delta = 0.1, 0.075$, and 0.05m, respectively. The circle represents $s_0 = 0$ and the cross represents $s_0 = 0.05$.

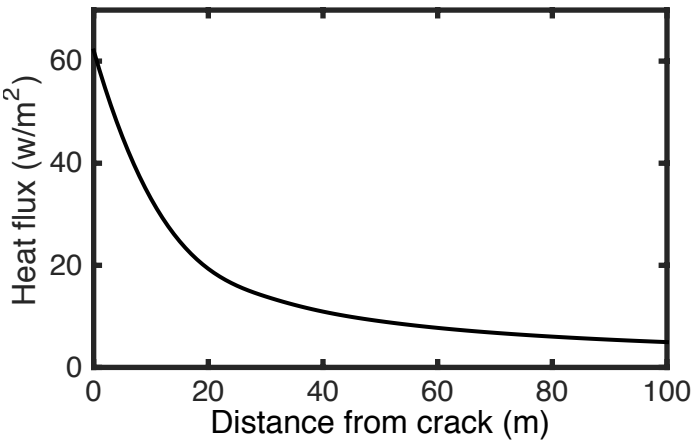

Figure 5.8: Heat flux to space as a function of the distance from the crack. The heat flux is most intense near the center of the crack and decreases sharply within several tens of meters away from the crack.

5.3 Results

The initial conditions and results are summarized in Table 5.1 when the crack width is uniform ($d\delta/dz = 0$). The fifth column from the left represents $\Delta p/p = (p_\mathrm{l} - p_0)/p_\mathrm{l}$. The sixth and seventh columns represent the production rate of the flow (including vapor and solid) per 500 km at the liquid-vapor interface (at the bottom) and at the surface of Enceladus ($d = D - z = 0$), respectively. The eighth and ninth columns are the heat flow per 500 km and the solid mass fraction at the surface ($d = D - z = 0$), respectively. The temperature profile of the ice wall is shown in Figure 5.2.

5.3.1 Vertical structure

Figure 5.3 shows the vertical profiles of pressure, temperature, flow velocity, mass flux into the ice walls ($-E$), and density for Case 1 ($\delta = 0.05$ m and $D = 1.5$ km) and Case 11 ($\delta = 0.075$ m and $D = 4$ km). The vertical axis is the depth d in km. We find

that the solid mass fraction s remains zero at all depths (not shown in Figure 5.3) if the solid mass fraction at the liquid vapor interface s_0 is zero. As shown in Figure 5.3A and B, we find that the pressure and temperature differences between the flow and ice walls are very small ($|p - p_{\rm w}| < 1$ Pa and $|T - T_{\rm w}| < 1$ K), as predicted by IP10.

The velocity continues to increase until the flow reaches the surface of Enceladus (Figure 5.3C). When the total mass flow rate that goes into the ice per 500 km ($2\int_0^D -E dz \times 500$ km and this is typically $500 - 600$ kg/s) is negligible with respect to the rate from the liquid ($\rho_0 v_0 \delta \times 500$ km), $\rho v \delta$ is considered to be nearly constant with the crack. When this is the case, the density ρ and pressure p decrease while the velocity v increases as the flow approaches the ice surface. In contrast, when $\rho_0 v_0 \delta \times 500$ km is comparable to or smaller than 500 - 600 kg/s, v can begin to decrease or even reverse its sign as the flow approaches the ice surface. These solutions correspond to a transfer of mass and energy from the liquid interface to the walls of the crack, with none of it reaching the icy surface and no production of plumes. Such cases have been eliminated from our "successful" results because they would not produce plumes.

As shown in Figure 5.3D, the mass flux that goes into the ice walls ($-E$) is always positive (i.e. E is always negative) and is insensitive to the choice of the initial conditions. The green dashed line corresponds to an analytic solution by assuming $T_{\rm w}$ =const.= 273K and by solving equations (5.8)-(5.10) (two equations and two unknowns, E and $T_{\rm s}$). Therefore, the heat flow is basically determined by thermal

conduction and radiation, and is insensitive to the structure of the flow. The density of the flow (Figure 5.3E) is very close to that of saturated water vapor.

The cases at $s_0 = 0.1$ and 0.05 are shown in Figure 5.4 (Cases 3 and 13). The value of s at the ice surface is given in the last column of Table 5.1. Here, Case 3 uses the same initial conditions as Case 1 ($\delta = 0.05$ m and $D = 1.5$ km) and Case 13 uses the same conditions as Case 11 ($\delta = 0.075$ m and $D = 4.0$ km) except that $s_0 > 0$ in Cases 3 and 13. The vertical structure of the flow with $s > 0$ is very similar to that with $s_0 = 0$ except that s continues to increase as the flow approaches the ice surface (Figure 5.4F). This behavior is further discussed in Section 5.3.3.

5.3.2 Tortuous and tapering cracks

In the calculations above, we assume that the crack is straight ($d\delta/dz = 0$), but the actual crack can be tortuous or tapering ($d\delta/dz \neq 0$). The initial conditions and results with $d\delta/dz \neq 0$ are listed in Tables 5.2 and 5.3. Although the heat flow is insensitive to $d\delta/dz$, the mass flow rate can be sensitive to $d\delta/dz$. In Cases 22 - 25 (Table 5.2), δ is sinusoidal and described as $\delta = \delta_0(1 + X\sin(2n\pi z/D))$, where the constants δ_0, X, and n are listed in the table. In Cases 22 - 24, the mass flow rate is much smaller ($250-270$ kg/s) than the rate in Case 21 (1055 kg/s), even though these cases have the same averaged crack width and depth. This is mainly because tortuous cracks have larger stresses from the wall and therefore larger back pressures. When δ is small (minimum at $2n\pi z/D = (3/2 + 2k)\pi$ where k is an integer), v increases and this leads to a large value of $\tau = 12\eta v/\delta + 2C_{\mathrm{d}}\rho v^2$. The mass flow rate is mainly

controlled by the amplitude X (the mass flow rates are 256 kg/s and 817 kg/s with $X = 0.5$ and 0.25 in Cases 22 and 25, respectively) and the wavelength of the sinusoid does not significantly affect the outcome (the mass flow rates are 256 kg/s and 251 kg/s with $n = 10$ and 30 in Cases 22 and 23, respectively). The overall structure of the flow is insensitive to s(Case 24). In Cases 26 – 28, we consider a crack which is wide (1 m) at the bottom and becomes quickly narrower as z increases. δ is expressed as $\delta_{\mathrm{t}} + (\delta_{\mathrm{b}} - \delta_{\mathrm{t}}) \exp(-z/Y)$. The constants δ_{t} (δ at the top), δ_{b} (δ at the bottom), and Y are listed in Table 5.3. The crack remains relatively wide in Case 27 ($Y = 100$ m) while it quickly narrows in Case 26 ($Y = 40$ m). This leads to a larger mass flux in Case 26, because the back pressure is smaller. The overall flow structure with $d\delta/dz \neq 0$ (Figure 5.5) is similar to that with $d\delta/dz = 0$, but the structures at the lower part of the flow (near the liquid-vapor interface) are different. For example, in Case 26, the velocity near the interface is small (< 1 m/s) but it sharply increases to 10 m/s (Figure 5.5 C). This transition occurs because δ sharply decreases while $\rho v \delta$ and ρ remain almost constant. Implications of this tapering cases are discussed in Section 5.4.3.

5.3.3 Behavior of solid mass fraction

Figure 5.6 shows behavior of the solid mass fraction s as a function of s_0, D and δ. The the sky-blue dashed line represents $s_0 = 0.1, \delta = 0.075$ m, and $D = 2$ km (Case 7). The gray dashed, and blue lines represent $s_0 = 0.05$, and 0.1, respectively, at $D = 4$ km, $\delta = 0.075$ m (Cases 13 and 14). The figure shows the general trend that

a large s_0 leads to a large s.

This is explained by Equation (5.6); the relation $L\frac{ds}{dz} = \frac{Ls(-E)}{\rho v \delta} + ...$ (E is always negative) indicates that a large s leads to a large ds/dz. In other words, vapor condenses onto the ice walls leaving ice particles, which increase s of the flow. The effects of D and δ can be analyzed in a similar manner. Equation (5.6) is rewritten as $L\frac{ds}{dz} = \frac{1}{\rho v \delta}[p\delta\frac{dv}{dz} - v\tau + Ls(-E) + ...] + ...$ (terms that have relatively small contributions are not explicitly written). The sum of the terms in the square bracket at a given depth d is insensitive to D or δ, but $\frac{1}{\rho v \delta}$ depends on these parameters in the sense that a large D and a small δ give a large $\frac{1}{\rho v \delta}$ and hence a large s (Section 5.3.4).

5.3.4 Heat flow and mass flow rate

Figure 5.7 shows the heat flow and the mass flow rate per 500 km that are emitted to space. The vertical axis in Figure 5.7A is the total heat flow provided to the ice walls, which is calculated as $2 \times \int_0^D -ELdz \times 500\text{km}$. The heat flow is approximately $\sim$ 1.5 - 1.8 GW and is insensitive to the initial conditions. It should be noted that this estimate of the heat flow does not include the contribution from the liquid. Given that 273K liquid fills 92% of 30km (ice shell thickness), its contribution can be computed by integrating $2 \times \int F_c(z')dz' \times 500\text{km}$ (0 km $< z' <$ 27.6 km) where z' is the distance from the bottom of the ice shell. $F_c(z')$ is analytically computed assuming T_w = 273 K (Section 5.3.1). The contribution from the liquid becomes ~ 0.8 GW and therefore the total heat flow becomes $\sim 2.3 - 2.6$ GW. This value is comparable to the current theoretical estimate (e.g., $1.5 - 3.1$ GW according to IP10

and $3.3-3.9$ GW according to Abramov and Spencer 2009). If there is a global ocean below 27.6 km, it will make a small global contribution to the heat flow, but it will be almost impossible to distinguish from re-radiated sunlight.

In contrast, the total mass flux emitted to space, which includes vapor and ice particles, highly depends on the crack width and crack depth (Figure 5.7B). The total mass flow rate increases as δ increases and as D decreases because a large δ and a small D decrease the back pressure p_0 (i.e., increase $\Delta p/p$ as shown in Table 5.1). The mass flow rate also moderately depends on the solid mass fraction s_0 in the sense that a larger s leads to a larger $\Delta p/p$ because the back pressure decreases ($p_0 = (1 - s_0)\rho_0/RT_0$).

It should be noted that cases at $D > 2$ km and $\delta = 0.05$ m do not have solutions that meet the top boundary condition ($v = c$). This is because such a flow completely condenses onto the ice walls and it could not reach the surface. Thus, in these cases, the flow does not produce observable plumes, which may provide interesting implications (discussed in Section 5.4.2).

Figure 5.8 shows calculated thermal radiation flux from the ice surface. The horizontal axis corresponds to the distance from the crack on the surface (only the nearest 100 m from the crack is shown). The heat flow is intense near the crack, but the intensity drops significantly as the distance increases. The heat flux from within 25 m from the crack constitutes $\sim 80\%$ of the total heat flux.

5.4 Discussion

5.4.1 Multiple crack model

Here, we consider the possibility that the total length of the tiger stripes is larger than 500km. It is possible that we are not detecting small scale fractures due to the limited resolution of observations (IP10 and Abramov and Spencer 2009). We define the total length of the cracks as $f\times$ 500 km, where f is chosen to match the observed heat flux. As discussed in Section 5.3.4, the typical value of the heat flow for a 500 km long crack is $\sim 2.3 - 2.6$ GW, which indicates $f \sim 4.2/2.5 = 1.7$ (the total heat flow is 4.2 GW, Spencer et al. 2013). If the heat flow is as high as 15 GW (Howett et al., 2011), f becomes ~ 6.

Given $f = 1.7$, the total vapor production rate becomes $141 \times 1.7 = 240$ kg/s in Case 1 and 133 kg/s $\times 1.7 = 226$ kg/s in Case 15. These rates are relatively close to the observed value ~ 200 kg/s (Hansen et al., 2011). Given that the crack depth D is estimated as $1.7 - 3.2$ km, a preferable δ would be between 0.05 and 0.075 m when $d\delta/dz = 0$. In contrast, when $\delta = 0.1$ m (Cases 16 - 21), the vapor production rates are too high. Alternatively, if the crack is as large as 1 m at the bottom of the flow and becomes sharply narrow at shallower depths (Cases 26 - 28), the observed mass flow rate and heat flow can be explained. A tapering crack can form naturally because vapor condenses more efficiently near the ice surface (Section 5.4.3).

5.4.2 Comparison with orbital variations

Our model could help explain some of the observed features of the plumes and surface thermal anomalies near the tiger stripes. As discussed in Section 5.3.4, our model predicts a larger mass flow rate emitted to space at a larger crack width δ. This is consistent with the observations that the plume brightness is largest at the apocenter (Hedman et al., 2013; Nimmo et al., 2014; Ingersoll and Ewald, 2016) where the crack width is expected to be largest (Hurford et al., 2007) given that the brightness (due to scattering by the ice particles) is proportional to the total mass of the plumes. Another interesting point is that our model predicts that the plume velocity does not depend on the orbital location. The temperature of the ice walls is close to $\sim$ 240 K and is insensitive to δ. Given that the plume velocity is approximately the same as the local sound speed ($c = \sqrt{\gamma RT/M}$ where $\gamma = 1.33$), the plume velocity would not depend on δ or its orbital location, which may be consistent with the observation that the plume scale height is independent of orbital position (Nimmo et al., 2014). In contrast, both Hedman et al. (2013) and Ingersoll and Ewald (2016) find that the brightness falloffis greater at apocenter, implying a lower velocity of ice particles than at pericenter. It It is possible that ice particles are slower than the vapor (Schmidt et al., 2008), but our model does not address this question because we assume that the ice particles are sufficiently small to be entrained in the flow (of course, this assumption would break down if the ice particles become large enough).

An important issue here is that this estimated crack width (0.05 - 0.075 m for a straight crack) may be too small because this is smaller than the crack motion

per tidal cycle (0.5 m slip, Nimmo et al. 2007). We point out here that the crack width we calculated may be an underestimate because of the following reasons. In our analysis, we assume that all the plumes contribute to the mass flow rate and heat flow simultaneously, but it is possible that some plumes only contribute to the heat flow. This can occur when all the vapor coming from the ocean condensed onto the ice walls (this is the case when δ is small and D is large as discussed in Section 5.3.4) and therefore the flow does not reach the ice surface or produce plumes. Alternatively, sufficiently tortuous cracks can be wider (which is more consistent with the estimated tidal displacements) without violating the constraints provided by the heat flux and mass flux. If this is the case, wider cracks on average are allowed without producing higher mass flow rates than the observed value.

Furthermore, our model may indicate that the total heat flow is insensitive to the crack width or orbital position, which may also be consistent with the observation that the heat flow does not change over time (varied by less than 15 % between July 2005 and November 2006, Abramov and Spencer 2009). It should be noted that our model does not describe the long-term evolution of the plumes; therefore, further investigation is required for this issue. Additionally, our model can explain a wide range of the ice to vapor (I/V) ratios. The I/V ratio ($= s/(1-s)$ at $d = 0$) is most sensitive to the value at the bottom of the flow, s_0. If s_0 at the bottom is larger than ~ 5 %, the I/V ratio of the plumes reach 0.1 or higher, but if s_0 is 1% or less, the I/V ratio becomes close to zero. Bursting bubbles from the liquid ocean may produce such a high solid mass fraction at the interface (Part 2), but it is not clear yet what

the typical value of s_0 would be.

Our model tracks physics per unit length and therefore does not put any constraint on the shape of the crack in the horizontal direction. Whereas a horizontally long crack would produce a collimated jets made of vapor and ice particles (Hansen et al., 2011; Postberg et al., 2011), or possibly more spread features (Spitale et al., 2015), a short crack would produce an isolated jet plume (Porco et al., 2014). A small-scale crack in the horizontal direction can form if the crack width δ is non-uniform along the stripes. A narrow region will be quickly sealed by the condensation of water vapor (Section 5.4.3), which could produce an isolated small-scale crack. If the crack is modeled better by a circular shape, the total heat flow can be computed as $\int -2\pi E\delta dz$ multiplied by the number of jets. A potential issue is that the total number of jets may need to be much higher than 100 to explain the observed high heat flow (if we assume that all of the plumes reach the ice surface, as discussed in Section 5.4.1).

5.4.3 Further questions

A potential issue of our model is that the crack would be sealed up within $\sim$ a few months, as noted by IP10, because water vapor continues to condense onto the ice walls. The sealed crack may be reopened or new cracks may be opened by tidally driven motions (Nimmo et al., 2007, 2014; Ingersoll and Ewald, 2016).

Another question is how to keep the water at the liquid-vapor interface from freezing. Postberg et al. (2009) suggest that the subsurface ocean may freeze because

evaporating water vapor removes latent heat from the liquid. They suggest that a significantly large surface area of the liquid ocean (a few to tens square kilometers) is needed to avoid freezing. Here, we argue that the surface area can be smaller than this size. As discussed in Part 2, if the crack width δ is ~ 1 m at the bottom of the flow (the surface area of the ocean is $1 \times 1.7 \times 500$ km $= 0.85$ km^2) and becomes narrower at shallower depths (e.g. Cases 26 – 28), the liquid ocean can avoid freezing. Such tapering crack could occur because more vapor condenses onto the ice walls at smaller d (e.g., Figure 5.3D). Maintaining a liquid ocean is an important issue; thus we have included extensive discussions in Part 2.

5.5 Conclusions

We investigate the hypothesis that flows of vapor and ice particles originating from a subsurface ocean are responsible for the plume activities and intense heat flow along the tiger stripes. The heat generated by the vapor condensation onto the ice walls is conducted through the ice and is eventually emitted to space by thermal radiation. We solve the flow dynamics and flow-ice wall interactions by considering the possibility that the total crack length can be larger than that of the tiger stripes (500km). We find that the observed mass flow rate (200 kg/s) can be explained if the crack width is 0.05-0.075 m for a vertically uniform crack. Wider cracks are not favorable because it would produce a larger mass flow rate than the observed value, but they are allowed if some flows do not reach the surface due to condensation of water vapor onto the ice walls. Alternatively, wider cracks are possible if the cracks are

sufficiently tortuous. The heat flow (4.2 GW) can be explained if the total length of the cracks is ~ 1.7 times larger than that of the tiger stripes. Furthermore, a tapering crack, which means that the crack is wide (1 m) near the liquid-vapor surface and becomes sharply narrow (0.05 – 0.075 m) at shallower depths, can also explain these observed mass flow rate and heat flow. The mass flow rate is larger with a wider crack width, which is consistent with the observation that the plume mass flux is largest at the apocenter where the crack width is the largest. Our model predicts a strong thermal emission from the ice surface near the tiger stripes (< 25 m), which can explain the observed hot spots near the stripes. Furthermore, we find that the ice to vapor ratio in the plumes is sensitive to the ice mass fraction of the flow at the liquid-vapor interface.

Bibliography

Abe, Y., Matsui, T., 1986. Early evolution of the Earth: Accretion, atmosphere formation, and thermal history. J. Geophys. Res. 91, E291.

Abe, Y., Ohtani, E., Okuchi, T., RIghter, K., Drake, M., 2000. Water in the Early Earth. Origin of the Earth and Moon. Univ. of Arizona Press, Tucson , pp. 413 – 433.

Abramov, O., Spencer, J.R., 2009. Endogenic heat from Enceladus south polar fractures: New observations, and models of conductive surface heating. Icarus 199, 189–196.

Armytage, R.M.G., Georg, R.B., Williams, H.M., Halliday, A.N., 2012. Silicon isotopes in lunar rocks: Implications for the moons formation and the early history of the earth. Geochim. Cosmochia. Ac. 77, 504–514.

Atreya, S., 1986. Atmospheres and Ionospheres aof the Outer Planets and Their Satellites. Physics and Chemistry in Space .

Barnes, J.J., Franchi, I.A., Anand, M., Tartse, R., Starkey, N.A., Koike, M., Sano, Y., Russell, S.S., 2013. Accurate and precise measurements of the D/H ratio and

hydroxyl content in lunar apatites using NanoSIMS. Chemical Geology 337-338, 48–55.

Benz, W., Cameron, A.G.W., Melosh, H.J., 1989. The origin of the moon and the single impact hypothesis. III. Icarus 81, 113–131.

Benz, W., Slattery, W.L., Cameron, A.G.W., 1986. The origin of the moon and the single-impact hypothesis. I. Icarus 66, 515–535.

Benz, W., Slattery, W.L., Cameron, A.G.W., 1987. The origin of the moon and the single-impact hypothesis. II. Icarus 71, 30–45.

Blackburn, D.G., Goguen, J.D., Buratti, B.J., Clark, R.N., Howell, R.R., Spencer, J.R., 2012. Detection of thermal emission from Enceladus' Tiger stripes with Cassini VIMS. Lunar Planet. Sci. 43rd , 1532.

Boyce, J.W., Liu, Y., Rossman, G.R., Guan, Y., Eiler, J.M., Stolper, E.M., Taylor, L.A., 2010. Lunar apatite with terrestrial volatile abundances. Nature 466, 466–9.

Boyce, J.W., Tomlinson, S.M., McCubbin, F.M., Greenwood, J.P., Treiman, A.H., 2014. The lunar apatite paradox. Science 344, 400–2.

Boyce, J.W., Treiman, A.H., Guan, Y., Ma, C., Eiler, J.M., Gross, J., Greenwood, J.P., Stolper, E.M., 2015. The chlorine isotope fingerprint of the lunar magma ocean. Sci. Adv. 1, E1500380.

Běhounková, M., Tobie, G., Cadek, O., Čhoblet, G., Porco, C., Nimmo, F., 2015. Tim-

ing of water plume eruptions on Enceladus explained by interior viscosity structure. Nat. Geosci. 8, 601–604.

Cameron, A.G.W., 2000. Higher-resolution Simulations of the Giant Impact. Univ. of Arizona Press, Tucson, In: Canup, R. M., Righter, K. (Eds.), Origin of the earth and Moon.

Cameron, A.G.W., Benz, W., 1991. The origin of the moon and the single impact hypothesis. IV. Icarus 92, 204–216.

Cameron, A.G.W., Ward, W.R., 1976. The origin of the moon. Lunar Planet. Sci. 7th , 120.

Canup, R.M., 2004. Simulations of a late lunar-forming impact. Icarus 168, 433–456.

Canup, R.M., 2005. A giant impact origin of Pluto-Charon. Science 307, 546–50.

Canup, R.M., 2008a. Accretion of the Earth. Philos Trans A Math Phys Eng Sci 366, 4061–75.

Canup, R.M., 2008b. Lunar-forming collisions with pre-impact rotation. Icarus 196, 518–538.

Canup, R.M., 2012. Forming a moon with an earth-like composition via a giant impact. Science 338, 1052–1055.

Canup, R.M., 2014. Lunar-forming impacts: processes and alternatives. Phil. Trans. R. Soc. A 372, 20130175.

Canup, R.M., Asphaug, E., 2001. Origin of the moon in a giant impact near the end of the earth's formation. Nature 412, 708–712.

Canup, R.M., Barr, A.C., Crawford, D.A., 2013. Lunar-forming impacts: High-resolution SPH and AMR-CTH simulations. Icarus 222, 200–219.

Canup, R.M., Salmon, J., 2014. On an impact origin of Phobos-Deimos. DPS meeting 46 , 501.09.

Canup, R.M., Visscher, C., Salmon, J., Fegley, B., 2015. Depletion of volatile elements in the Moon due to incomplete accretion within an impact-generated disk. Nature Geoscience , in press.

Canup, R.M., Ward, W.R., Cameron, A.G.W., 2001. A scaling relationship for satellite-forming impacts. Icarus 150, 288–296.

Carlson, R.W., Lugmair, G.W., 1988. The age of ferroan anorthosite 60025 - Oldest crust on a young moon? Earth Planet. Sci. Lett. 90, 119–130.

Chamberlain, J., Hunten, D.M., 1987. Theory of Planetary Atmospheres, Second Edition. International Geophysics 36, 481.

Chandrasekhar, S., 1961. Hydrodynamic and hydromagnetic stability. Oxford Univ. Press, Oxford .

Chase, M., Davies, C., Downey, J., Frurip, D., Mcdonald, R., Syverud, A., 1985. Janaf thermochemical tables 3rd edition. J. Phys. Chem. Ref. Data 14, 9271856.

Citron, R.I., Aharonson, O., Perets, H., Genda, H., 2014. Moon formation from multiple large impacts. Lunar Planet. Sci 45th , 2085.

Crifo, J.F., 1989. Inferences concerning water vapour viscosity and mean free path at low temperatures. Astron. Astrophys. 223, 365–368.

Ćuk, M., Stewart, S.T., 2012. Making the moon from a fast-spinning earth: A giant impact followed by resonant despinning. Science 338, 1047–1052.

Dahl, T.W., Stevenson, D.J., 2010. Turbulent mixing of metal and silicate during planet accretion - and interpretation of the HfW chronometer. Earth Planet. Sci. Lett. 295, 177–186.

Dauphas, N., Burkhardt, C., Warren, P.H., Fang-Zhen, T., 2014. Geochemical arguments for an Earth-like Moon-forming impactor. Phil. Trans. R. Soc. A 372, 20130244.

Deng, L., Gong, Z., Fei, Y., 2008. Direct shock wave loading of mgsio3 perovskite to lower mantle conditions and its equation of state. Phys. Earth Planet. In. 170, 210–214.

Desch, S.J., Taylor, G.J., 2013. Isotopic mixing due to interaction between the protolunar disk and the Earth's atmosphere. Lunar Planet. Sci. 44th , 2566.

Elkins-Tanton, L.T., 2008. Linked magma ocean solidification and atmospheric growth for Earth and Mars. Earth Planet. Sci. Lett. 271, 181–191.

Elkins-Tanton, L.T., Grove, T.L., 2011. Water (hydrogen) in the lunar mantle: Results from petrology and magma ocean modeling. Earth and Planetary Science Letters 307, 173–179.

Epstein, S., Taylor, H.P., 1974. D/H and $^{18}O/^{16}O$ ratios of H20 in the "rusty" breccia 66095 and the origin of "lunar water". Proc. Fifth Lunar Sci. Conf. 2, 1839–1854.

Evrard, A.E., 1988. Beyond n-body - 3d cosmological gas dynamics. MNRAS 235, 911–934.

Fiquet, G., Dewaele, A., Andrault, D., 2000. Thermoelastic properties and crystal structure of $MgSiO_3$ perovskite at lower mantle pressure and temperature conditions. Geophys. Res. Lett. 27, 21–24.

Fitoussi, C., Bourdon, B., 2012. Silicon Isotope Evidence Against an Enstatite Chondrite Earth. Science 335, 1477–1480.

Franchi, I.A., Wright, I.P., Sexton, A.S., Pillinger, C.T., 1999. The oxygen-isotopic composition of earth and mars. Meteoritics and Planetary Science 34, 657–661.

Füri, E., Deloule, E., Gurenko, A., Marty, B., 2014. New evidence for chondritic lunar water from combined D/H and noble gas analyses of single Apollo 17 volcanic glasses. Icarus 229, 109–120.

Gao, P., Kopparla, P., Zhang, X., Ingersoll, A.P., 2016. Mobile lid convection beneath Enceladus' south polar terrain. Icarus 264, 227–238.

Genda, H., Abe, Y., 2003. Modification of a proto-lunar disk by hydrodynamic escape of silicate vapor. Earth Planets Space 55, 2003.

Gingold, R.A., Monaghan, J.J., 1977. Smoothed particle hydrodynamics - theory and application to non-spherical stars. MNRAS 181, 375–389.

Goguen, J.D., Buratti, B.J., Brown, R.H., Clark, R.N., Nicholson, P.D., Hedman, M.M., Howell, R.R., Sotin, C., Cruikshank, D.P., Baines, K.H., Lawrence, K.J., Spencer, J.R., Blackburn, D.G., 2013. The temperature and width of an active fissure on Enceladus measured with Cassini VIMS during the 14 April 2012 South Pole flyover. Icarus 226, 1128–1137.

Greenwood, J.P., Itoh, S., Sakamoto, N., Warren, P., Taylor, L., Yurimoto, H., 2011. Hydrogen isotope ratios in lunar rocks indicate delivery of cometary water to the Moon. Nature Geoscience 4, 79–82.

Halliday, A.N., 2012. The origin of the moon. Science 338, 1040–1041.

Hansen, C.J., Esposito, L., Stewart, A.I.F., Colwell, J., Hendrix, A., Pryor, W., Shemansky, D., West, R., 2006. Enceladus' Water Vapor Plume. Science 311, 1422–1425 (2006).

Hansen, C.J., Shemansky, D.E., Esposito, L.W., Stewart, A.I.F., Lewis, B.R., Colwell, J.E., Hendrix, A.R., West, R.A., Waite, J.H., Teolis, B., Magee, B.A., 2011. The composition and structure of the Enceladus plume. Geophys. Res. Lett. 38, n/a–n/a.

Hartmann, D.L., 1994. Global physical climatology. volume 56 of *International Geophysics Series*.

Hartmann, W.K., Davis, D.R., 1975. Satellite-sized planetesimals and lunar origin. Icarus 24, 504–514.

Hauri, E.H., Saal, A.E., Rutherford, M.J., Van Orman, J.A., 2015. Water in the Moon's interior: Truth and consequences. Earth and Planetary Science Letters 409, 252–264.

Hauri, E.H., Weinreich, T., Saal, A.E., Rutherford, M.C., Van Orman, J.A., 2011. High pre-eruptive water contents preserved in lunar melt inclusions. Science 333, 213–5.

Hedman, M.M., Gosmeyer, C.M., Nicholson, P.D., Sotin, C., Brown, R.H., Clark, R.N., Baines, K.H., Buratti, B.J., Showalter, M.R., 2013. An observed correlation between plume activity and tidal stresses on Enceladus. Nature 500, 182–4.

Hedman, M.M., Nicholson, P.D., Showalter, M.R., Brown, R.H., Buratti, B.J., Clark, R.N., 2009. Spectral Observations of the Enceladus Plume with Cassini-Vims. Astrophys. J. 693, 1749–1762.

Hernquist, L., Katz, N., 1989. TREESPH - A unification of SPH with the hierarchical tree method. Astron. Astrophys. Sup. 70, 419–446.

Herwartz, D., Pack, A., Friedrichs, B., Bischoff, A., 2014. Identification of the giant impactor Theia in lunar rocks. Science 344, 1146–50.

Howett, C.J.A., Spencer, J.R., Pearl, J.C., Segura, M., 2011. High heat flow from Enceladus south polar region measured using 10600 cm?1 Cassini/CIRS data. J. Geophys. Res. 116, E03003.

Hui, H., Peslier, A.H., Zhang, Y., Neal, C.R., 2013. Water in lunar anorthosites and evidence for a wet early Moon. Nature Geosci. 6, 177–180.

Hunten, D.M., 1973. The Escape of Light Gases from Planetary Atmospheres. Journal of Atmospheric Sciences 30, 1481–1494.

Hunten, D.M., Pepin, R.O., Walker, J.C.G., 1987. Mass fractionation in hydrodynamic escape. Icarus 69, 532–549.

Hurford, T.A., Helfenstein, P., Hoppa, G.V., Greenberg, R., Bills, B.G., 2007. Eruptions arising from tidally controlled periodic openings of rifts on Enceladus. Nature 447, 292–294.

Ida, S., Canup, R.M., Stewart, G.R., 1997. Lunar accretion from an impact-generated disk. Nature 389, 353–357.

Iess, L., Stevenson, D.J., Parisi, M., Hemingway, D., Jacobson, R.A., Lunine, J.I., Nimmo, F., Armstrong, J.W., Asmar, S.W., Ducci, M., Tortora, P., 2014. The gravity field and interior structure of Enceladus. Science 344, 78–80.

Ingersoll, A.P., Ewald, S.P., 2011. Total particulate mass in Enceladus plumes and mass of Saturns E ring inferred from Cassini ISS images. Icarus 216, 492–506.

Ingersoll, A.P., Ewald, S.P., 2016. Decadal timescale variability of the Enceladus plumes inferred from Cassini images, submitted .

Ingersoll, A.P., Nakajima, M., 2016. Controlled boiling on Enceladus. 2. Model of the liquid-filled cracks. Icarus, accepted. .

Ingersoll, A.P., Pankine, A.A., 2010. Subsurface heat transfer on Enceladus: Conditions under which melting occurs. Icarus 206, 594–607.

Jackson, I., Ahrens, T.J., 1979. Shock wave compression of single-crystal forsterite. J. Geophys. Res. 84, 3039–3048.

Jacobson, S.A., Morbidelli, A., Raymond, S.N., O'Brien, D.P., Walsh, K.J., Rubie, D.C., 2014. Highly siderophile elements in Earth's mantle as a clock for the Moon-forming impact. Nature 508, 84–87.

Kaib, N.A., Cowan, N.B., 2015. The feeding zones of terrestrial planets and insights into Moon formation. Icarus 252, 161–174.

Karato, S., 2014. Asymmetric shock heating and the terrestrial magma ocean origin of the Moon. Proceedings of the Japan Academy, Series B 90, 97–103.

Kieffer, S.W., Lu, X., McFarquhar, G., Wohletz, K.H., 2009. A redetermination of the ice/vapor ratio of Enceladus plumes: Implications for sublimation and the lack of a liquid water reservoir. Icarus 203, 238–241.

Kite, E.S., Rubin, A.M., 2015. Sustained eruptions on Enceladus explained by turbulent dissipation in tiger stripes. . Luar Planet. Sci. 46th , 1247.

de Koker, N., Stixrude, L., 2009. Self-consistent thermodynamic description of silicate liquids, with application to shock melting of MgO periclase and MgSiO3 perovskite. Geophysical J. Int. 178, 162–179.

Kokubo, E., Ida, S., Makino, J., 2000. Evolution of a circumterrestrial disk and formation of a single moon. Icarus 148, 419–436.

Krähenbühl, U., Ganapathy, J., Morgan, J.W., Anders, E., 1973a. Volatile elements in Apollo 16 samples: Implications for highland volcanism and accretion history of the moon. Proc. Fourth Lunar Sci. Conf. 2, 1325–1348.

Krähenbühl, U., Ganapathy, J., Morgan, J.W., Anders, E., 1973b. Volatile Elements in Apollo 16 Samples: Possible Evidence for Outgassing of the Moon. Science 180, 858–861.

Kraus, R.G., Stewart, S.T., Swift, D.C., Bolme, C.A., Smith, R.F., Hamel, S., Hammel, B.D., Spaulding, D.K., Hicks, D.G., Eggert, J.H., Collins, G.W., 2012. Shock vaporization of silica and the thermodynamics of planetary impact events. J. Geophys. Res. 117, E09009.

Kurosawa, K., Kadono, T., Sugita, S., Shigemori, K., Sakaiya, T., Hironaka, Y., Ozaki, N., Shiroshita, A., Cho, Y., Tachibana, S., Vinci, T., Ohno, S., Kodama, R., Matsui, T., 2012. Shock-induced silicate vaporization: The role of electrons. J. Geophys. Res. 117, E04007.

Labrosse, S., Hernlund, J.W., Coltice, N., 2007. A crystallizing dense magma ocean at the base of the Earths mantle. Nature 450, 866–869.

Landau, L.D., Lifshitz, E.M., 1987. Fluid Mechanics, 2nd edition .

Lee, D.C., Halliday, A., Snyder, G.A., Taylor, L.A., 1997. Age and Origin of the Moon. Science 278, 1098–1103.

Lee, D.C., Halliday, A.N., 1996. Hf-W Isotopic Evidence for Rapid Accretion and Differentiation in the Early Solar System. Science 274, 1876–1879.

Li, J., Agee, C.B., 1996. Geochemistry of mantle-core differentiation at high pressure. Nature 381, 686–689.

Lucy, L.B., 1977. A numerical approach to the testing of the fission hypothesis. Astron. J. 82, 1013–1024.

Lugmair, G.W., Shukolykov, A., 1988. Early solar system timescales according to 53Mn- 53Cr systematics. Geochim. Cosmochim. Acta 62, 2863–2886.

Machida, R., Abe, Y., 2004. The evolution of an impact-generated partially vaporized circumplanetary disk. Astrophys. J. 617, 633–644.

Makino, J., Taiji, M., Ebisuzaki, T., Sugimoto, D., 1995. GRAPE-4: A special-purpose computer for gravitational N-body problems. Proceedings of the 7th SIAM Conf. on PPSC , 343–348.

Makino, J., Taiji, M., Ebisuzaki, T., Sugimoto, D., 1997. GRAPE-4: A massively parallel special-purpose computer for collisional N-body simulations. Astrophys. J. 480, 432–446.

Mastrobuono-Battisti, A., Perets, H.B., Raymond, S.N., 2015. A primordial origin for the compositional similarity between the Earth and the Moon. Nature 520, 212–215.

McCubbin, F.M., Steele, A., Hauri, E.H., Nekvasil, H., Yamashita, S., Hemley, R.J., 2010. Nominally hydrous magmatism on the Moon. Proc Natl Acad Sci U S A 107, 11223–8.

McDonough, W.F., Sun, S.S., 1995. The composition of the Earth. Chemical Geology 120, 223–253.

McKinnon, W.B., 2015. Effect of Enceladus's rapid synchronous spin on interpretation of Cassini gravity. Geophys. Res. Lett. 42, 2015GL063384.

Melosh, H.J., 2007. A hydrocode equation of state for SiO2. Meteorit. Planet. Sci. 42, 2079–2098.

Monaghan, J.J., 1992. Smoothed particle hydrodynamics. Annu. Rev. Astron. Astrophys. 30, 543–574.

Monaghan, J.J., Lattanzio, J.C., 1985. A refined particle method for astrophysical problems. Astron. Astrophys. 149, 135–143.

Moses, J., Bézard, B., Lellouch, E., 2000. Photochemistry of Saturn's Atmosphere I. Hydrocarbon Chemistry and Comparisons with ISO Observations. Icarus 143, 244–298.

Mukhopadhyay, S., 2012. Early differentiation and volatile accretion recorded in deep-mantle neon and xenon. Nature 486, 101–104.

Nakajima, M., Stevenson, D.J., 2014. Investigation of the Initial State of the Moon-Forming Disk: Bridging SPH Simulations and Hydrostatic Models. Icarus 233, 259–267.

Nakajima, M., Stevenson, D.J., 2015. Melting and mixing states of the Earth's mantle after the Moon-forming impact. Earth and Planetary Science Letters 427, 286–295.

Nakajima, S., Hayashi, Y., Abe, Y., 1992. A Study on the "Runaway Greenhouse Effect" with a One-Dimensional Radiative-Convective Equilibrium Model. Journal of Atmospheric Sciences 49, 2256–2266.

Nimmo, F., Porco, C., Mitchell, C., 2014. Tidally Modulated Eruptions on Enceladus:Cassiniiss Observations and Models. The Astronomical Journal 148, 46.

Nimmo, F., Spencer, J.R., Pappalardo, R.T., Mullen, M.E., 2007. Shear heating as the origin of the plumes and heat flux on Enceladus. Nature 447, 289–291.

Pahlevan, K., 2013. Developing the rare earth element constraint for scenarios of lunar origin. Lunar Planet. Sci. 44th , 3073.

Pahlevan, K., Stevenson, D.J., 2007. Equilibration in the aftermath of the lunar-forming giant impact. Earth Planet. Sci. Lett. 262, 438–449.

Pahlevan, K., Stevenson, D.J., Eiler, J.M., 2011. Chemical fractionation in the silicate vapor atmosphere of the earth. Earth Planet. Sci. Lett. 301, 433–443.

Parker, E.N., 1963. Interplanetary Dynamical Processes. New York, Wiley, Chap. 4 , 41–50.

de Pater, I., Lissauer, J.J., 2010. Planetary Sciences. Cambridge University Press, 2 edition , 663.

Porco, C., DiNino, D., Nimmo, F., 2014. How the Geysers, Tidal Stresses, and Thermal Emission across the South Polar Terrain of Enceladus Are Related. The Astronomical Journal 148, 45.

Porco, C.C., Helfenstein, P., Thomas, P.C., Ingersoll, A.P., Wisdom, J., West, R., Neukum, G., Denk, T., Wagner, R., Roatsch, T., Kieffer, S., Turtle, E., McEwen, A., Johnson, T.V., Rathbun, J., Veverka, J., Wilson, D., Perry, J., Spitale, J., Brahic, A., Burns, J.A., Delgenio, A.D., Dones, L., Murray, C.D., Squyres, S., 2006. Cassini observes the active south pole of Enceladus. Science 311, 1393–401.

Postberg, F., Kempf, S., Schmidt, J., Brilliantov, N., Beinsen, A., Abel, B., Buck, U., Srama, R., 2009. Sodium salts in E-ring ice grains from an ocean below the surface of Enceladus. Nature 459, 1098–101.

Postberg, F., Schmidt, J., Hillier, J., Kempf, S., Srama, R., 2011. A salt-water reservoir as the source of a compositionally stratified plume on Enceladus. Nature 474, 620–622.

Prettyman, T.H., Hagerty, J.J., Elphic, R.C., Feldman, W.C., Lawrence, D.J., McKinney, G.W., Vaniman, D.T., 2006. Elemental composition of the lunar surface:

Analysis of gamma ray spectroscopy data from Lunar Prospector. Journal of Geophysical Research 111.

Pritchard, M.E., Stevenson, D.J., 2000. Thermal aspects of a lunar origin by giant Impact. Univ. of Arizona Press, Tucson, In: Canup, R. M., Righter, K. (Eds.), Origin of the earth and Moon.

Reufer, A., Meier, M.M.M., Benz, W., Wieler, R., 2012. A hit-and-run giant impact scenario. Icarus 221, 296–299.

Righter, K., Drake, M.J., Yaxley, G., 1997. Prediction of siderophile element metal-silicate partition coefficients to 20 GPa and 2800C: the effects of pressure, temperature, oxygen fugacity, and silicate and metallic melt compositions. Phys. Earth Planet. Inter. 100, 115–134.

Ringwood, A.E., Kesson, S.E., 1977. Basaltic magmatism and the bulk composition of the moon. II - siderophile and volatile elements in moon, earth and chondrites: implications for lunar origin. The Moon 16, 425–464.

Robinson, K.L., Taylor, G.J., 2014. Heterogeneous distribution of water in the Moon. Nature Geoscience 7, 401–408.

Rubie, D.C., Jacobson, S.A., Morbidelli, A., O'Brien, D.P., Young, E.D., de Vries, J., Nimmo, F., Palme, H., Frost, D.J., 2015. Accretion and differentiation of the terrestrial planets with implications for the compositions of early-formed Solar System bodies and accretion of water. Icarus 248, 89–108.

Rubie, D.C., Melosh, H.J., Reid, J.E., Liebske, C., Righter, K., 2003. Mechanisms of metal-silicate equilibration in the terrestrial magma ocean. Earth Planet. Sci. Lett. 205, 239–255.

Saal, A.E., Hauri, E.H., Cascio, M.L., van Orman, J.A., Rutherford, M.C., Cooper, R.F., 2008. Volatile content of lunar volcanic glasses and the presence of water in the Moon's interior. Nature 454, 192–195 (2008).

Saal, A.E., Hauri, E.H., Van Orman, J.A., Rutherford, M.J., 2013. Hydrogen isotopes in lunar volcanic glasses and melt inclusions reveal a carbonaceous chondrite heritage. Science 340, 1317–20.

Salmon, J., Canup, R.M., 2012. Lunar accretion from a roche-interior fluid disk. Astron. J. 760, 83–101.

Schmidt, J., Brilliantov, N., Spahn, F., Kempf, S., 2008. Slow dust in Enceladus plume from condensation and wall collisions in tiger stripe fractures. Nature 451, 685–688.

Shi, C.Y., Zhang, L., Yang, W., Liu, Y., Wang, J., Meng, Y., Andrews, J.C., Mao, W.L., 2013. Formation of an interconnected network of iron melt at Earth's lower mantle conditions. Nat. Geosci. 6, 971–975.

Solomatov, V.S., 2000. Fluid Dynamics of a Terrestrial Magma Ocean. Origin of the Earth and Moon. Univ.of Arizona Press, Tucson , pp. 323–338.

Spencer, J.R., Gorius, N.J.P., Howett, C.J.A., Jennings, D.E., Albright, S.A., 2012.

The Spatial Distribution of Thermal Emission from Baghdad Sulcus, Enceladus, at 100 meter Scales. DPS Meeting 44 , 104.06.

Spencer, J.R., Howett, C.J.A., Verbiscer, A., Hurford, T.A., Segura, M., Spencer, D.C., 2013. Enceladus Heat Flow from High Spatial Resolution Thermal Emission Observations. EPSC abstract 8.

Spencer, J.R., Pearl, J.C., Segura, M., Flasar, F.M., Mamoutkine, A., Romani, P., Buratti, B.J., Hendrix, A.R., Spilker, L.J., Lopes, R.M., 2006. Cassini encounters Enceladus: background and the discovery of a south polar hot spot. Science 311, 1401–5.

Spitale, J.N., Hurford, T.A., Rhoden, A.R., Berkson, E.E., Platts, S.S., 2015. Curtain eruptions from Enceladus' south-polar terrain. Nature 521, 57–60.

Spitale, J.N., Porco, C.C., 2007. Association of the jets of Enceladus with the warmest regions on its south-polar fractures. Nature 449, 695–7.

Stevenson, D.J., 1989. Spontaneous small-scale melt segregation in partial melts undergoing deformation. Geophys. Res. Lett. 16, 1067–1070.

Stevenson, D.J., 1990. Fluid dynamics of core formation. Newton, H. E. and Jones, J.H. (Ed.), Origin of the Earth. Oxford University Press, New York, pp. 231 - 250.

.

Stewart, S.T., Lock, S., Mukhopadhyay, S., 2014. Partial atmospheric loss and partial

mantle melting during the giant impact stage of planet formation. AGU Meeting, San Francisco , P44A–06.

Stixrude, L., Karki, B., 2005. Structure and Freezing of $MgSiO_3$ Liquid in Earth's Lower Mantle. Science 310, 297–299.

Stixrude, L., de Koker, N., Sun, N., Mookherjee, M., Karki, B., B., 2009. Thermodynamics of silicate liquids in the deep Earth. Earth Planet. Sci. Lett. 278, 226–232.

Sugita, S., Kurosawa, K., Kadono, T., Sano, T., 2012. An High-Precistion Semi-Analytical on-Hugoniot EOS for Geologic Materials. Lunar Planet. Sci. 43rd , 2053.

Tackley, P.J., 2012. Dynamics and evolution of the deep mantle resulting from thermal, chemical, phase and melting effects. Earth-Science Reviews 110, 1–25.

Tartése, R., Anand, M., Barnes, J.J., Starkey, N.A., Franchi, I.A., Sano, Y., 2013. The abundance, distribution, and isotopic composition of Hydrogen in the Moon as revealed by basaltic lunar samples: Implications for the volatile inventory of the Moon. Geochimica et Cosmochimica Acta 122, 58–74.

Taylor, G.I., 1931. Effect of Variation in Density on the Stability of Superposed Streams of Fluid. Proc. R. Soc. London A 132, 499–523.

Taylor, S.R., 1979. Lunar and terrestrial potassium and uranium abundances: Impli-

cations for the fission hypothesis. Lunar and Planetary Science Conference 10th , 2017–2030.

Tera, F., Papanastassiou, D.A., Wasserburg, G.J., 1974. Isotopic evidence for a terminal lunar cataclysm. Earth and Planetary Science Letters 22, 1–21.

Tera, F., Wasserburg, G.J., 1976. Lunar ball games and other sports. Lunar Planet. Sci. Conf. 7, 858–860.

Thomas, P.C., Tajeddine, R., Tiscareno, M.S., Burns, J.A., Joseph, J., Loredo, T.J., Helfenstein, P., Porco, C., 2016. Enceladuss measured physical libration requires a global subsurface ocean. Icarus 264, 37–47.

Thompson, C., Stevenson, D.J., 1988. Gravitational instability in two-phase disks and the origin of the moon. Astrophys. J. 333, 452–481.

Thompson, S.L., Lauson, H.S., 1972. Improvements in the chart-D radiationhydrodynamics code III: revised analytic equation of state. Sandia National Laboratories, Albuquerque, New Mexico , 119p.

Tian, F., Stewart, A., Toon, O., Larsen, K., Esposito, L., 2007. Monte Carlo simulations of the water vapor plumes on Enceladus. Icarus 188, 154–161.

Tonks, W.B., Melosh, J., 1993. Magma Ocean Formation Due to Giant Impact. J. Geophys. Res. 98, 5319–5333.

Touboul, M., Kleine, T., B., B., Palme, H., Wieler, R., 2007. Late formation and

prolonged differentiation of the moon inferred from w isotopes in lunar metals. Nature 450, 1206–1209.

Touboul, M., Puchtel, I.S., Walker, R.J., 2012. 182W Ecidence for Long-Term Preservation of Early Mantle Differentiation Products. Science 335, 1065–1069.

Touma, J., Wisdom, J., 1998. Resonances in the early evolution of the earth-moon system. Astron. J. 115, 1653–1663.

Visscher, C., Fegley, B., 2013. Chemistry of Impact-Generated Silicate Melt-Vapor Debris Disks. The Astrophysical Journal 767, L12.

de Vries, J., Nimmo, F., Jacobson, S.A., Morbidelli, A., Rubie, D.C., 2014. Melting Due to Impacts on Growing Proto-Planets. Lunar Planet. Sci. 45th , 1896.

Wada, K., Kokubo, E., Makino, J., 2006. High-resolution simulations of a moon-forming impact and postimpact evolution. The Astrophys. J. 638, 1180–1186.

Wade, J., Wood, B.J., 2005. Core formation and the oxidation state of the Earth. Earth Planet. Sci. Lett. 236, 78–95.

Waite, J.H., Lewis, W.S., Magee, B.A., Lunine, J.I., McKinnon, W.B., Glein, C.R., Mousis, O., Young, D.T., Brockwell, T., Westlake, J., Nguyen, M.J., Teolis, B.D., Niemann, H.B., McNutt, R.L., Perry, M., Ip, W.H., 2009. Liquid water on Enceladus from observations of ammonia and 40Ar in the plume. Nature 460, 487–490.

Waite, J.H., Magee, B., Brockwell, T., Zolotov, M.Y., Teolis, B., Lewis, W.S., 2011. Enceladus Plume Composition. EPSC Abstract 6, EPSC–DPS2011–61–4.

Walker, J.C.G., 1982. The earliest atmosphere of the Earth. Precarnbrian Research 17, 147–171.

Walsh, K.J., Morbidelli, A., Raymond, S.N., O'Brien, D.P., Mandell, A.M., 2011. The Low Mass of Mars: First Evidence of Early Gas-Driven Migration. Nature 475, 206–209.

Ward, W.R., 2012. On the vertical structure of the protolunar disk. Astron. J. 744, 140.

Wetzel, D.T., Hauri, E.H., Saal, A.E., Rutherford, M.J., 2015. Carbon content and degassing history of the lunar volcanic glasses. Nature Geoscience 8, 755–758.

Wiechert, U., Halliday, A.N., Lee, D.C., Snyder, G.A., Taylor, L.A., Rumble, D., 2001. Oxygen isotopes and the moon-forming giant impact. Science 294, 345–348.

Willbold, M., Elliott, T., Moorbath, S., 2011. The tungsten isotopic composition of the Earth's mantle before the terminal bombardment. Nature 477, 195–199.

Wisdom, J., Tian, Z., 2015. Early evolution of the EarthMoon system with a fast-spinning Earth. Icarus 256, 138–146.

Wolf, R., Anders, E., 1980. Moon and Earth: compositional differences inferred from siderophiles, volatiles, and alkalis in basalts. Geochemica et Cosmochimica Acta 44, 2111–2124.

Zahnle, K., Kasting, J.F., Pollack, J.B., 1990. Mass fractionation of noble gases in diffusion-limited hydrodynamic hydrogen escape. Icarus 84, 502–527.

Zhang, J., Dauphas, N., M., D.A., Leya, I., Fedkin, A., 2012. The proto-earth as a significant source of lunar material. Nature Geosci. 1429, 1–5.

Zimmerman, M.E., Zhang, S., Kohlstedt, D.L., Karato, S., 1999. Melt distribution in mantle rocks deformed in shear. Geophys. Res. Lett. 26, 1505–1508.